Study on Reduction of Passive Waveguide's loss by Selective Zinc Diffusion for Selective Area MOVPE Monolithically Integrated Photonic Devices

MOVPE   Zn

A dissertation submitted to the
Graduation School of Engineering of the University of Tokyo

in partial fulfillment of the requirements for the Master's degree in
Electronic Engineering

by
Chan, Melvin Jeffrey Cheng

Research Supervisor: Professor Yoshiaki Nakano

1. Introduction

Monolithic integration of optical, optoelectronic, electronic and/or micro-mechanical device elements on a single semiconductor substrate enables the fabrication of compact device modules offering various kinds of reliable and high performance functionalities at low cost. Opto-Electronic Integrated Circuits (OEICs) or Photonic Integrated Circuits (PICs) are envisaged to become key elements within flexible and scalable ultra-high capacity optical telecommunication systems. With today's technology, the generation, detection, modulation, switching, and transport of light on chip enables cost reduction, but it will also allow for a new generation of high functionality photonic integrated circuits (PICs) with reduced size and power dissipation.

Currently, the majority of optoelectronic components in use in the field are in discrete nature. Each component is designed to perform one specific task, and several components with differing functions are then interconnected. This method, commonly refer as hybrid integration. Hybrid integration has one advantage in that each component is optimized for one specific function, enabling that device to perform its task flawlessly. And this is also a relatively feasible method of integrating different passive components. However, there are several shortcomings involved with this method of system construction. One is the difficulty in coupling light on and off each discrete chip. Advances in the coupling between the semiconductor chip and a fiber optic cable using mode converters is a significant step in reducing the coupling loss, yet it is still a dominant source of optical loss. Another is the expense involved with the discrete packaging of each component, which is the major cost source for the components. [1-2] Thus, monolithic integration is the only sole solution the dilemma. The monolithic integration of the optoelectronic devices on the same chip offers the potential to completely eliminate the device-to-device coupling problem which commonly occurs in hybrid integration. This can provide a significant reduction in packaging cost and package size as well as increased reliability and reduced power dissipation. Furthermore, the potential for high functionality components such as widely tunable transmitters and chip scale wavelength conversion devices will open new ways for wavelength division

multiplexing (WDM) applications such as dynamic provisioning, reconfigurable optical add/drop multiplexers (ROADMs), wavelength routing, and optical packet switching. Among different monolithic integration techniques, the following are the most common integration technique: butt-joint regrowth, offset quantum wells, quantum well intermixing (QWI), and selective area growth (SAG).

1.1 Comparison of Different Integration Schemes

In this section different integration schemes are being detailed and compared: [3]

1.1.1 Butt-Joint Regrowth

Butt-joint regrowth or etch-and-regrowth involves the selective removal of waveguide core material followed by the regrowth of an alternate waveguide core using different material composition. This process is inherently difficult involving a precise etch of the original waveguide core, followed by a regrowth of waveguide material with composition and thickness variables. The coupling efficiency between the two different regions and the reflection at the interface are key characteristics affecting the performances of integrated devices [4-5] Although through this method, passive and active parts can be optimized individually, high coupling efficiency is difficult to achieve, and the device characteristics are strongly affected by the regrowth interface which is subject to possible contamination during wafer processing between the regrowth steps. Besides, the risk of poor surface morphology increases with the increasing number of etch-and-regrowth steps. Hence, this technique might lead to low device yields and higher final product cost. However, this method is still remained as most commonly used integration technique.

1.1.2 Offset Quantum Wells

Offset quantum wells, also categorize under Etch and Regrowth, takes place where the quantum wells are grown above the waveguide and selectively removed in various regions post-growth. Various integrated structures based on this technique have been reported. The drawback of the offset quantum-well method, however, is the limitation of each integrated component to limited

number of band edges, difficult in fabricating complex, high-performance PICs. Furthermore, the vary nature of the offset QW design does not allow for the optimal optical mode overlap with the quantum wells, leading to a modal gain which is not at the optimal level, as compared with a centered quantum well design. [4-5]

1.1.3 Quantum Well Intermixing (QWI)

Quantum well Intermixing (QWI) makes use of the metastable nature of the compositional gradient found at heterointerfaces. The natural tendency for materials to interdiffuse is the basis for the intermixing process. In this approach, light generation and amplification components are fabricated in the non-intermixed regions, and low-loss light guiding components are realized in the intermixed regions. The integrated optical functions must share a similar material structure, since growth occurs in only a single step. This results in two constraints. First, efficient light detection components that require thick, undoped bulk materials with a bandgap smaller than the photon energy are difficult to realize using this method. Second, light guiding components must consist of MQWs similar to light generating devices. Hence, it is difficult to optimize the light guiding material for special device functions such as polarization-insensitive waveguides and waveguides with high coupling efficiencies to single-mode optical fibers. Several methods have been demonstrated to realize QWI such as surface dopant diffusion, ion implantation, and photoabsorption-induced local heating. QWI is known for its limitation in dealing with limited band edges. But multiple bandgap energies integrated device has been reported based on QWI. [8-10]

1.1.4 Selective Area Growth (SAG)

The Selective area growth (SAG) process, involves the selective growth using a mask (typical SiO_2 or Si_3N_4 films). In such process, a mask is patterned on the surface of the wafer prior to epitaxial growth. The geometry of the mask has a role in determining the growth near the vicinity of the mask and can be used to obtain different compositions and thickness across the wafer. This method is useful in fabricating several quantum-well band edges across the wafer, but due to the fact that the thickness is inherently coupled with the band

edge in these regions, the optical confinement factor cannot be independently optimized. And also due to the doped cladding are grows simultaneously on both active and passive region together, the loss in passive region is unavoidable. This will be more detailed in the succeeding chapters. [11-12]

1.1.5 Summary of Different Integration Schemes

Method	Compactness	Complexity	Fabrication cost	Multiple-λ	Passive-active coupling	Passive propagation loss
Hybrid Integration	×	×	×		×	
Butt-joint Regrowth					×	×
Offset Quantum Wells				×		×
Quantum Well Intermixing (QWI)						×
Selective Area Growth (SAG)						×

Table 1: comparison of different active-passive integration schemes
Legend: × - bad,   - OK,   - good,   -very good

In this research, Selective Area Metal Organic Vapor Phase Epitaxy (SA-MOVPE) is used thru out this in fabrication of monolithically integrated photonic devices. This is due to its merit of simplicity in single-step epitaxy, the compactness of the fabricated device and its capability of achieving growing different bandgap energies simultaneously on a single substrate. However, undesirable total insertion loss is one of the major shortcomings of this technique. Reasons of that are stated in the succeeding chapters. In this research, methods

of reducing such loss is proposed and studied.

1.2 Outline of the Thesis

The purpose of this thesis is to demonstrate the potential of selective zinc diffusion as a solution to the optical absorption issue occurred in the p-doped InP upper cladding which is unavoidably during single-step-epitaxy selective area growth. Moreover, this thesis would like to demonstrate that given similar condition, an undoped passive waveguide should suffer less optical loss than a doped one due to less carrier absorption in the said region. And finally this thesis would like to prove the feasibility of applying zinc diffusion to selective area grown device.

In specific, this thesis is divided mainly into 7 chapters, and it's organized as follow:

In Chapter 2, the principle of Selective Area MOVPE is presented. Along with the physical properties of the SAG regions has been detailed. As for this thesis, the selective area MOVPE is chose as the integration method and its properties is exploited to optimize the epitaxy quality and device performance.

In Chapter 3, the selective zinc diffusion, a solution we proposed to solve the issue of Selective Area growth is presented. The diffusion profile of both conventionally doped active device and our proposed zinc diffused device has been presented as well.

In Chapter 4, the design aspect of the Monolithically Integrated 4-channels DFB laser Array by Selective Area MOVPE for 1.5um CWDM system has been presented. Both active and passive components' design considerations are also discussed in this chapter. The fabricated selective integrated device and its basic characteristics are illustrated in the last part of the same chapter.

In Chapter 5, the fabrication process and technologies is presented. This section gives an overview of the processing procedures and technology of the separate components which is necessary for the realization of the whole device.

Subsequently, the yield issue of the integrated device is also addressed.

In Chapter 6, the characterization for both passive and active regions of the Monolithically Integrated 4-channels DFB laser Array device has been presented. Functions and behavior of each integrated components are characterized and presented as well.

In chapter 7, the conclusions have been presented; along with the possible improvement we think which is suitable for this thesis.

2. Selective Area MOVPE

In this chapter two parts are mainly studied and investigated. Namely the Metal Organic Vapor Phase Epitaxy(MOVPE) and Selective Area Growth (SAG) technique.

Crystal growth is always the first step in device fabrication. Improvement in single crystal growth of compound semiconductors led to development of highly reliable laser diodes operation at room temperature. Together with the development of low-loss optical fiber and optical amplifier, the laser diode is a driving force in all aspect of optical communication, sensing, electronics and computing. Reduction of crystal defects and incorporation of quantum size effects like the quantum well led to great increase in laser lifetime, efficiency, modulation response and etc. And the two most used methods for fabricating thin films with atomic layer control are the metal-organic vapor phase epitaxy (MOVPE) and molecular beam epitaxy (MBE). MBE is ideal for very abrupt interface in quantum wells, but due to difficulty of maintaining ultra-high vacuum used in MBE apparatus its use in mass production is limited. MOVPE on the other hand is the most cost effective mass production technology for epitaxial growth of thin films. In this research, MOVPE is used to grow the crystal of the fabricated devices.

In this section, the MOVPE would be briefly introduced first. After that, the principle of SAG would be schematically described. Different growth enhancement factor of indium and gallium resulted from different sticking probability was used to explain the bandgap engineering with SAG.

2.1 Introduction of Metal Organic Vapor Phase Epitaxy (MOVPE)

Depicted in Fig.2.1 is the schematic configuration of the MOVPE machine which is used in this research, and model number AIX 200/4 by AIXTRON. The sources for group III are Trimethylgallium (TMGa) ,Trimethylindium (TMIn), and that for group V are Tertiarybuthylarsine (TBAs) and Tertiarybuthylphosphine

(TBP). The source for n-doping is Dimethylzinc (DMZn), and that for p-doping Hydrogen Sulfide (H_2S). The basic properties of these sources were listed in table 2.1. In these sources, except for the TMIn is solid and H_2S is vapor, others are liquid at the thermostat bath temperature. In other MOVPE systems, AsH_3 and PH_3 are often used as the sources for V group, however, mainly for safety concerns, almost all of the sources are organic solutions in this system.
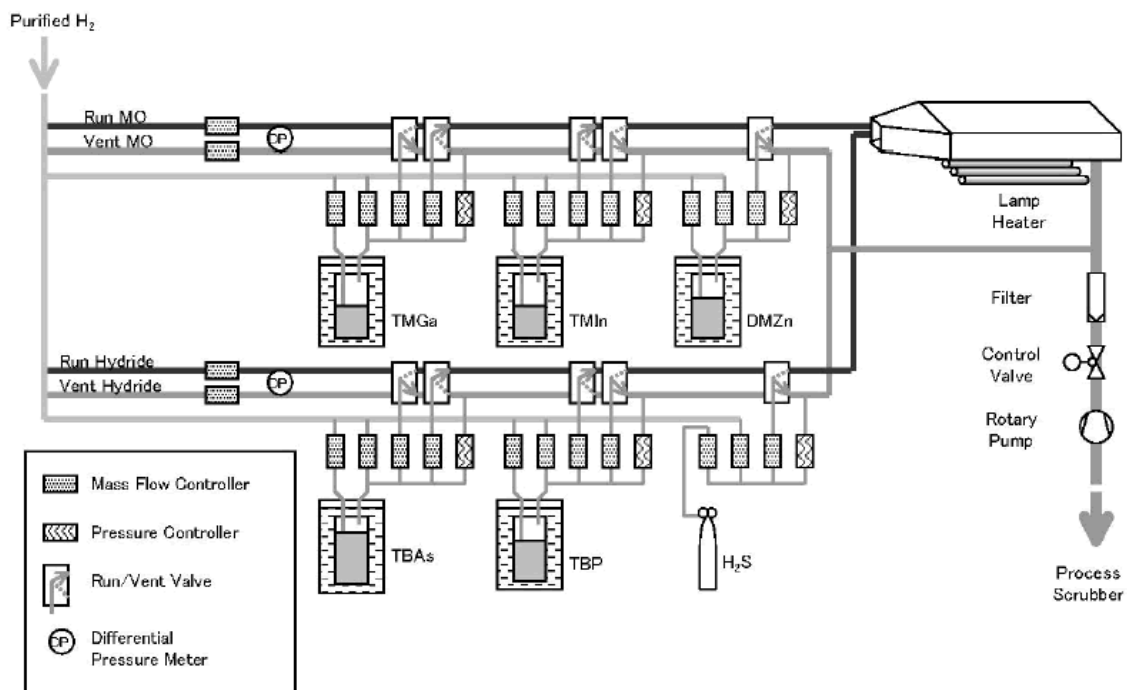

Fig.2.1 Schematic configuration of MOVPE system used in this research.

Purified H_2 gas is guided to each source tank through mass flow controllers (MFC), and saturated vapor is carried out to "Run" line or "Vent" line through other MFC's. The pressures in all of the gas lines are auto-controlled with pressure controllers. "Run MO" line is used to mix all of the saturated H_2 gas containing group III as well as zinc sources, and guide into the reactor chamber with a carefully controlled and stable flow rate. "Vent MO" line is used to collect the unused saturated gas and guide it into the phosphor-trap filter and then scrubber. "Run Hydride" and "Vent Hydride" lines play the same roles for group V and sulfur sources. Differential pressure meters are placed between "Run MO" line and "Vent MO" line, as well as between "Run Hydride" line and "Vent Hydride" line, to monitor the pressure difference and thus prevent reverse flows at the point of link up before phosphor- trap filter. [13]

11

Element	Source	Molecular Weight	Fusing Point [^{O}C]	Boiling Point [^{O}C]	Vapor pressure $\log_{11}P$ [Torr] T: temperature [K]	Thermostat Temperature [^{O}C]
In	TMIn	159.9	88.4	133.8	$10.52 - 3014/T$	18
Ga	TMGa	144.8	-15.8	55.7	$8.07 - 1703/T$	0
As	TBA	134.1	-1	68	$7.243 - 1509/T$	18
P	TBP	90.1	4	54	$7.5857 - 1539/T$	18
Zn	DMZn	95.4	-42	46	$7.802 - 1560/T$	-10
S	H_2S	34.1	-82.9	-60.19	--	--

Table.2.1 Parameters of MOVPE Source

An important technique to be noted for clean epitaxial interface in MOVPE is the use of dummy line. In the process of epitaxy, the MFC regulation steps are kept to a minimum number of times, since the regulation requires a certain length of time, which results in a broad interface between different epitaxy layers. For this purpose, the injection of the source-containing gas into the "Run" line is not a simple open/close valve, but a switch valve between "Run" line and "Vent" line. Basically, when the source-containing gas is switched from "Vent" line to "Run" line, the same quantity pure H_2 dummy gas would be switched from "Run" line to "Vent" line through dummy lines, to maintain a stable flow in the "Run" and "Vent" lines. Since the speed of this switching is much faster than the MFC regulating, the epitaxy with clean interfaces between different epitaxy layers is possibly. The high quality layer interface is vital for thin film epitaxy, especially for multi-quantum wells (MQW) which is grown in the process.

2.2 Principle of Selective Area MOVPE

In Selective Area MOVPE, epitaxy structure is grown on a mask-patterned substrate. The role of the dielectric mask pattern is to mask epitaxy growth of the region beneath and to bring about bandgap engineering effect to the nearby growth region called Selective Area Growth (SAG) region, while the region far enough, typically a few hundred micron, from the mask is called planar region. These planar regions can be considered as growth on a plain substrate without any mask through normal MOVPE. Depicted in Fig. 2.2 is the schematic cross sectional view of SAG in MOVPE. The SAG region (the

active region) is the area sandwiched between the masks. Since no growth is undergoing in the masked area, extra supply of group-III species diffuse from the masked region as well as from the crystal facet and hence, locally enhance the growth rate in the region near and sandwiched between these masked areas. Consequently, layer thickness at these regions become larger and, the bandgap energies become smaller than that of the planar region. Moreover, larger incorporation of In source than that of Ga source is another reason that shrinks the bandgap of the SAG region furthermore. [14] Thus far, we have succeeded in incorporating 5 band-gap compositions on a single substrate through SAG technique and the bandgap energies measured with photoluminescent showed good agreement with the design.
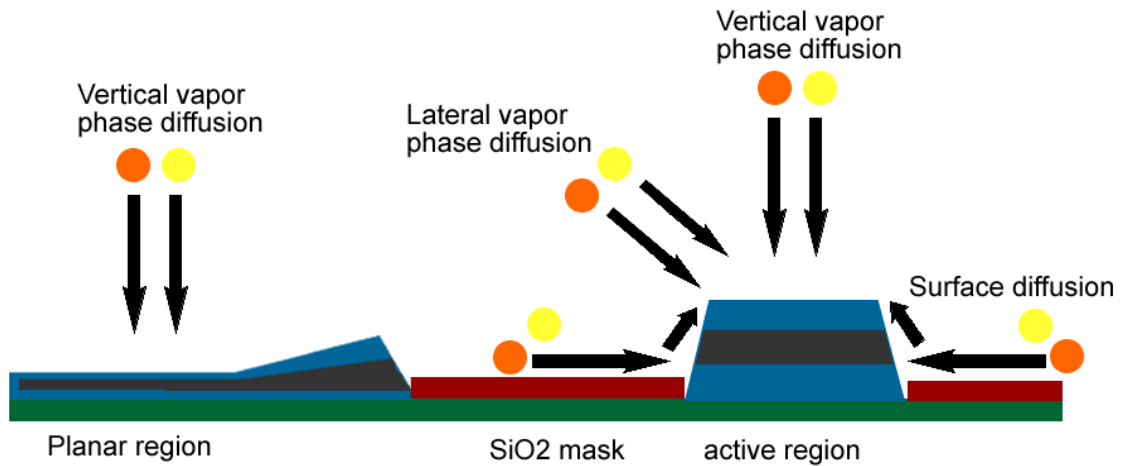

Fig.2.2 Schematic view of monolithic integration by the selective Area MOVPE.

2.3 Physical Properties of Selective Area Grown (SAG) Regions

As mentioned in the previous section, the properties of the SAG region can be tailored by controlling the diffusion process in MOVPE. This can be done by proper design of the mask widths and the gap dimension between a pair of masks. To be specific, the ratio between the mask width and gap width is proportion (W_m/G_m) and the most important aspect in determine the bandgap engineering in the SAG region. For application in photonic integrated circuits, waveguide components will have to be fabricated in the SAG region as active parts while as contrast to this, the non-SAG region or the planar region is used as passive components. Usually some lithography and etching process is

needed to fabricate waveguides on top of SAG region. However another approach is to design a narrow-stripe SAG mask such that the waveguide structure is formed automatically as its epitaxy growth. [15-19]. This self-aligned approach, or generally known as narrow strip selective area growth (NS-SAG) can save the necessary of post-epitaxial processing and hence, can save cost and time. Fig. 2.3 shows a schematic representation of the two main different time of selective area growth. So far, application using narrow strip SAG, as well as arrayed narrow strip SAG, has been reported by different research institute. However, one of the shortcomings in narrow-stripe SAG is that the stripe direction needed to be aligned along specific crystal orientations, otherwise anomalous growth would occur. So, etching is required to achieve bent waveguides. In contrast with narrow stripe SAG, there is wide stripe SAG, which typically of a few tens of micron wide. Lithography and etching process is then used to fabricate waveguides through this wide stripe region. Using a wide stripe SAG, the anomalous growth horns at the edges caused by surface migration can be avoided. Moreover, since the waveguide can be fabricated in the smoother and more uniform area around the center of the SAG region, the influence of growth fault affects less on the device components. As the wide-stripe SAG is utilized. In this research wide-strip SAG is chosen over narrow-strip SAG.
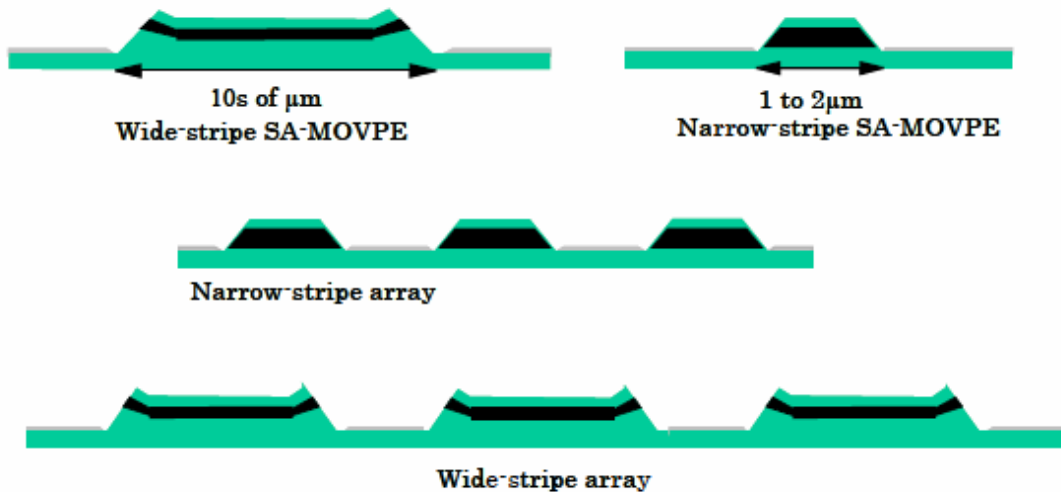

Fig.2.3 Different Schemes of SA-MOVPE: narrow and wide-strip.

Photoluminescence (PL) waveforms illustrated in Fig. 2.4 are obtained thru carefully tailored ratio with respect to each mask width to gap width ratio. These masked patterns with different W_m/G_m ratio are illustrated in Fig 2.5.

14

[9-10] These data are obtained thru repeated trials and therefore the very essence of Selective area growth. In order to explain Fig. 2.4 in simpler terms, for given planar condition such of 1410nm (w0), the 1550nm can be obtained with mask width to gap width ratio of 2.5 (50μm of mask with to 20μm of gap width), while 1600nm can be obtained with ratio of 4 (80μm of mask width to 20μm of gap width) similarly and so on. [14]
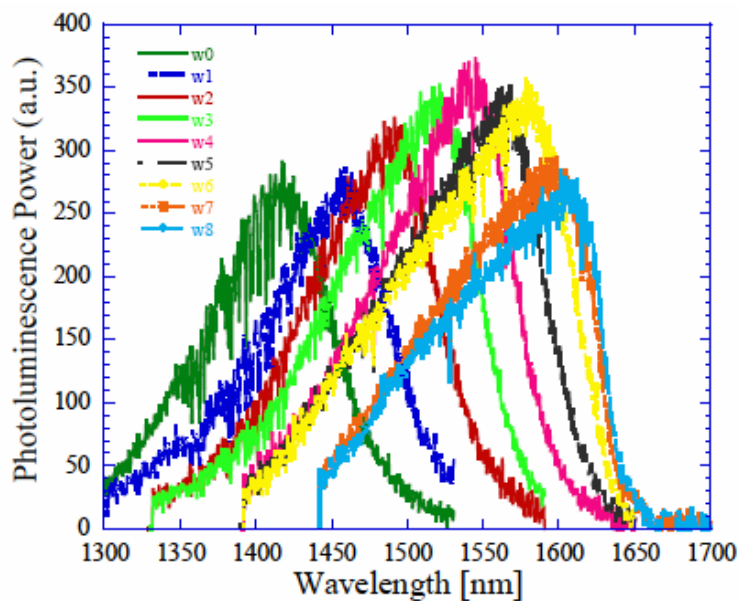
Fig.2.4 PL waveform in 20μm growth gap. The legend 1, 2, 3 to 8 denotes the SAG mask step in Fig 2.3. w0 refers to planar region
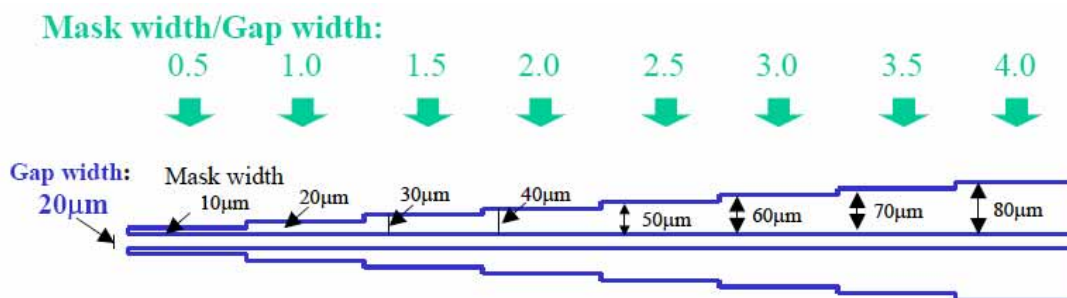

Fig.2.5 Old Selective Area growth mask design with 20μm growth gaps

However the findings above were conducted a couple of years ago, for making a three bandgap energies device for all optical switching purpose and it's slightly different from the requirement in this study. Our target wavelengths in

this study are 1530nm, 1550nm, 1570nm and 1590nm. These wavelengths are standard in 1.55µm for CWDM system. There for new W_m/G_m ratios are needed and a new mask is designed. For details of 1.55µm for CWDM system and the new photonic device by selective area MOVPE we are going to fabricated, (named Monolithically Integrated 4-Channel DFB Laser Array with Optical Combiner for 1.55µm CWDM Systems by Selective Area MOVPE) they are discussed comprehensively in chapter 4. Depicted in Fig 2.6 is the final prototype of the newly designed mask. It represents the newly designed SAG condition with 10µm, 15µm and 20µm gaps. The PL waveforms are shown in Fig. 2.7 with a) 10µm, b)15µm and c)20µm gaps respectively. In the end, we observed that the 15µm gap is the most ideal case in this study due to the uniformity of intensity; the width is long enough for waveguide fabrication casing. And the PL wavelength are observed to be1530.2nm, 1552.2nm, 1571.1nm and 1590.6nm for channel 1, channel 2, channel 3 and channel 4 respectively. Meanwhile the planar is observed to be 1481.4nm.

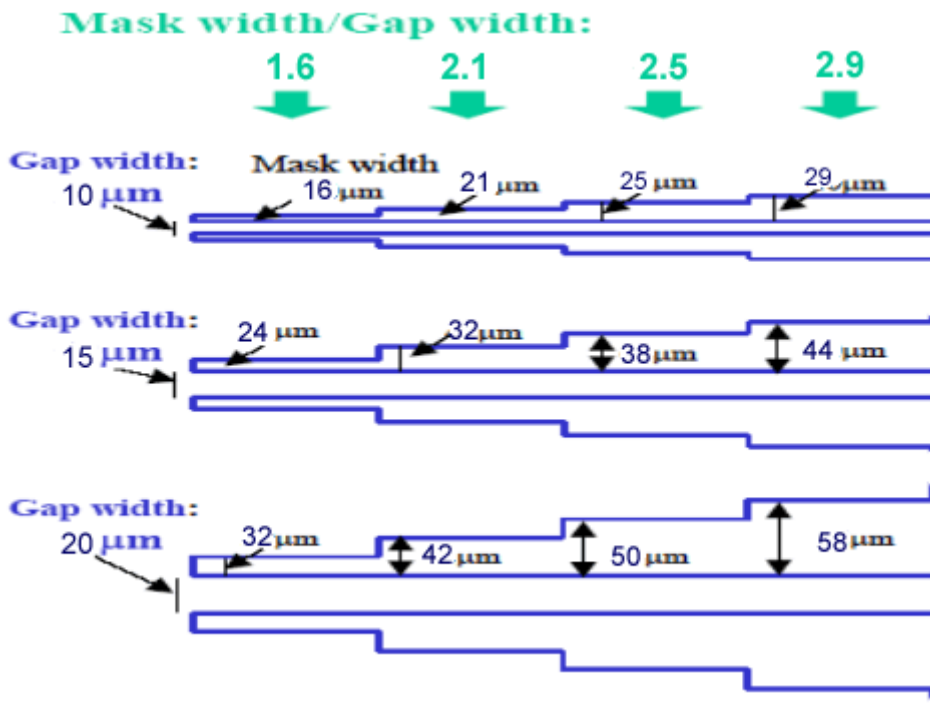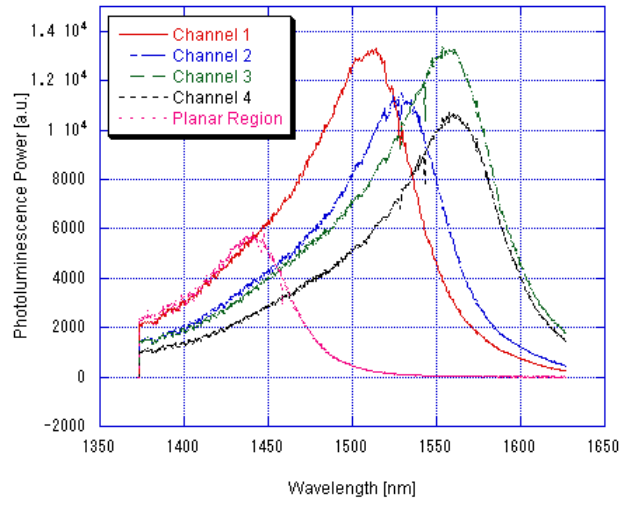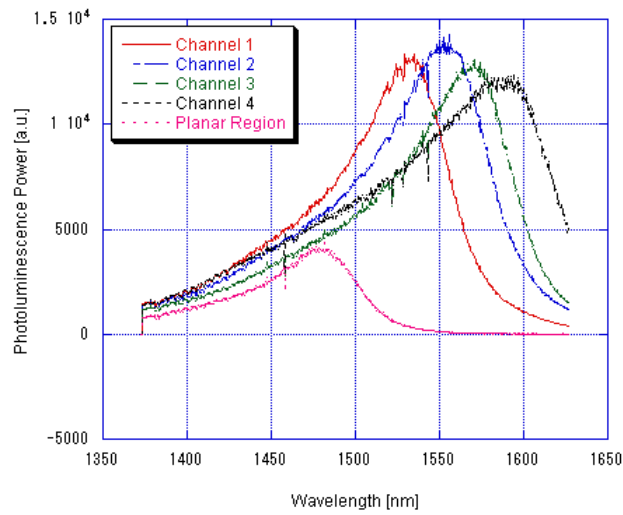*Fig.2.6 The final prototype of newly designed Selective area growth mask design solely dedicated for this research with 10µm, 15µm and 20µm growth gaps.*

16

a) 10um gap

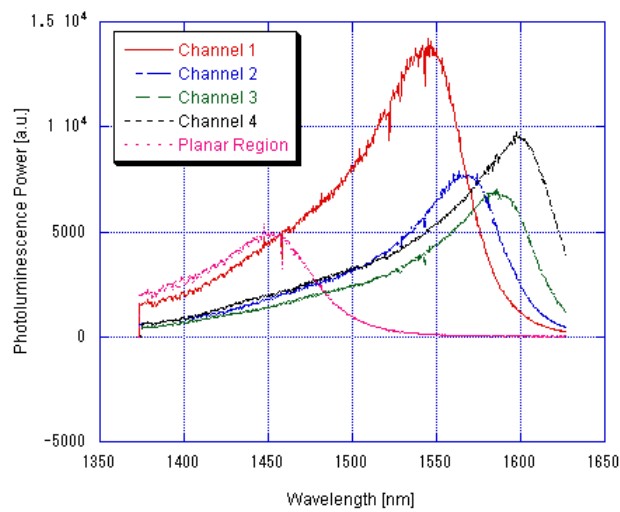## b) 15um gap

c) 20um gap

Fig.2.7 Photoluminescence (PL) waveform of all the four channels in a) 10µm gap. b) 15µm gap

17

and c)20µm gap.

2.4 Micro-Photoluminescence Profiles of SAG Regions

There are various properties of the SAG regions can be studied, such as bandgap energies by micro-photoluminescence (micro-PL) profiling, the epitaxy film thickness by height profiler, scanning electron microscope, and the surface morphology by differential interference microscope. However in this study, for the purpose of simplicity, only micro-PL was focused and extensively studies.

The micro-PL profiler is a set up consists of excitation light source, lenses unit, and detection unit. The light source consists of a Ti-sapphire laser that has high photon energy to excite electrons to higher energy levels. The lenses unit focuses the laser light to a beam waist of a few ten microns, allowing local probing of the PL profile in the SAG region (which in our case was measured from 10 to 20µm). The detector unit consists of semi conductor photo-detectors that are cooled at a low temperature for high sensitivity and low noise.
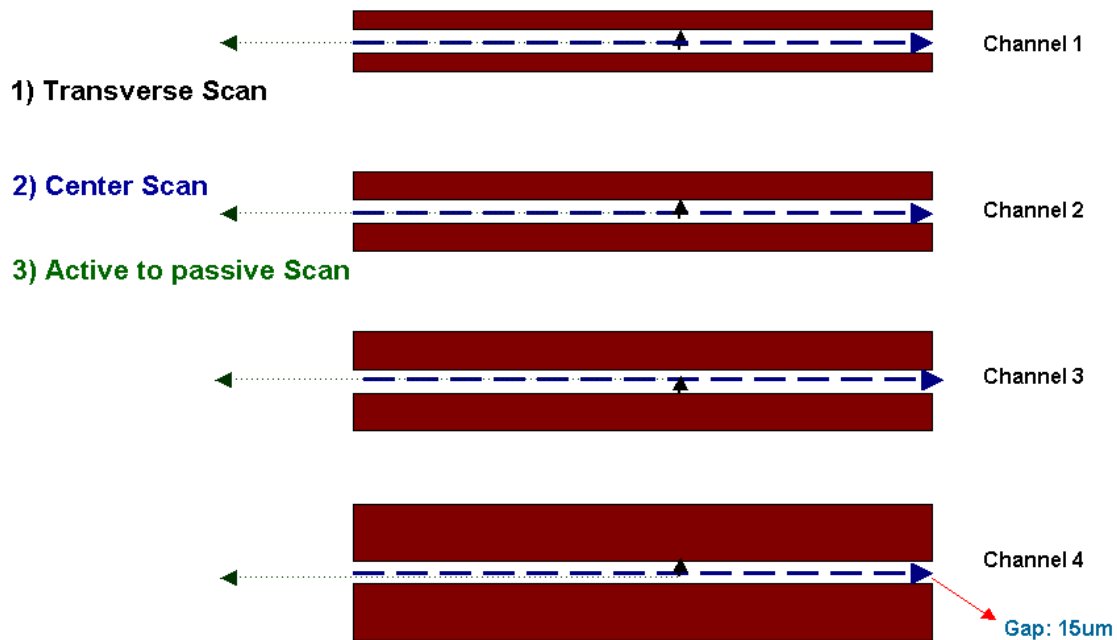

Fig.2.8 Different Photoluminescence scan modes upon SAG region: 1) Transverse Scan (Black arrows), 2) Center Scan (Blue dash arrows) and 3) Active to passive scan (Green Dot arrows)

In this study, the properties of SAG region were studied through three

types of scan modes: namely the center scan, transverse scan and active to passive transition scan, illustrated in Fig. 2.8 Since in this study the design of SAG regions has been set to 15µm, therefore the following properties of SAG was also focused on 15µm width gap alone.

The transverse scan studies the PL profile across the SAG stripe sandwiched by the pair of masks. The mode of scan gives information on the SAG uniformity so that position tolerance for the waveguides to be fabricated in this SAG region can be known. The anomalous growth at the edges of the SAG region can also be investigated.

The center scan studies the PL profile along the center of the SAG stripe. This study can probe directly the PL characteristics of the region that will become the stripe of the waveguide. This scan is significant in investigating the effect of the mask width to the PL in the SAG region as well as the PL intensity uniformity of that same region.

And lastly, the active to passive transition scan gives information on the morphology of the transition region from active to passive and vise versa.

Depicted in Fig. 2.9 is the micro-PL peak wavelength against the distance in transverse scan direction. Here position 0 refers to the starting point at one edge of the SAG region. The total length is 15µm for all four channels as indicated in the same figure. The distribution of the PL peak wavelength across the SAG gap is considerably flat for all four channels. However, it can be observed that, channel one has the most uniform PL peak distribution which is expected since it has the shortest SAG height thus, the crystal structure is expected to be better than the other three channels. Yet, the distribution of all channels shows acceptable results. Since the waveguide is around 2.5µm wide and it expected to be fabricating at the center of the SAG region. Another thing we would like to point out is that the position tolerance is observed to be approximately 13, 8, 12 and 14µm for channel 1, 2, 3 and 4 respectively. Another observation shows that the PL wavelength at the area around the edge has the tendency of shifting to longer wavelength, which happens to all the four channels. This kind of behavior is caused by the anomalous growth where the strain in the crystal is high.
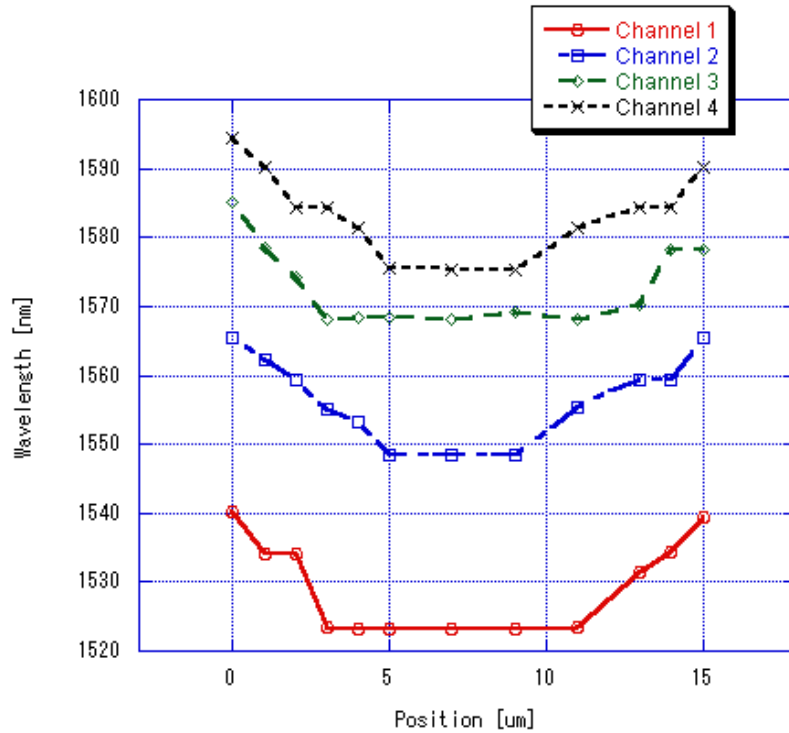
Fig.2.9 Photoluminescence peak wavelength as a function of the distance in transverse scan direction. The mask width is 15μm.
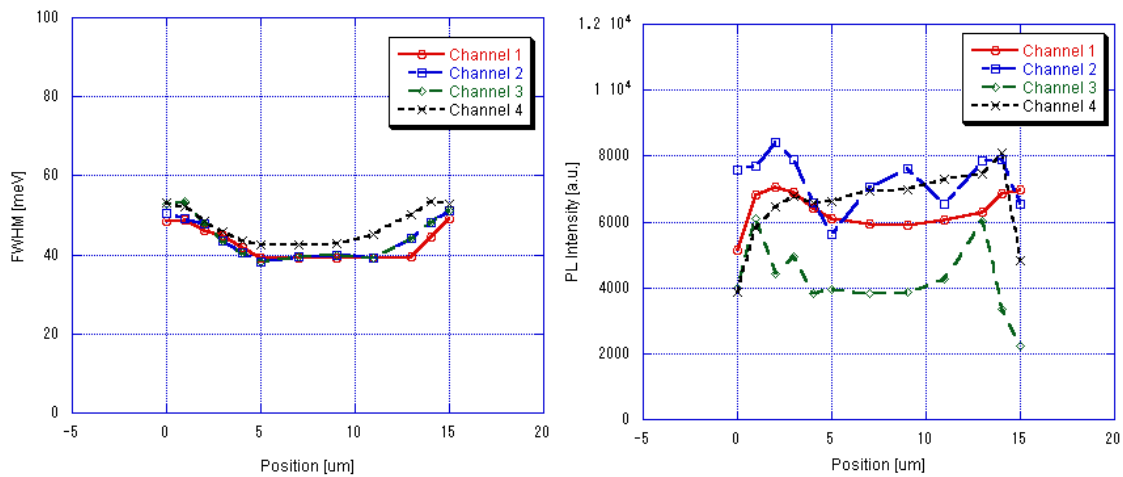
Fig.2.10 (left) Photoluminescence FWHM and (right) PL Intensity of the four channels in Transverse Scan directional distribution.

Fig. 2.10 illustrates the Full Width Half Maximum (FWHM) distribution (at the left) and the Photoluminescence Intensity (at the right) of all the four channels in transverse scan direction. The graph at the left (FWHM) shows though all four channels have relatively similar curves profile and values. Given

a closer look, channel 4 has slightly higher values than channel 3 and 2 follow by channel one. This indicated as generally speaking, as FWHM increases with the SAG mask width, indicating the slightly decreased epitaxial quality. It is also observed in any of the four channels, that the FWHM distribution decrease from the one edge and maintain stable in the center region, closely resembles the position tolerance which indicated in the previous figure. Meanwhile, It is observed the right graph of the Fig. 2.10, that the maximum intensity varies which mainly due to the quality of the grown crystal and the micro-PL measurement system, however among all four channels: the intensity is weakest at the edges then intensifies due to change of quality and stabilized in the middle section, which also resembles the position tolerance

Fig.2.11 Center scans of PL peak, with different SAG mask width to gap width ratio, denoted as four different channels

Depicted in Fig. 2.11 is PL peak versus position through the center of the SAG patterns. The result of all the four channels is illustrated together in the same figure. The total length of each region is a little more than 1000μm. Position 0 denoted as one end of the region. For simplicity only one channel (channel one) was measured from end to end. But it is expected all the four channels share similar outcomes in terms of PL peak. It can be observed that

most of the channels were measured with PL peak near the planar region of approximately 1480nm, and increasing gradually during transition region. For more details of the total length of transition region will be discussed in following passages. The transition region is expected to be similar at both ends regardless channels. The PL FWHM against mask position which is shown in left image of Fig. 2.12 and the PL intensity versus mask position in right side of the same figure give a more thorough analysis to the Figure above. It is observed that both PL FWHM and PL intensity fluctuated mostly in the transition region which is quite expected. Channel 1 in the right figure gives a typical fluctuation intensity phenomenon due to the morphology of the transition region from active to passive region.

Fig.2.12 (Left) Photoluminescence FWHM vs. mask position and (Right) Photoluminescence intensity vs. mask position of the four different channels at center scan.

Fig. 2.13 illustrates the active to passive region transition scan. It gives a clearer picture focusing the transition part from active to passive, starting from halfway of the SAG region and scanning outward until it reaches around 250μ m from the SAG region. (So total of 750μm: 500μm of SAG region + 250μm of planar region). The PL profiling measurement is somehow an extended version of center scan illustrated in Fig. 2.11. It is observed that for all four channels, the transition region is approximately 150μm to 200μm. Fig. 2.14 also shows the agreed results similar to Fig. 2.13. The left graph of Fig. 2.13 illustrates the PL FWHM versus position while the right graph demonstrates the PL intensity versus position of the active to passive region transition scan. Compare to the results in Fig. 2.13, both Intensity and FWHM in the transition region are

observed to be fluctuating due to morphology of the transition region from active to passive region, which is in good agreement with the center scan results in Fig. 2.11 and Fig. 2.12

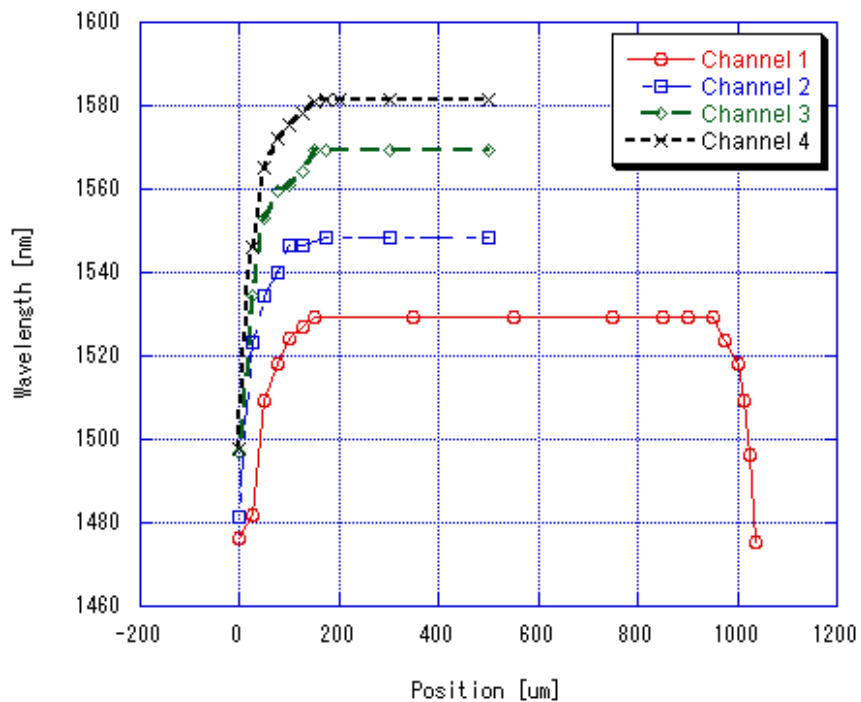*Fig.2.13 Active to passive transition scans of PL peak, with different SAG mask width to gap width ratio, denoted as four different channels*
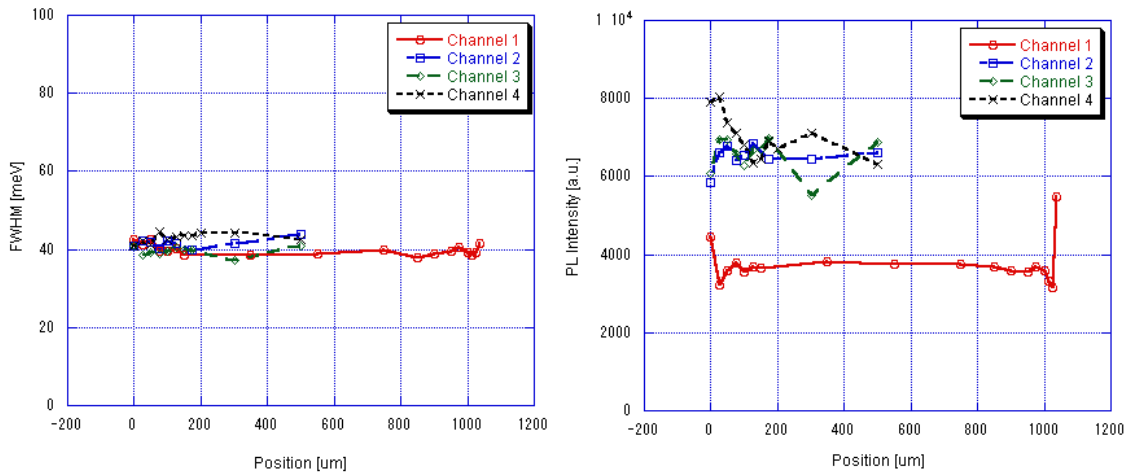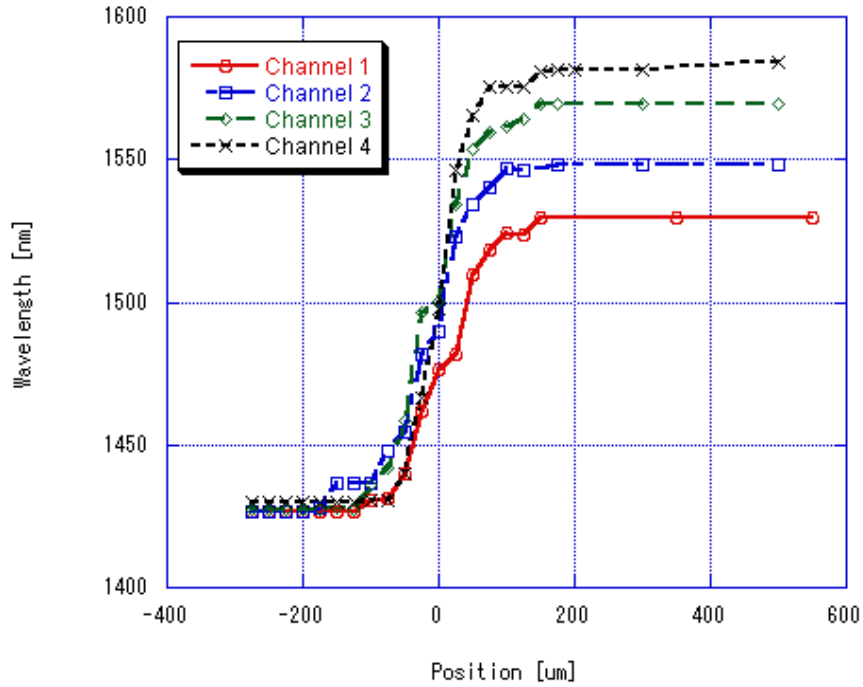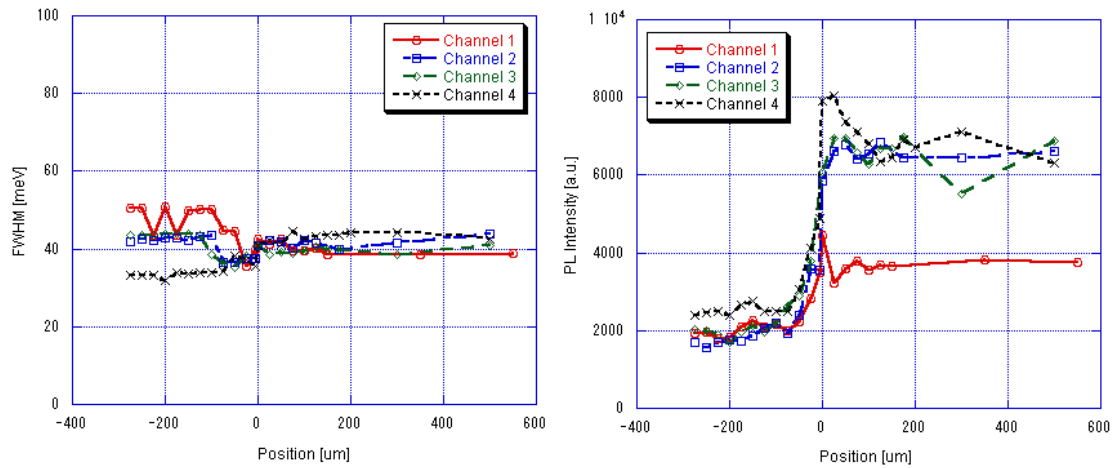

Fig.2.14 (Left) Photoluminescence FWHM vs. position and (Right) Photoluminescence intensity vs. position of the four different channels during the active to passive region.

2.5 Issues of Selective Area MOVPE

Regardless of photonic devices fabricated by selective area MOVPE, total insertion loss remains the main issue. This may due few different reasons, such as unwanted impurities and defects contaminated the surface of device during processing and thus contribute to the propagation loss at the passive waveguide. Second, the total insertion loss which is occurred due to the coupling loss between the optical fibers and the facets of the devices, typically a few dB/facet was observed. Another reason might contribute to the insertion loss such as the side wall roughness of the waveguide, which contributed mostly due to transferring waveguide pattern thru etching, more apparent in dry etching than wet etching. And lastly, which we believe contributed mostly to the propagation loss is involved in the p-doped materials in the single step selective area growth.

Doping refers to the process of intentionally introducing impurities into an extremely pure or intrinsic semiconductor in order to change its electrical properties. The impurities are dependent upon the type of semiconductor. Lightly and moderately doped semiconductor is referred to as extrinsic. A semiconductor which is doped to such high levels that it acts more like a conductor than a semiconductor is called degenerate. Dopants are generally added as the boule is grown, giving each wafer an almost uniform initial doping. To define circuit elements, selected areas which typically controlled by photolithography are further doped by such processes as diffusion and ion implantation, the latter method being more popular in large production runs due to its better controllability.

In typical selective area epitaxy structure which included active device, the topmost structure of both the active and passive regions is highly doped InGaAs layer, known as the cap contact layer. This contact layer has the characteristics of a lower bandgap energy than the core layer and the doping level is usually 10^{19} cm^{-3}. For theses two reasons, the layer is basically very absorptive to the optical signal. The main purpose of this contact layer is to provide an ohmic contact for the active region and is actually an unwanted byproduct happened in the procedure of single step SAG. According to some previous study, 60dB/cm of the total waveguiding loss was found in a deeply-etched passive waveguide having an InGaAs contact layer. To reduce

this loss caused by the absorptive contact layer, the removal of the InGaAs contact layer over the passive region has been etched away ever since this discovery. However, the p-doped InP cladding remained as issue in our study.

In an active optical device, both n-doped and p-doped materials contributed to optical loss. Optical absorption in n-doped material is manly due to intra-band absorption of free carriers, while and intervalence band absorption is the main cause in p-doped materials. Thus, when comparing both, the optical loss in the latter one is much severe. According to our study, 13dB/cm to 99dB/cm for n-doping InP to p-doping InP, assuming the sulfur concentration, n, is equal to the zinc concentration, p, (between 10^{16} cm^{-3} and 10^{19} cm^{-3}). This data can give us how the severe optical loss which caused by in p-doped materials in passive components of an integrated phonic device by SAG.

In order to solve this particular Selective Area MOVPE issue, the p-doped InP material in the upper cladding, proposal has been made and it will be detailed in the next chapter.

2.6 Conclusion

In this chapter, regarding Metal Organic Vapor Phase Epitaxy (MOVPE) and Selective Area Growth (SAG) technique which is applicable in this study has been thoroughly discussed.

First, the MOVPE which used throughout this study has been introduced, followed by the principle of the selective area Growth and the bandgap engineering with selective area MOVPE for photonic integrated circuit (PIC).

Secondly, after understanding the importance of the W_m/G_m ratio in bandgap engineering with SA-MOVPE, repeated experiences has been performed and finally the right W_m/G_m ratio for a simultaneous 5 bandgap energies device has been realized. These ratios are 1.6, 2.1, 2.5, and 2.9 with 15µm gap for 1530nm, 1550nm, 1570nm and 1590nm target wavelengths respectively, which is applicable in 1.55µm CWDM system. Ridge lasers will be fabricated within the mentioned SAG regions.

Thirdly, the Micro-Photoluminescence Profiles of SAG regions used where thoroughly investigated. These micro-PL profiles are mainly the transverse scan, the center scan and the active to passive transition scan, which mentioned in orderly through the later part of this chapter.

And lastly, the issue of selective area MOVPE, particularly the p-doped InP materials in upper cladding of passive parts has been detailed, thus the main issue which this study would like to focus.

3. Selective Zinc Diffusion

In the past years, different studies have been carried out to solve the loss issue in Photonic Integrated Circuits (PIC) by Selective Area Growth (SAG). These include the introduction of grated-index separate confinement structure (GRIN-SCH) structure, the optimization of dry etching and the application of selective zinc diffusion. [20-22] And in this thesis we only focus on the last one. As it was mentioned in the last chapter regarding the issue with SAG, which in this study, is mainly focusing on the optical absorption in the p-doped InP cladding in the passive region. In order to solve this particular issue which yield to severe optical loss, selective zinc diffusion is proposed. It will be detailed in the following section.

3.1 Fick's Law of Diffusion

Diffusion is a random thermal motion of particles such as electrons, holes, dopant atoms, which causing a redistribution of concentration with time to reduce the concentration gradient. The diffusion of particles creates an effective particle current towards the points of lower concentration. In semiconductor, diffusion is a common way of introducing dopants into contact layers. This processing step is the basis for many p-n junctions. Atoms will diffuse from regions of high concentration to region of low concentration. This phenomenon can be modeled thru Fick's law of diffusion. In 1855s, Adolf Fick introduced two differential equations that describes the density fluctuations in a material undergoing diffusion and define the diffusion coefficient, *D*. Fick's First Law states that the flux, J, of a component of concentration, C, across a membrane of unit area, in a predefined plane, is proportional to the concentration differential across that plane, and is expressed by: [23-26]

$$J = -D \frac{\partial C}{\partial x} \qquad (3.1)$$

Fick's Second Law states that the rate of change of concentration in a volume element of a membrane, within the diffusional field, is proportional to the rate of change of concentration gradient at that point in the field, as given by if

assuming diffusion coefficient, *D* is constant:

$$\frac{\partial C}{\partial t} = D\frac{\partial^2 C}{\partial x^2}$$ (3.2)

If the diffusion constant, *D*, is not a constant but depends upon coordinate and/or concentration, the Second Fick's Law is expressed as follow equation

$$\frac{\partial C}{\partial t} = \frac{\partial}{\partial x}\left(D\frac{\partial C}{\partial x} \right)$$ (3.3)

3.2 Principle of Selective Zinc diffusion

In this study, Selective Zinc diffusion is proposed to solve the issue mentioned in last chapter, which is unavoidably p-doping of InP upper cladding during the single-step epitaxy by selective area growth. In conventional SAG, DMZn is introduced during the growth of the upper cladding and InGaAs contact layer. However, in this study, the proposed selective zinc diffusion technique, DMZn is introduced after the growth. But prior to that, a 350nm SiO_2 mask is applied to the passive region to protect it from the zinc dopant. Thus, the passive components or the planar region of the integrated device is expected to be free from p-dopant in the upper cladding, or remained undoped. Depicted in Fig. 3.1 is the schematic view of such selective zinc diffusion.
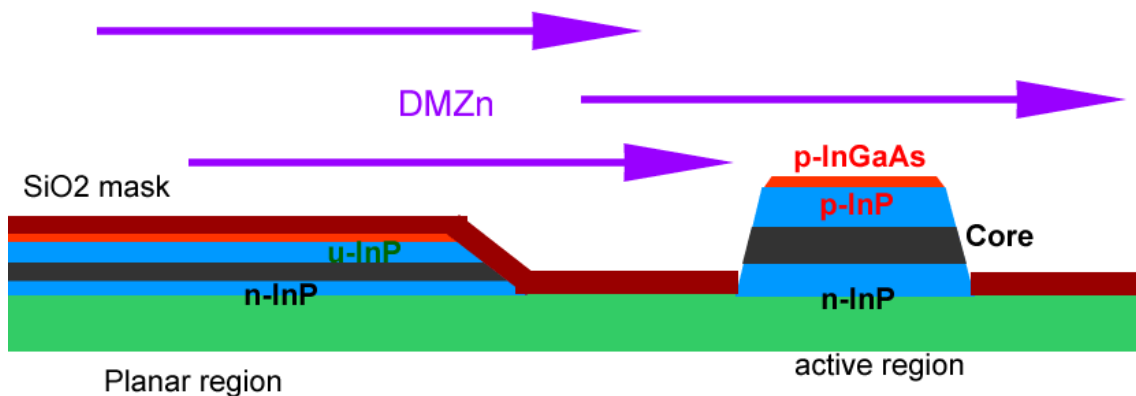

Fig.3.1 Schematic view of selective zinc diffusion. Only the active part is exposed to Zn diffusion while the passive components is protected by SiO_2 mask.

To avoid confusion, the difference between *zinc diffusion* and *selective*

zinc diffusion should be stated here. In former case, zinc is diffused directly to the whole surface of the sample wafer, which in this study, is used in fabricating zinc diffused Fabry-Perot Laser diode array (without any passive components), will be detailed in chapter 4 and 5. While, the latter one, the *selective zinc diffusion*, is the proposed method, only concerns a certain part of a wafer, typical the active parts is being zinc diffused. And the rest is protected by an electrically insulating layer such as SiN or SiO$_2$ layer. This is a concept similar to selective area growth. By such process, the active region can be successfully p-doped while the remaining passive component is remained undoped.

3.3 Zinc Diffusion Profiles

Zinc, a p-dopand in III-V material, has been commonly used, especially for InP based laser diode. However Zn is a very fast diffuser and it is very difficult to precisely control the grown-in Zn profile after epitaxy growth. [27-30] Since the final Zn diffusion front is critical to laser performance, a precise control of the Zn profile in the laser structure is important. As a result, we obtained our zinc diffusion profile thru repeated trial and error.
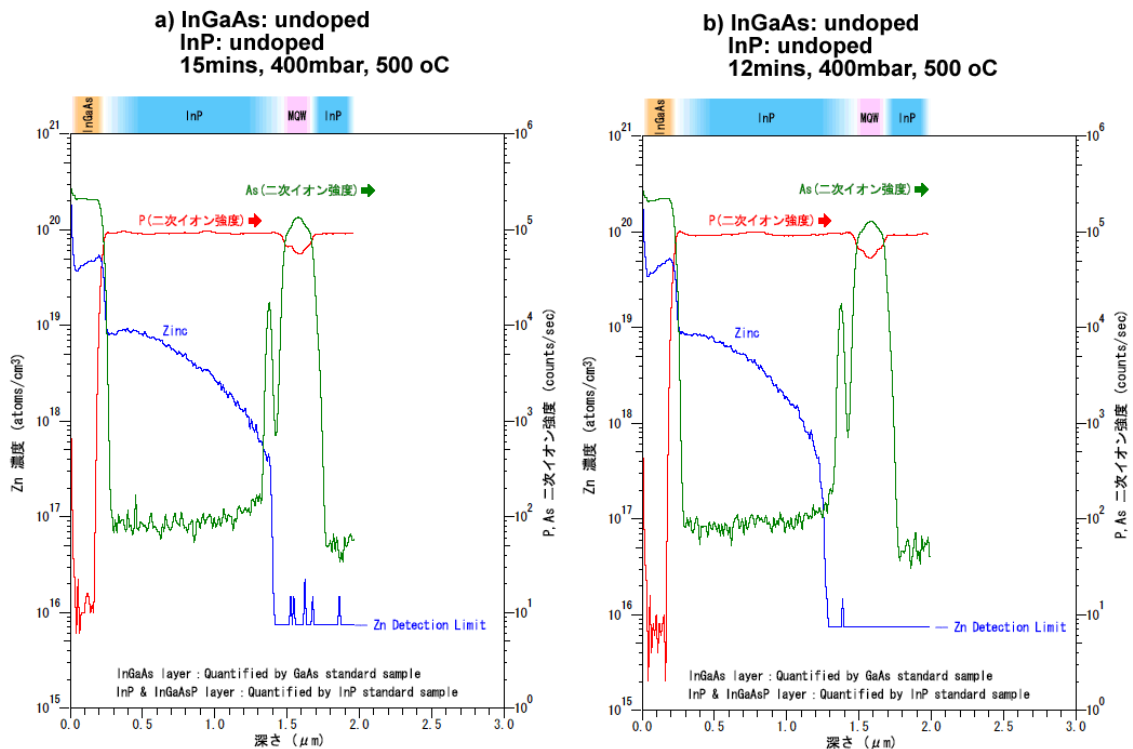

Fig.3.2 Zinc diffusion Profile of similar conditions except variable time: a) 15 mins. and b)

12mins.
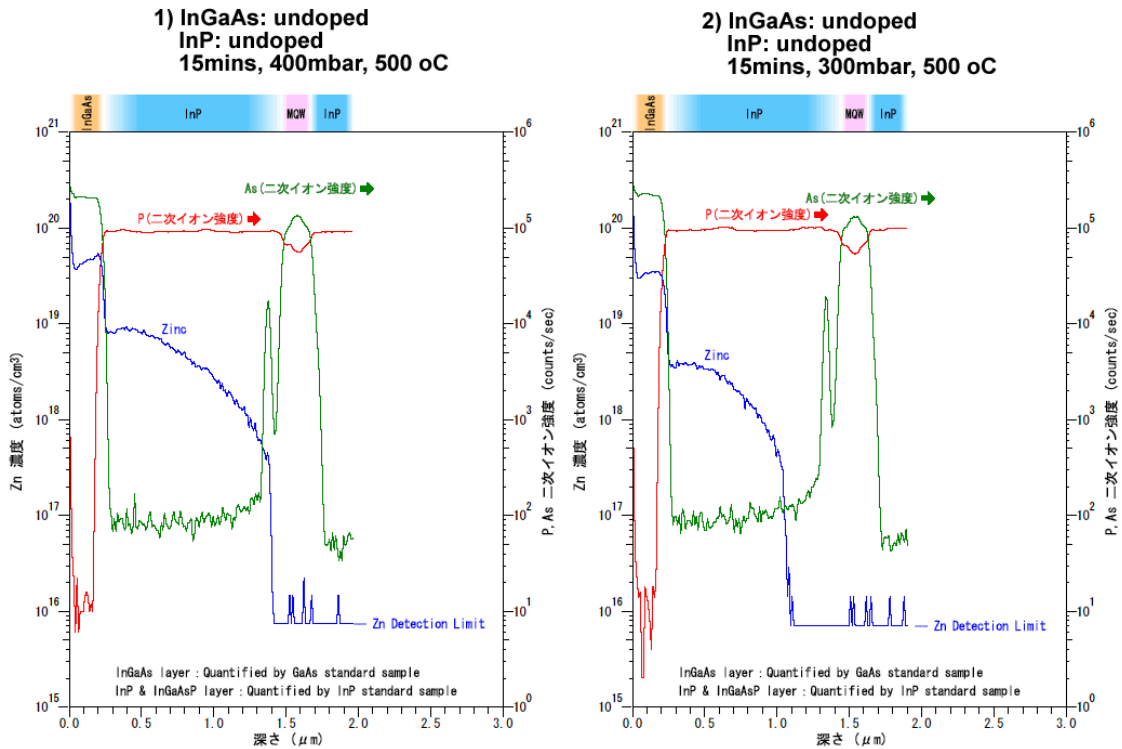
Fig.3.3 Zinc diffusion Profile of similar conditions except variable pressure: 1) 400 mbar and 2) 300mbar.

In our experiment we accomplished the Zinc Diffusion into a grown plain wafer (with 200nm of InGaAs contact layer and 1500nm of InP upper cladding above 210 core layer) via MOVPE, with carefully monitoring a few parameters including: 1) the amount of zinc inflow, 2) the temperature, 3) the pressure and 4) time. We believe by applying selective zinc diffusion based on the zinc profile we obtained, into the integrated photonic devices by SAG, we will be able to effectively reduce the propagation loss efficiently.

Fig. 3.2 and Fig 3.3 illustrate results by Secondary Ion Mass Spectroscopy (SIMS) analysis of our zinc diffused sample mentioned above. Both (a) and (b) of Fig 3.2 were diffused under similar condition except different in time. Fortunately, the zinc diffusion profile in (a) has gave us the desire result, which is 1) it has reached our target mark of penetrating the InGaAs contact and most of the Upper InP cladding while the core remain undoped, and 2) it has reached the target doping density of approximately $\sim 10^{19} cm^{-3}$ in InGaAs contact layer and, $\sim 10^{17} cm^{-3}$ to $\sim 10^{18} cm^{-3}$ in upper InP cladding layer, which is the

typical concentration for a laser to work properly. As a result, the obtained zinc profile will be used in the later fabricated actual devices by Selective Area MOVPE. In Fig. 3.3, the test was performed similar to Fig. 3.2 except alternating the pressure: (1) 400mbar and (2) 300mbar.

3.4 Zinc Diffusion Analysis

In this study, the upper InP is capped with an InGaAs contact layer, the diffusion equation for single-type material might not be entirely applicable. However for simplicity seek; the diffusion coefficient was assumed to be constant and calculated using equation 3.2, the time-dependent Fick's second law of Diffusion. C is the zinc concentration with respect to depth, x. Fig. 3.4 demonstrates the computed diffusion coefficient, D, 1.30×10^{-13} cm^2/s and 1.38×10^{-13} cm^2/s from the two zinc diffusion profiles obtained in Fig. 3.2. -
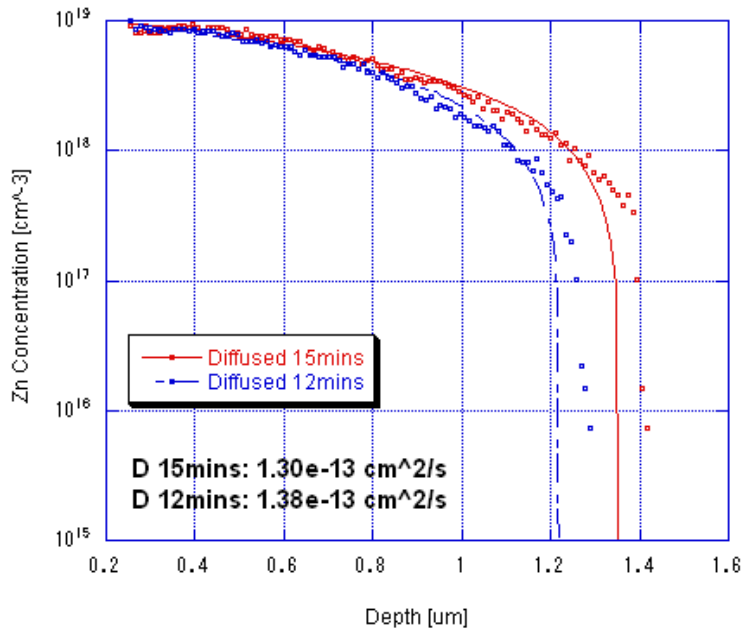
Fig.3.4 Zinc diffusion concentration extracted from the InP portions in Fig. 3.2

In general there are two common analytical solutions to the diffusion equations (or Fick's second law of diffusion): the Gaussian distribution and the Error-function solution. The former one is used when a fixed number of particles diffusing from a square concentration, while the latter is used when an infinite supply of diffusing particles from a surface. In our study, the latter one is more

appropriate. The erfc solution of Fick's law is stated as follow:

$$C = C_s erfc\left(\frac{x}{2\sqrt{Dt}}\right) \qquad (3.4)$$

where C_s is the surface concentration (cm^{-3}), x, is the diffusion depth from the surface, t is the time and D, the Diffusion coefficient. The complementary error function, *erfc* is defined as follow:

$$erfc(x) = 1 - erf(x) = \frac{2}{\sqrt{\pi}}\int_x^\infty e^{-t^2} dt \qquad (3.5)$$

SIMS data from Fig. 3.2 was extracted and fitted to error-function solution of Fick's Law. The result is illustrated in Fig. 3.5.
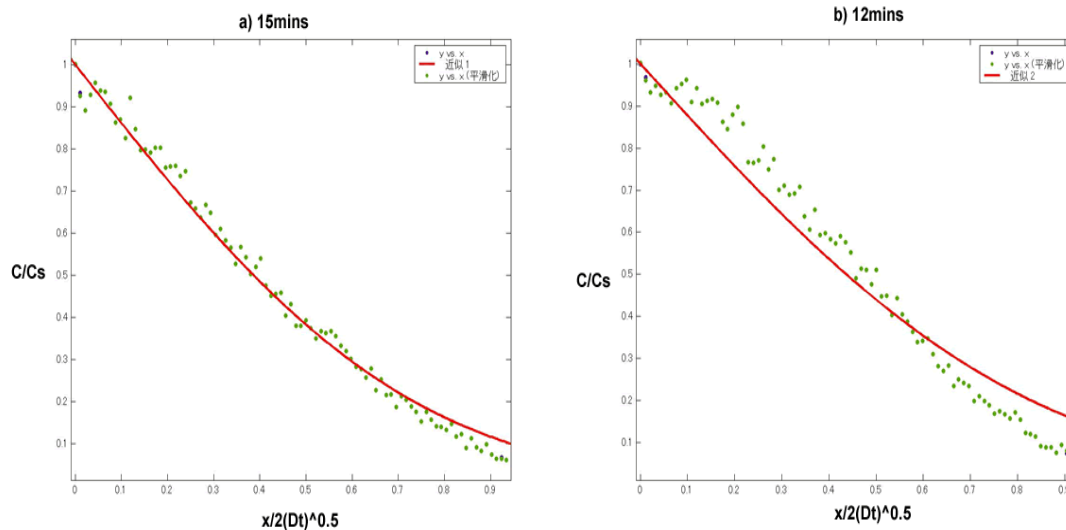
Fig.3.5 the error-fucntion solution of Fick's second law based on the SIMS data extracted from Fig.3.2.

Based on equation 3.4, it can be observed that, distance, *x* is proportional to $t^{1/2}$. This result suggest that the local equilibrium can be reached for these diffusion since the decomposition of DMZn throught the boundary layer to InP layer occurs rapidly, resulting in a constant source Zn diffusion. Depicted in Fig. 3.6 is the graph based on the diffusion distance x, against $t^{1/2}$, at 500^oC and pressure of 400mbar. The result is in good agreement with the relation of depth versus square root of time.
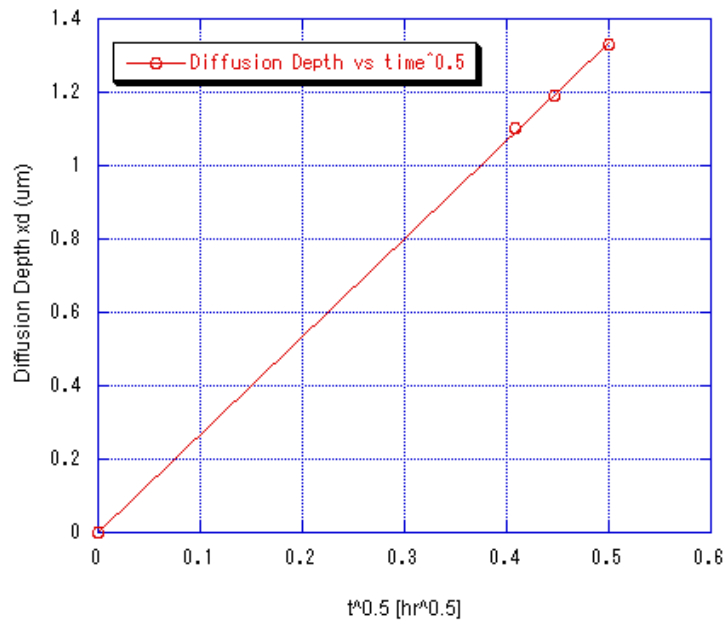
Fig.3.6 diffusion depth x, vs. $t^{1/2}$ at $500^{o}C$, 400mbar

3.5 Implementation of Zinc Diffusion

After careful study of zinc diffusion and its potential toward Selective Area MOVPE issues, the implementation state is planned to carry out. Though the original plan was to directly implement such solution into an integrated photonic device by selective area MOVPE (detail of the device is mentioned in chapter 4) However, due to some fabrication issue which is mentioned in section 4.8, and also in order to investigate the feasibility of zinc diffusion on selective area grown device, the proposed solution is first carried out separately on sole active laser device. In fact it's similar to the active components of the target integrated device, which is detailed in chapter 4, excepted instead of fabricating low-yield Distributed Feedback (DFB) laser diode arrays, Fabry-Perot (FP) laser diode arrays were fabricated. This fabricated *zinc diffused* sample was then compared to the performance of a conventional single-step-epitaxy grown sample, or *zinc doped* sample as we named it. Both samples are illustrated in Fig 3.7: (a) is the zinc doped sample with 15μm gaps sandwiched between SAG regions, and (b) is the zinc diffused sample with similar structure. For more details of the fabrication procedure, refer to Chapter 5. The black spots sandwich between the SAG mask (encircled in red dashed lines) are the actual spots were SIMS analysis carried out. The results are illustrated in Fig. 3.8: a) zinc doped

sample and b) zinc diffused sample. It is observed that the zinc diffusion profile of a) is more linear in the InP upper cladding region compare to the one in b). The zinc diffusion profile in b) is observed behaving quite similarly to those conducted previously, such as results in Fig. 3.2. Fig. 3.9 illustrates the comparison of both diffusion profiles from Fig. 3.9.
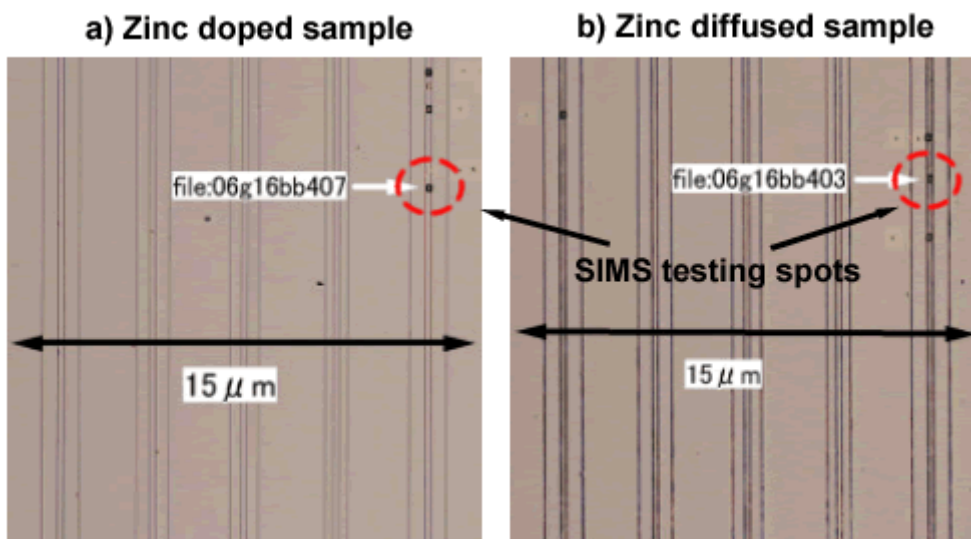
Fig.3.7 Secondary Ion Mass Spectroscopy (SIMS) analysis is carried out in a SAG region with 15μm gap on both a) zinc doped sample and b) zinc diffused sample.
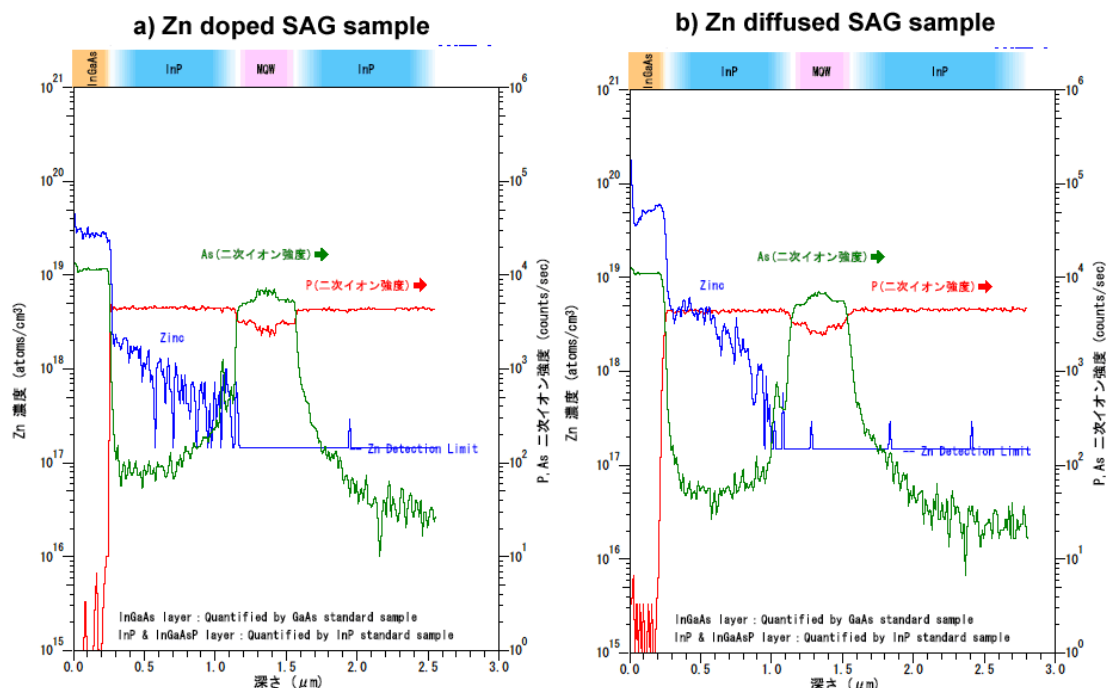
Fig.3.8 SIMS results obtained from the SAG region illustrated in Fig. 3.7 a)zinc doped sample

and b) zinc diffused sample.
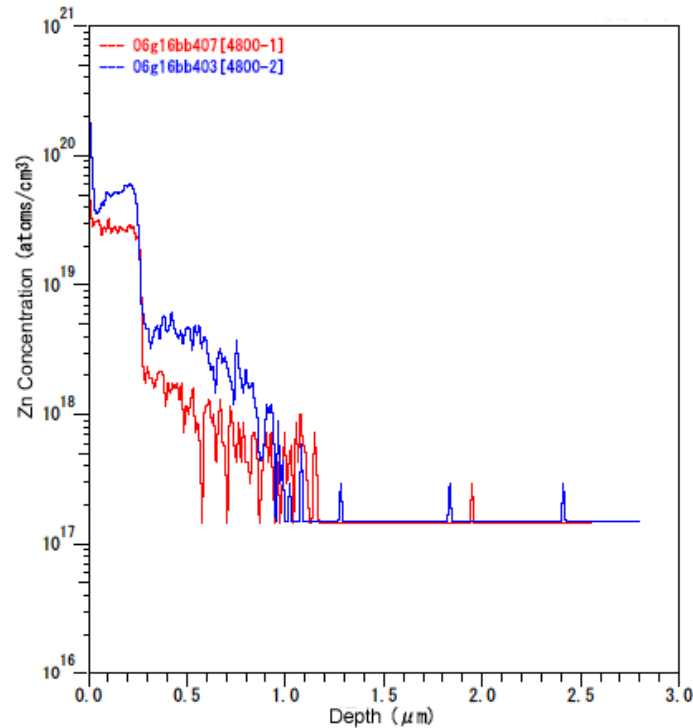
Fig.3.9 Comparison of both Zinc diffusion profiles (red) zinc doped sample and (blue) zinc diffused sample.

3.6 Conclusion

In this chapter, the selective zinc diffusion, as a solution, for selective area MOVPE Monolithically Integrated Photonic Devices has been investigated.

The principle of selective zinc diffusion and Fick's law of diffusion equations were first studied and detailed in the first part of this chapter. Then ideal zinc diffusion profiles were obtained thru repeated tests and the results are illustrated in Fig 3.2. Diffusion coefficients were obtained from extracting the said diffusion profiles. And Error-function solution of diffusion equations were used to fit the SIMS data obtained from the same profile.

In the last part of this chapter, the implementation of zinc diffusion is carried out on a separately selective area grown laser diode array. The fabricated device was then compared to another zinc doped sample thru

Secondary Ion Mass Spectroscopy (SIMS) analysis. The InGaAs contact layer of both samples were observed with doping density of approximately $\sim 10^{18} cm^{-3}$ to $\sim 10^{19} cm^{-3}$, meanwhile, $\sim 10^{17} cm^{-3}$ to $\sim 10^{18} cm^{-3}$ of doping concentrations were observed in both upper InP cladding layer as well. These promising results for typical laser doping level support the feasibility of zinc diffused device, and further, the potential of selective zinc diffusion in selective are MOVPE monolithically integrated devices.

4. Design Consideration

As mentioned in the previous chapter, selective zinc diffusion is a solution we proposed in order to solve a specific selective area growth issue, however before implementing such proposal, a selective area grown integrated device is needed. Thus, we first developed such device before we implemented the proposed selective zinc diffusion. Such device is named the *Integrated 4-Channel DFB Laser Array with Optical Combiner for 1.55µm CWDM Systems by Selective Area MOVPE*. [31] The passive and active components have also been separately studied and are detailed from section 4.3 to 4.6.

4.1 Monolithically Integrated 4-Channel DFB Laser Array with Optical Combiner for 1.55µm CWDM Systems by Selective Area MOVPE

WDM has played a key role in telecommunications for many years, and matured sufficiently that Dense Wavelength Division Multiplexed (DWDM) systems have been widely demonstrated at aggregate bit rates up to and beyond 1Tb/s along a single fiber. However, despite the high performance of DWDM, there remains much interest in lower cost short haul links for use in the access and metro areas of the telecommunication network. And Coarse Wavelength Division Multiplexed (CWDM) system gains its value in the market since it has much larger channel spacing (20nm as compared to 0.4nm to 1.6nm for DWDM) with few channels, thus capable of using uncooled, unstabilized, and directed modulated laser transmitters as well as inexpensive passive CWDM components. [32-35] Conventionally, CWDM laser diodes is built in hybrid integration, which is large in size, high package cost and require precise fiber alignment. [36-37] The CWDM standard defines maximum of 18 channels from 1270nm to 1610nm, however the current vendors' emphasis is on 4 or 8 channels system centered around 1550nm to minimize fiber loss and to avoid the 1380nm water peak present in most deployed fiber. In our study, we focused on 4 channels system, and determined to fabricate an integrated four channels DFB laser diode with 4x1 Multimode Interference (MMI) Combiner for 1.55µm CWDM system. The four channels of laser diode are 1530nm, 1550nm, 1570nm

and 1590nm, which are based on ITU-T standard. The schematic diagram is illustrated in Fig. 4.1. The 4 DFB lasers will be fabricated within the 4 SAG regions, which have been detailed in chapter 2. While the remaining MMI coupler and passive waveguides will be made upon the passive regions of the integrated device. The distance designed between each channels were set to 250μm to avoid crosstalk.
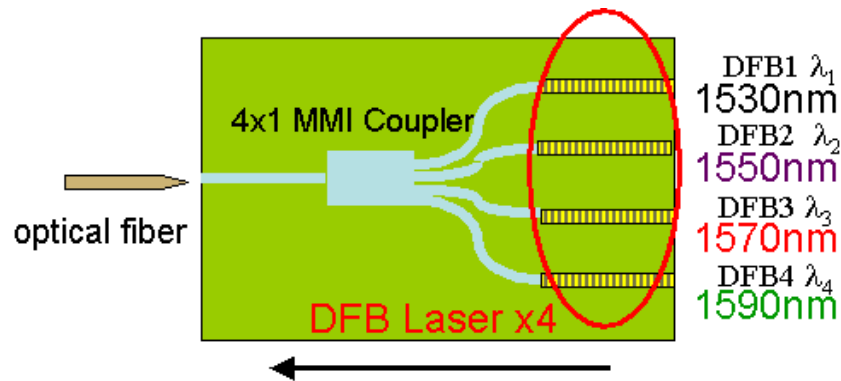
Fig.4.1 The Schematic diagram of the Monolithically Integrated 4-channels DFB laser array by Selective Area MOVPE for 1.5μm CWDM system. The integrated device mainly composes of 4 DFB laser array in 4 different lasing spectra and an 1x4 MMI Combiner.

4.2 Principle of Fabry-Perot (FP) Laser and Distribute Feedback (DFB) Laser

The Fabry-Perot laser operates according to the basic laser principles: current pumping leads to stimulated and amplified light emission at a wavelength defined by the bandgap of the material in the laser active layers, which leads to laser oscillation as the optical field reflects from two parallel mirrors which form the Fabry-Perot cavity. The optical field is confined by the structural definition of the laser strip. The cleaved mirrors reflect to first order independently of wavelength and a combination of the peak wavelength of the gain spectrum and resonant wavelength of the cavity determines the longitudinal laser mode. Lateral mode width and structure is defined by the width and nature of lateral guiding where hole burning and temperature effects are also of relevance. The left image of Fig.4.2 is a typical ridge Fabry-Perot Laser.

Meanwhile, in Distributed Feedback (DFB) Laser, though similar to a Fabry-Perot (FP) Laser, feedback is required for oscillation. However in DFB laser, the optical feedback is obtained by the periodic variation of the effective

refractive index of a corrugated optical waveguide inside the laser cavity or so called the grating structure. The periodic index variation causes a very wavelength-selective feedback. For this reason, DFB is preferred in optical communication systems due to its excellent side-mode suppression, low threshold current and good coupling efficiencies with the waveguide or fiber-optic system to which the laser is attached. Maximum reflectivity of the rating occurs around the Bragg wavelength λ_B which can be defined by the following equation:

$$\lambda_B = 2\Lambda n_e \qquad (4.1)$$

where Λ is the period of the grating or pitch grating and n_e is the effective refractive index of the waveguide without grating. The right image of Fig.4.2 is schematic representation of a DFB laser. [38-42]
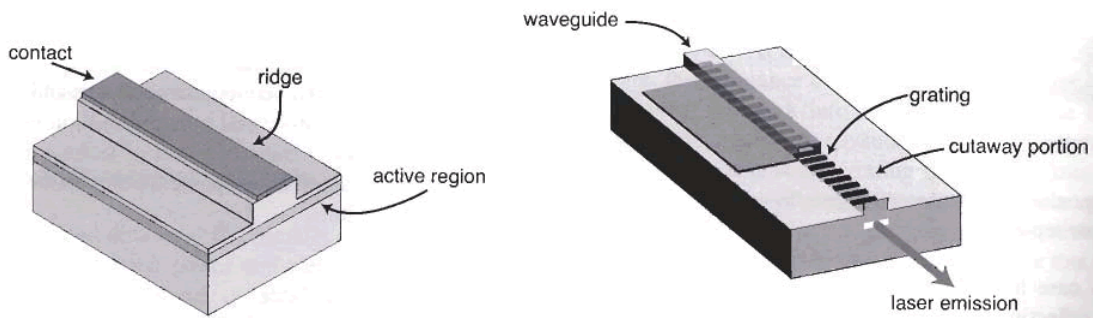
Fig.4.2 (Left) a ridge Fabry-Perot Laser with a waveguide etched into the upper cladding region. (Right) Schematic representation of a distributed feedback (DFB) laser. The pumped and grating regions are concomitant such that the grating is buried inside the semiconductor. A cutway view shows the grating in more detail.[42]

4.3 Principle of Multimode Interference (MMI) Coupler

Since the designing of the MMI coupler used in the integrated device mentioned above is one of the main focuses in this research, this subsection is dedicated to the detailing of 4X1 MMI combiner.

MMI couplers are optical integrated components which are capable of

splitting and combining multiple optical beams while remained low-loss, compact in size and large fabrication tolerance. The operation of MMI coupler is based on the self-imaging principle, which is the property to reproduce an input field profile in single or multiple images at periodic intervals along the propagation direction of the guide. In integrated optics an MMI is determined by its geometry. It typically consists of one or several narrow input ports, which are guided into a wider waveguide. After a certain interval the wider waveguide is stopped and one or several output waveguides are appended to extract the light. Physically, at the transition from the narrow to the wider waveguide, the optical mode of the input guide is adiabatically decomposed into the eigenmodes of the wider waveguide. The different new eigenmodes of the wider waveguide then propagate each with its own propagation velocity along the wider waveguide. Depending on the position along the wider waveguides, their superpositions form new interference patterns. At some periodic intervals the input profile is reproduced and can be extracted into new output waveguides.

(a)

(b)
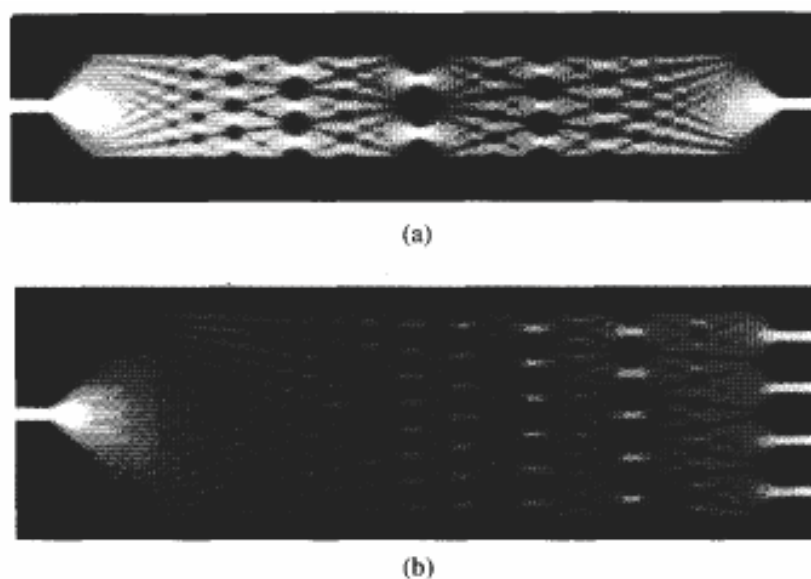
Fig.4.3 Theoretical light intensity patterns corresponding to (a) single-input symmetric interference mechanism and (b) a 1-to-4 way splitting Multimode waveguide. [43]

In generally speaking, there are two major types of MMI: *NXN general MMI* and *Special over lap MMI*. Special over lap MMI can be further classified into *1XN MMI*, or *symmetric interference MMI*, and *2XN MMI*, or *paired MMI*. "N" denotes the number of input and/or number of output of a MMI. Since in this research, we needed to combine the four DFB laser into one single output, so a

4X1 combiner is required. Thus, a 1XN MMI coupler is chosen since it fits our requirement. Due to the duality of MMI, by designing the proper dimension of a 1X4 MMI splitter, we can get our 4X1 combiner at the same time. The power at the output of either 1X4 MMI splitter or combiner is expecting to be approximately 1/4 of the original input power. Fig. 4.3 illustrated the theoretical light intensity patterns a 1x1 and a 1x4 MMI coupler. [43-47]

4.4 Design of 4X1 MMI Combiner

The most crucial consideration in designing a MMI coupler is to determine the coupler length L_{MMI} with respect to the width, W_{MMI}, and can be expressed as the following equations which are only applicable to 1XN symmetric interference MMI:

$$L_{MMI} = \frac{1}{N}\left(\frac{3L_\pi}{4}\right) \tag{4.2}$$

$$L_\pi \approx \frac{4n_r W_{eff}^2}{3\lambda_0} \tag{4.3}$$

$$W_{eff} = W_{MMI} + \left(\frac{\lambda_0}{\pi}\right)\left(n_r^2 - n_c^2\right)^{-1/2} \tag{4.4}$$

Where N is the number of images-fold, L_π is the beat length, W_{eff} is the effective width of the MMI, n_r and n_c denote the ridge and cladding effective refractive index respectively at free space wavelength λ_0. [48]

In this study, the W_{MMI} were first set to 30nm, as to compensate the 4 input waveguides with approximately 8µm apart from each other while each waveguide is 2.5nm in width. Simulation is carried out using Beam-Propagation Method (BPM) analysis. First, a 1x4 MMI splitter is simulated to determine the optimum L_{MMI} for the MMI coupler. As a result, 530nm is obtained as the optimum L_{MMI}. Then a 4x1 MMI combiner is simulated using the same W_{MMI} and optimum L_{MMI} as mentioned above. Fig. 4.4 and 4.5 illustrated the simulation result of a 1X4 MMI splitter and a 4X1 MMI Combiner. The duality of the MMI coupler can be observed thru the two figures, as the output power of both MMI

couplers are approximately equal to 1/4 of the input power as expected.
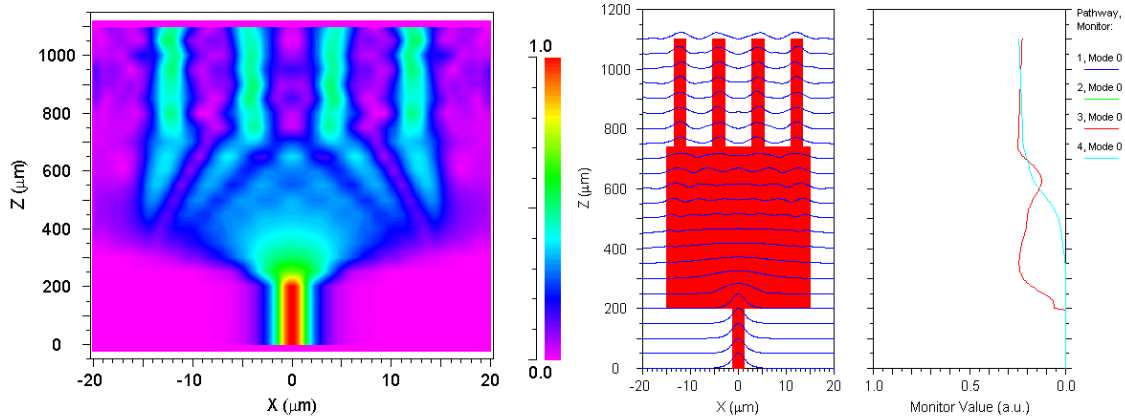
Fig.4.4 (Left) BPM Simulation result of the field amplitude as a function of x and z, (Middle) optical path way and (Right) output intensity of a 1X4 MMI splitter. It is observed that the output power is equal to approximately 1/4 of the input power from the right figure.
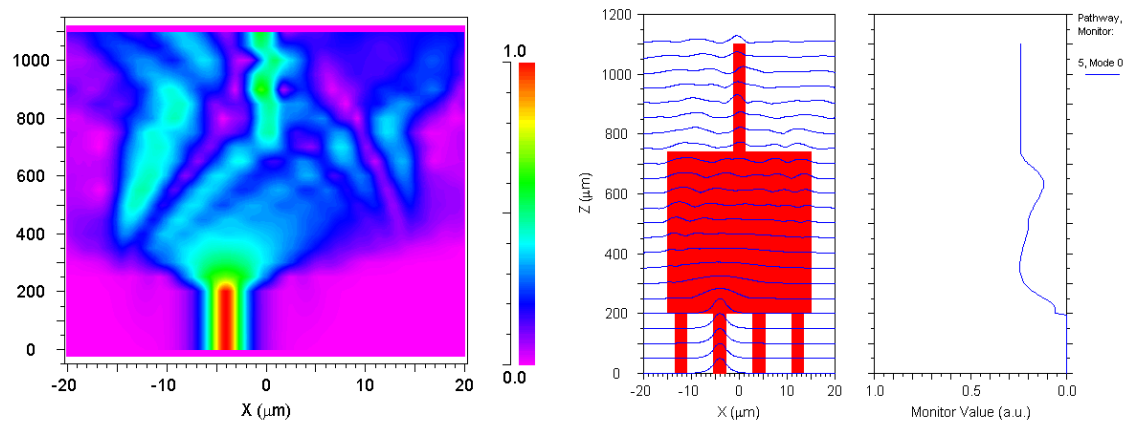
Fig.4.5 (Left) BPM Simulation result of the field amplitude as a function of x and z, (Middle) optical path way and (Right) output intensity of a 4X1 MMI combiner. The duality of a MMI coupler can be observed as e output power is equal to approximately 1/4 of the input power from the right figure.

In reality, since our device is fabricated using chemical wet etching, the actual dimension might vary from the designed dimension. For this, we conducted some tolerance simulation thru BPM Analysis. [49] The results are illustrated in the next two figures. Fig. 4.6 illustrated the MMI width tolerance starting from 24µm up to 36µm, with default dimension as 30µm; we realized the width tolerance is estimated at around 30 ± 0.85µm. Fig. 4.7 illustrates MMI

length tolerance, with 530μ m long MMI, the length tolerance is estimated at 530±29μm. However in the final design, we decided to make use of three different MMI lengths for reference: 490μm, 530μm, and 570μm.
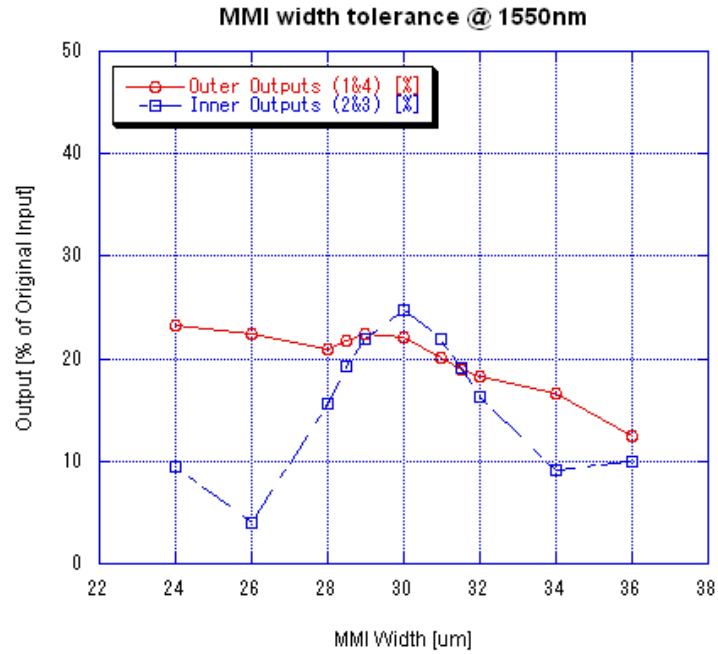
Fig.4.6 Width tolerance of MMI measured from 24μm up to 36μm: 30±0.85μm
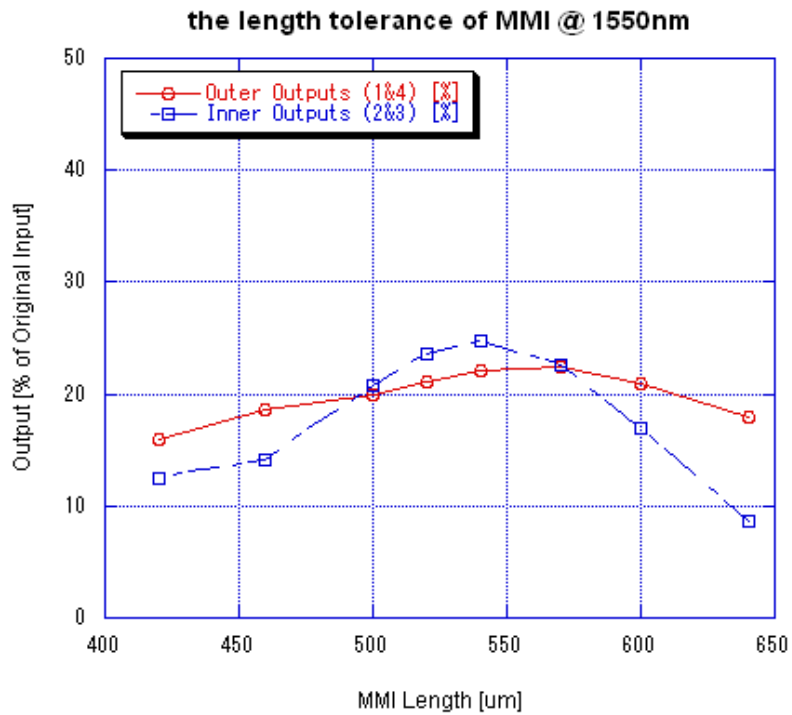
Fig.4.7 Length tolerance of MMI measured from 420μm up to 640μm: 530±29μm

4.5 Design of S-bend Passive Waveguide

In order to avoid crosstalk between each of the 4 channels of the integrated device, 250µm distance is given between each channel. On the other hand, since only 8µm distance is set between each input port of the MMI coupler, the only way to link the two sets of components is via S-bend waveguides. Thus we designed two inner and two outer S-bend waveguides in total. For the inner one with radius of curvature of 2757µm, we denoted it as R2757, and the outer one as R1000, for have radius of curvature of 1000µm. The width is designed to 2.5µm, same with the width of output straight waveguide and ridge waveguide of the active components.

Depicted in Fig. 4.8 are the results of both R2757 and R1000 S-bend waveguides obtained thru BPM analysis. (a) and (c) are the results of R2757 in 2-D and 3-D respectively, while the same goes with b) and d) (R1000's result) However due to the limitation of the simulation tool, the optical output is observed to be very low, which in reality should be higher than the computed results.
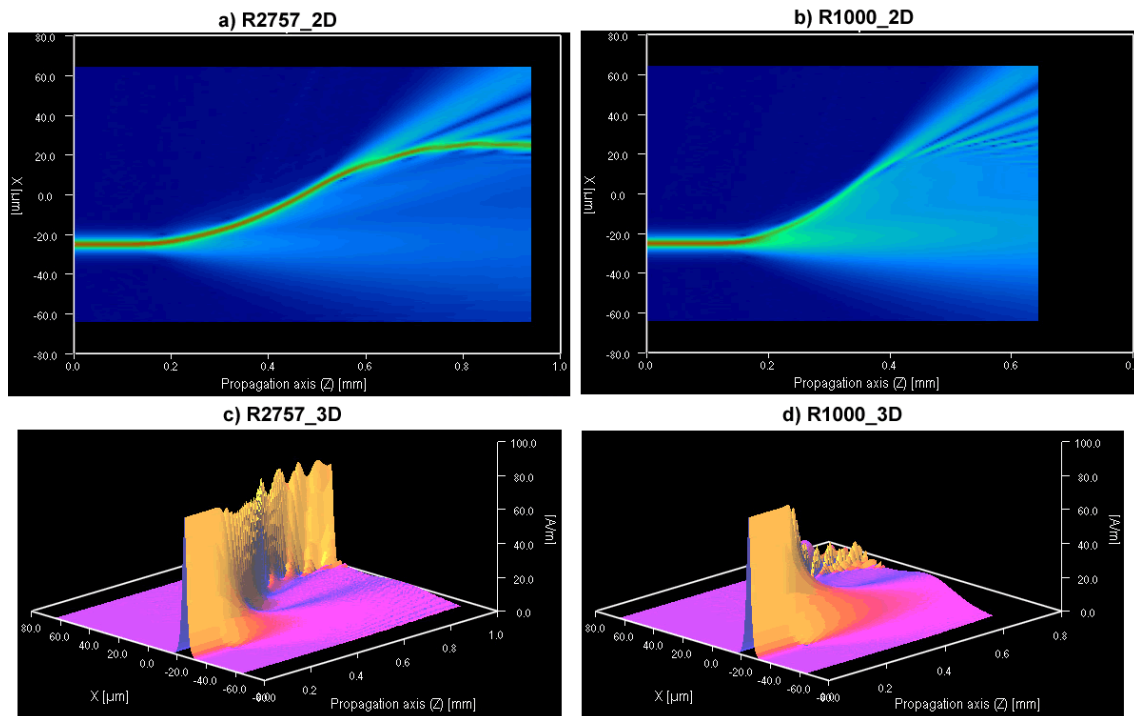
Fig.4.8 BMP analysis of S-bend waveguids a) and c) are R2757 results in 2-D and 3-D, while b)

and d) are R1000 results in the same way.

a) S-bend with variable Radius v.s. Output @ 1550nm

b) S-bend with variable Radius v.s. Loss @ 1550nm
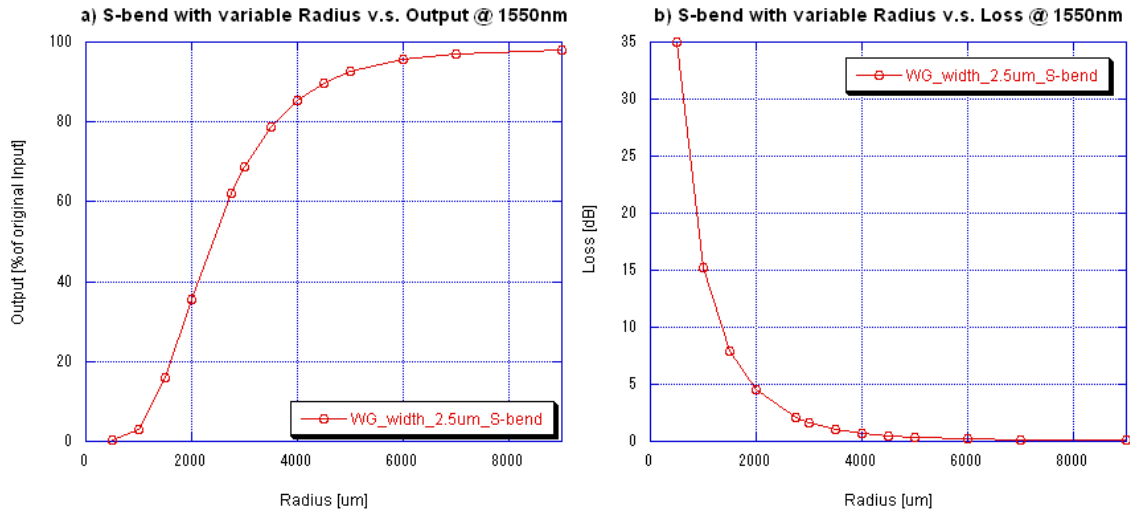
Fig.4.9 Results based on BPM analysis: as the radius of curvature increases, a) the optical power increases, and b) the optical loss decreases.

a) S-bend Offset tolerence @ 1550nm

b) S-bend Offset Position v.s. Loss @ 1550nm
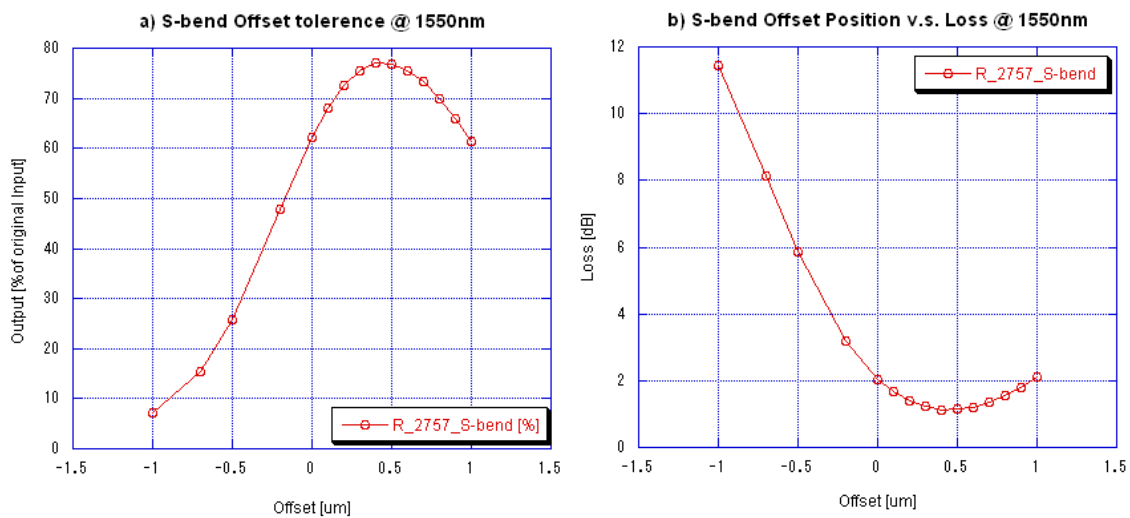
Fig.4.10 offset tolerance of R2757. Offset is only applicable when dry etching is used, since wet-etching can not give precise sharp edges like dry etching does.

Fig. 4.9 illustrates the results based on BPM analysis using 2.5um wide S-bend waveguides and gradually increases the radius of curvature. As it was expected, as the radius of curvature increases, the optical power also increases, and optical decreases. This gives us an insight that in the future design, if we could decrease the SAG region distance, like making it more compact, we could compensate S-bend waveguide with higher radius of curvature due to lower optical loss. In Fig. 4.10, offset tolerance of R2757 with 2.5μm width is

demonstrated. We can concluded that but including offset in the S-bend design (approximately 0.4μm offset), the optical loss is greatly improved. However, this is only applicable using dry-etching since the wet-etching can not give precise sharp edges like dry-etching does. Fig 5.3 in the next chapter illustrates the difference between dry and wet-etching.

4.6 Design of Selective Area Grown DFB Laser Diodes

The design of SAG regions has been detailed in chapter two. The essence of SAG lies on the ratio of gap width to mask width (W_m/G_m), which is directly related to the bandgap energies once fabricated. These ratios were obtained thru repeated trials and errors. In this study, the 5 bandgap energies (1 passive bandgap for the passive components and 4 active bandgap for the 4 different wavelengths laser diodes) and the ratio has been summarized in table 4.1. The photoluminescence profile of the 5 bandgap energies required by our SAG Laser diode array is also the same profile we demonstrated in (b) of Fig. 2.7 of Chapter 2.

W_m/G_m ratio	Wavelength obtained
1.6	1530 nm
2.1	1550 nm
2.5	1570 nm
2.9	1590 nm
Planar	1440 nm

Table.4.1 the W_m/G_m ratio with respect to wavelength obtained.

4.7 The Fabricated Integrated Selective Area Grown (SAG) DFB Laser Diode Array with 4X1 MMI Combiner

Depicted in Fig. 4.11 is the microscopic view of the fabricated Monolithically Integrated 4-Channel DFB Laser Array with Optical Combiner for 1.55μm CWDM Systems by Selective Area MOVPE. The total dimension of the whole integrated device is approximated 2.8mm by 1.25mm. The whole device composed of 4 channels (1530nm, 1550nm, 1570nm and 1590nm) of DFB laser fabricated by SAG, 4 S-bend waveguides with radii of 1000μm and 2757μm for the outer and inner S-bend waveguides respectively, a 530μm long 4 to 1 MMI

combiner and followed by a straight output waveguide.

Depicted in Fig. 4.12 is the simultaneous lasing spectrum of one of the fabricated integrated SAG DFB Laser diode array sample, which lasing at 1521.3nm, 1541.4nm, 1563.9nm, and 1580.6nm. The separated lasing spectra are illustrated in the right of Fig4.13, the side-mode suppression rates (SMSR) are 33.2dB, 30dB, 36.4dB and 36.2dB for channel 1 to 4 respectively. The I-L curves of the same device are illustrated in the left of Fig 4.13, the threshold currents (I_{th}) are 64mA, 58mA, 63mA and 57mA for channel 1 to 4.
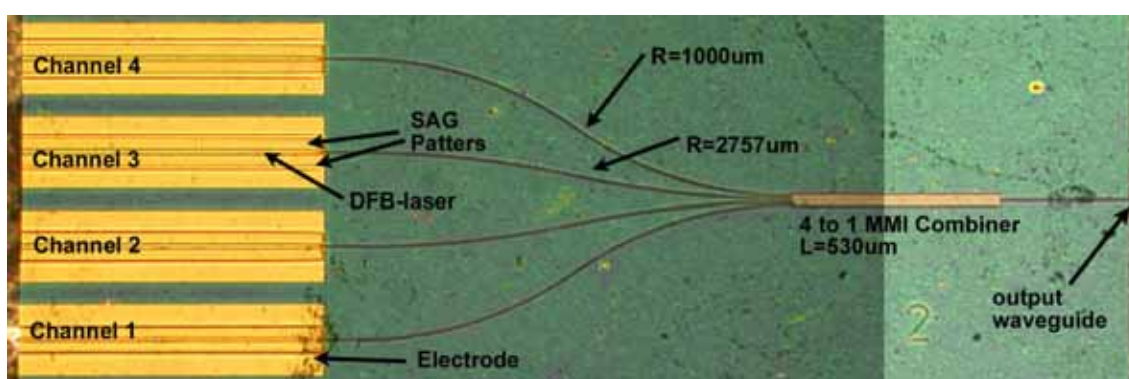
Fig.4.11 Microscopic view of the Integrated 4-Channel DFB Laser Array with Optical Combiner for 1.55µm CWDM Systems by Selective Area MOVPE. The total dimension of the device is around 2.8mm by 1.25mm
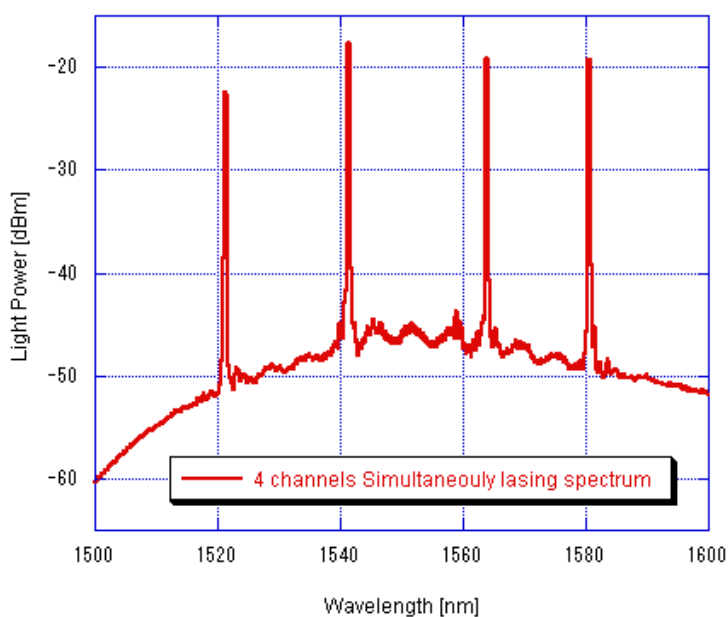
Fig.4.12 sample of simultaneous lasing integrated SAG DFB Laser diode.
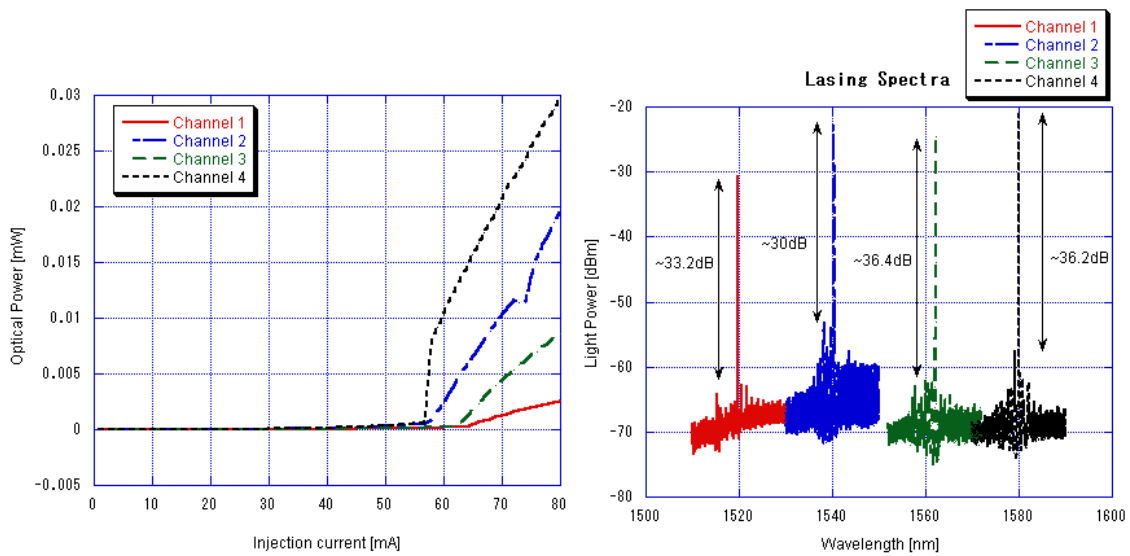
Fig.4.13 (Left) the I-L characteristics of the 4-channels from the same device of fig. 4.11 (Right) the separated lasing per channel from the same device of fig. 4.11 the SMSR of each channels is also illustrated.

4.8 Yield issue with the Fabricated Integrated SAG Device

As mentioned is the section 4.7, although the Monolithically Integrated 4-Channel DFB Laser Array with Optical Combiner for 1.55μm CWDM Systems by Selective Area MOVPE has been fabricated. But the yield was not exactly high. Out of total of fourteen sets that have been cleaved and tested. Only 57% of channel 1, 50% of channel 2, 29% of channel 3 and 21% of channel lased. Simultaneously lasing device's yield is even less than 10% of the total tested samples. [31]. Thus, this issue of yield held back the researchers' attempt of directly applying the proposed selective zinc diffusion into the said integrated SAG device. Since, the main objective of this research remains on study on reduction of passive waveguide's loss by selective zinc diffusion for SA-MOVPE Integrated device. We decided to first apply the zinc diffusion into a Selective Area Grown Fabry-Perot Laser diode (SAG FP LD) array instead of DFB LD. Hence, we fabricate the active and passive components from the original design separately. As for the active component, SAG FP LD is grown first with undoped upper InP cladding and InGaAs contact layer, followed by zinc diffusion upon the samples. On the other hand, a conventional SAG FP LD was being fabricated so to compare the performance with the former produced device. For the better understand, the former one is named *zinc diffused* sample, while the latter one

as *zinc doped* sample. Meanwhile, passive parts were also going to be separately fabricating. Since as discussed in the previous chapter, the passive component of a Selected Zinc Diffused photonic integrated device is expected to be free from p-dopant in the upper cladding or remained undoped. In order to determine how much different between a doped passive waveguide (p-doped in the upper InP cladding) and an undoped passive waveguide (u-doped upper InP cladding), the separating of fabrication of the passive part is necessary. For easier understanding, we denoted the conventional selective area grown passive waveguide as *doped waveguide*, and the other one as *undoped waveguide*. The fabrication process of both passive and active components was discussed in the next section.

4.9 Conclusion

In this chapter, the overall design consideration of the Monolithically Integrated 4-Channel DFB Laser Array with Optical Combiner for 1.55μm CWDM Systems by Selective Area MOVPE has been detailed.

First, active components such as DFB laser diode arrays and passive components such as multimode interference (MMI) coupler and S-bend passive waveguides have also been studied and investigated. Beam-Propagation Method (BPM) analysis was used to simulate the performance of the mentioned passive components and tolerances were calculated from the data extracted. With regards to the design of MMI coupler: 30μm in width MMI by 530μm in length, the width tolerance is measured to be 30 ± 0.85μm, while the length tolerance is measured to be 530 ± 29μm.

Secondly, the fabricated integrated device by selective area MOVPE is illustrated, along with simultaneous lasing spectrum and the threshold currents of each of the separate channels. Though these threshold currents (I_{th}) are measured at 64mA, 58mA, 63mA and 57mA for channel 1 to 4 separately, it required much higher bias current for the simultaneous lasing mainly due to thermal crosstalk. These bias currents are recorded as 120mA, 100mA, 115mA and 100mA for channel 1 to 4 respectively with heatsink temperature of 12°C. It is observed almost twice from the separate threshold current.

Lastly, the low yield issue is stated, at the end of this chapter. As it is well known, that DFB lasers are more complex to fabricate than FP lasers. Most of this added complexity is due to the grating mirrors: the grating shape, position and period must be accurately determined to yield a laser with the desired output characteristics. These factors contribute mostly to the low yield of DFB lasers. For this reason, we separately fabricated the active and passive components which are going to be detailed in next chapter.

5. Fabrication and Processing Technologies

As mentioned in the last section of chapter 4, although the Monolithically Integrated 4-Channel DFB Laser Array with Optical Combiner for 1.55µm CWDM Systems by Selective Area MOVPE has been realized, but due to the low yield issue, the researchers think extra precaution need to be taken. One of such precautions is that instead of directly fabricating such SAG integrated device with the proposed method of selective zinc diffusion, two things need to be confirmed prior to that. One, we know the p-doped InP material in a passive waveguide bring propagation loss to the device, but we needed to confirm how much is this loss. The better way is to compare it with one using undoped InP material. And the second thing we need to confirm is the feasibility of fabricating a selective area grown laser diode array similar to the one of the integrated SAG LD. So in order to achieve such objective, the passive and active components needed to be fabricated separately. For the passive components, we called one using p-doped InP passive waveguide as a *doped* waveguide, otherwise an *undoped* one, And for active one we called the conventional grown SAG LD as *zinc doped* LD and the one using zinc diffusion as *zinc diffused* LD. But doing such precaution, we hope it can give us a clearer picture of the whether selective zinc diffusion can help reducing loss in a PIC by SAG.

The following subsection gives the details of the fabrication processes starting from the epitaxy.

5.1 Epitaxy

The general flow of fabrication process is illustrated in Fig. 5.1. Since we wanted to maximize the efficiency of the MOVPE equipment, on a single substrates, we divided it into four main parts, two for passive waveguides fabrication, and two for active LD arrays. In the mentioned figure, P denoted the one for passive use, while A denoted for active use.

First the two portions for active parts has been separated and sputtered

with 80nm SiO$_2$ film, and the film is patterned with photomask lithography and the patterned is transformed by buffered hydrofluoric acid (BHF) etching. Then the photoresist is removed with Stripper 106 solution and rinsed with heated Iso-propanol (IPA) a few times to cleanse the remaining of stripper solution. After careful sulfuric acid (H$_2$SO$_4$) assisted cleaning to remove any oxidized layer, all the four portions of samples were put into the MOVPE reactor for epitaxy growth.
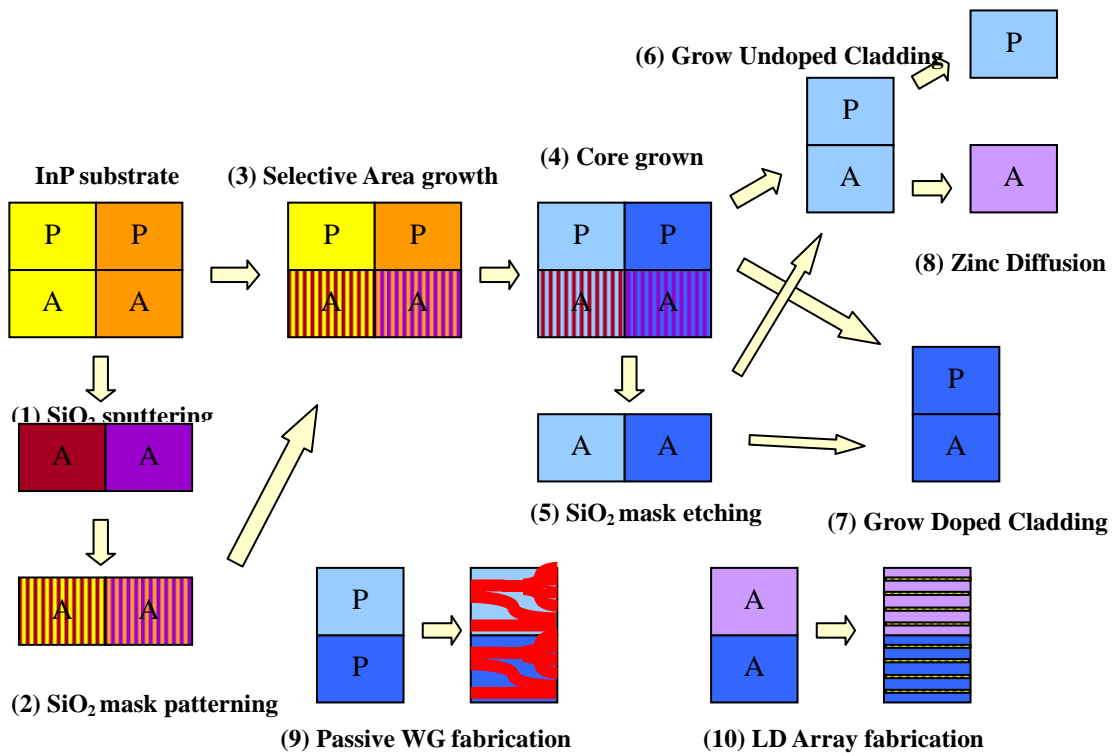
Fig.5.1 General Flow of fabrication process. P: for passive WG fabrication, A: for active LD arrays fabrication

Unlike the usually single step epitaxy which used by the SAG, in this study, the core was first grown before an extra step of clad growing. This step can be better understood with the illustration in Fig 5.2. For structure details, refer to table 5.1 and table 5.2. While 5.1 indicates the epitaxy structures up to core for all samples (both passive and active used), Table 5.2 shows the structure of the upper cladding and InGaAs for ohmic contact, the main difference between doped and undoped one is injecting TMZn during MOVPE, we included TMZn in the former one and none in the latter.
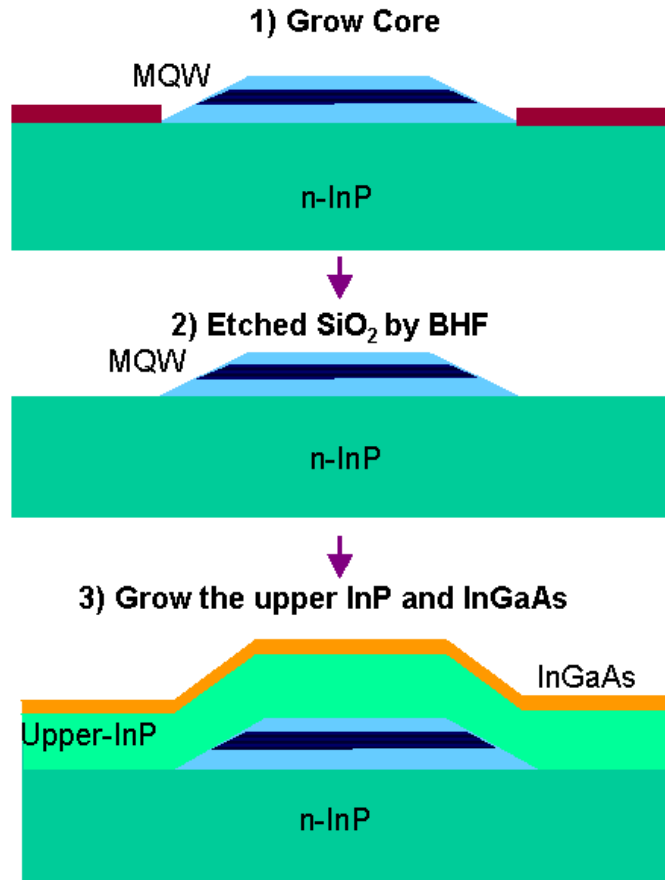
Fig.5.2 The two-step SAG epitaxy growth. 1) core is grown within the SAG region, 2) the SiO₂ masks are etched away using BHF 3) the growing of upper InP cladding and InGaAs contact layer.

After the core was grown, the active samples were taken out from the MOVPE reactor and SiO$_2$ masks was etched away using BHF before growing the upper cladding thereafter. There are a few reasons of doing this extra instead of the one step epitaxy growth usually used by SAG. First reason is to ease waveguide patterning after the growth. Since from our experience, usually Selective Area MOVPE devices has quite uneven surface due to different height in different SAG region (since same growth is applicable to both core and cladding thickness). In fact, this increases the difficulty when doing photolithography for the waveguide patterning because of the uneven surface height. Thus, by making each SAG region has uniform cladding thickness, the only difference between each channels would be the core thickness which is tens of nanometers. In our LD, there are 5 bandgap energies including planar region, by doing such extra step, it indeed gave us a more even surface, but with

a price, which is the cost brought along with additional MOVPE growth step. This makes it a major drawback of doing such extra step. And the second reason of separating clad and core is because it is crucial for zinc diffusion. Otherwise, the zinc dopant might penetrate into the core of the thinner upper cladding, while others might be lack due to different cladding thickness. We took this into our major concern of applying the extra step.

Epitaxy Layers		PL peak [nm]	Thickness[nm]
u-InP	Buffer cladding	918	20
u-Q1.25	Upper SCH	1222	69.6
u-InGaAsP	Well (x5)	1536	6.7
u-Q1.25	Barrier (x4)	1222	8.7
u-Q1.25	Lower SCH	1222	69.6
n-InP	Lower Cladding	918	182
n-InP	Substrate	918	-------

Table 5.1 Epitaxy structure and parameters of the core at the planar region

Epitaxy Layers		PL peak [nm]	Thickness[nm]
p-InGaAs / u-InGaAs	Well (x5)		117.5
p-InP / u-InP	Upper cladding	1222	1078
p-Q1.25 / u-Q1.25	Etch-stop	1222	69.6
p-InP / u-InP	Buffer Cladding	918	182

Table 5.2 Epitaxy structure and parameters of the upper cladding and InGaAs at the planar region. Epitaxy layers in ( ) indicates the undoped cladding structure.

After the etching of SAG masks, one portion of active and one portion of passive were put into the reactor for the p-doped upper cladding and p-InGaAs contact layer epitaxy growth. This was soon followed by the undoped cladding and InGaAs growing. And lastly, the active portion with undoped cladding was undergone another zinc diffusion process by using the same MOVPE equipment. The procedure and detailed condition is discussed in chapter 3.Then both passive portions was under through the passive waveguide processing while the active went through the device processing. Both procedures will be discussed in the following two sections.

5.2 Passive Waveguides Fabrication

The two passive portions we grown from MOVPE were simultaneously fabricate into passive waveguide. A portion of the undoped one was used to fabricate using dry etching. And it will also discuss as follow.

5.2.1 Chemical Wet Etching Based Process of Passive Waveguides

A) Using the grown InGaAs contact as mask, a layer of positive photoresist (TSMR 8900) is spun coated on top of it. The spin coating condition is 500rpm for 5 sec followed by 6000rpm for 60sec. The thickness formed by the spun phtoresist is approximately 1um. For better adhesive of the resist, primer was first spun coasted under the same condition prior to the photoresist. 90sec was waited in the idle of primer spinning and photoresist spinning. The resist coated substrate was then subjected to 90sec pre-baking at 110°C with a digital hot plate. Waveguide patterns are defined onto the resist using soft contact photolithography under mask aligner. Then the exposed resist is developed in NMD-3 solution for 30 to 60 sec. However the time used for developing varied due to different external factors such as temperature and humidity. The developed patterns needed to confirm under microscope after developing. This procedure was followed by a post-bake for 90sec at 110°C to strengthen the resist to the InGaAs mask.

B) Waveguide patterns are transfer from the resist to the lower layers using chemical etching. InGaAs was etched with H_2SO_4 + H_2O_2 + H_2O in 1:1:5 ratio or SH solution in short. On the other hand, InP was etched with HCl solution with 1:7 ratio (36% HCl and 20% HCl). The InP etching would stop once it reached the etch stop layer which can be confirmed by bare eyes.

C) The remained resist was removed with heated acetone and IPA.

D) The InGaAs contact layer of the waveguides was removed with the HS again. The extra step is to further reduce the propagation loss due to the absorption of light by highly p-doped InGaAs.

E) Usually at this stage, the samples thickness is approximately 350um. The

samples were then thinning up to 150um and ready to be cleaved.

5.2.2 Dry Etching Based Process of Passive Waveguides

A) First, the surface InGaAs was totally removed using SH solution since we didn't need to use it as mask like wet etching process does. Then a 320nm think of SiN film is deposited on the Upper Cladding InP with magnetron sputtering machine. The sputtering rate is 320nm for 60mins at room temperature.

B) The deposition of photoresist, photolithography procedure and exposing is done under same condition with wet etching based procedures. Refer to step A of 5.2.1.

C) The waveguide pattern is transferred from the resist to SiN mask by ICP dry etching with CHF3/Ar/O2/He plasma with gas flow of 9:1:0.3:8 sccm and source power of 100W and bias power 15W. The photoresist was removed using ICP O_2 plasma ashing before the InP material is etched, with O_2/Ar gas flow of 10:8 sccm and 200W source power, 0W bias power for 8 minutes. The SiN etching and O_2 plasma etching are both performed in room temperature.

D) The etching of the InP material was done in the same ICP etching machine with Cl_2/Ar plasma. The optimization of etching condition for low damage and vertical, smooth sidewall is not included in this study. We referenced the result obtained from Mr. Salah Ibrahim of our research group. [69]. At an elevated temperature of 210 ^oC, with the Cl_2/Ar gas ratio of 8:2 sccm was found to be satisfying. In this etching process, the substrate was bonded to the Si carrier wafer using the silver paste. The silver paste is used to facilitate heat conduction to the substrate surface and to avoid sample of small size from being blown away during the plasma ignition. Our dry etched undoped sample is also ridge waveguide. The comparison of such dry etched sample and wet etched sample is detailed in next chapter.

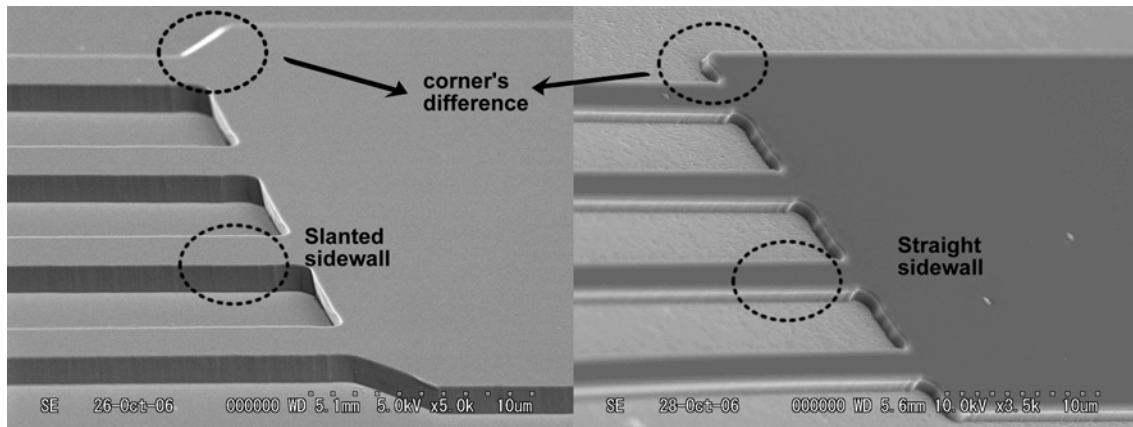E) The samples were thinning until 150um and ready to be cleaved

Fig. 5.3 SEM images of the passive MM coupler at the 4 input ports. (left) the wet etched sample, (right) the dry etched sample.

Depicted in Fig. 5.3 are the Scanning Electron Microscope (SEM) images of the fabricated passive MMI couplers. Both images showed the combing side of the 4X1 combiner. The left one is the wet etched sample while the right one is the dry etched one. The advantage of dry etching over wet-etching is apparent here. First the corner of the dry etched sample is much sharper than the wet etched one the corner of right angle is formed, which in short more closely resemble to the original design. Second, the side wall of the wet etching is slanted toward the base which is quite common in chemical wet etching process. Thus, though the design of waveguides was 2.5um, in the end the base of the waveguide can reach 4um or more, that's the reason why we try to lessen the thickness of the upper cladding during our MOVPE growth. And in addition, if the thickness of the upper cladding is not uniform among all channels, the difference between each waveguide could be even enhanced. However, during the design phase of this research, wet etching was decided and the design of the passive components has been determined, so though there are advantages with using dry etching, in this study the result of dry etching is for reference purpose. Another problem with dry etching is that the etching rate is quite unrepeatable and thus very difficult to control even using a dummy beforehand. This is also another reason that we chose wet-etching over dry etching because of the stable etching rate and avoiding of contamination due to ICP dry etching..

5.3 Active Laser Diode Arrays Fabrication

The two active portions we grown from MOVPE, one zinc doped sample,

and one zinc diffused sample were simultaneously fabricate into active LD arrays. The procedure is detailed as below.

A) Waveguides need to be patterned first, and similar to the process of wet etching of passive waveguides mentioned in section 5.2.1. We used the InGaAs layer as mask, disposition of photoresist, photolithography, then developing. The condition used is same with the one mentioned in A) of section 5.2.1. This mask however has straight waveguide patterns passing through the grown SAG region with length of 2.5um. The waveguides need to be alight in the middle of the grown SAG region carefully. The gap of the SAG region is 15um wide.

B) The waveguide patterns were transferred thru wet-etching, InGaAs etching using SH solution and InP with HCL solution.

C) After the waveguides were formed, a 320nm of SiO_2 is sputtering on the surface of the whole sample. This layer defines the regions for current injection and it also isolates the optical field from the metalization layer in order to avoid high optical loss. This is a step need to be done prior to contact opening.

D) The contact opening on top of the ridges, were defined as openings using positive photoresist (TSMR 8900). This step is one of the most difficult procedures during the whole processing since misalignment in the opening will cause current leakage. The SiO_2 exposed by the openings was etching away in ICP etching machine with $CHF_3/Ar/O_2$ plasma in ratio of 9:1:0.3:8 sccm for 10 minutes. The remaining of resist is etching away using O_2 plasma.

E) After the dry-etching procedure, the etched sample was put into a diluted SH solution, with the ratio is 1:1:40 (H_2SO_4 + H_2O_2 + H_2O) for around 5 sec. the purpose of this extra step to etch away a very tiny portion of the surface InGaAs contact layer which might be contaminated by plasma from dry-etching.

F) The p-metalization was deposited on the InGaAs contact layer with an EB evaporation machine. This p-metalization consists of Au over Ti layers. The

Ti of 100nm meter was first deposited on the whole surface of sample followed by 500nm of Au. Ti is used as transitional p-contact to achieve an ohmic contact behavior at the interface with highly p-doped InGaAs layer. While the Au completes the electrode contact and it was used because of its good electric conductivity. After the deposition of p-metalization, the pattern of the p-contacts on the surface of the sample was defined in positive photoresist (TSMR 8900) and unwanted metal was etched away with proper etchant. Au was etched away with KI + I_2 +H_2O in 2 grams to 1 gram to 50mL ratio while Ti was etched away with BHF.

G) The samples were further thinning up to 120um. Followed by the metalization of Au at the bottom side using plasma quick coating.

H) Annealing of the sample was done at 384°C for 30 sec. The samples were ready for cleaving.
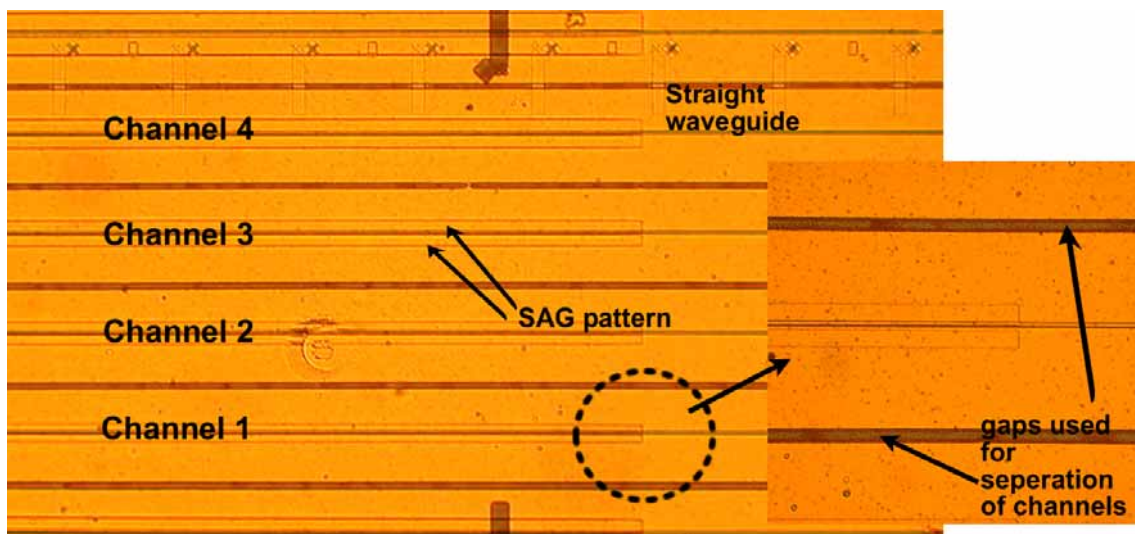
Fig. 5.4 Microscopic view of the fabricated LD array with 4 channels. Before measurement LD array would be cleave into shorter length for testing

Depicted in Fig 5.4 is the fabricated LD array with channel 1 to 4 on top of it. Both zinc doped and zinc diffused samples looked quite the same and the gap between each channels was formed by etching away the unwanted Au and Ti. This helps prevent current leaking during forward bias. LD arrays were cleaved into shorter cavity for testing. The result of output performance is detailed in next chapter. Figure 5.5 illustrates the SEM images of two samples of the cross section of both zinc doped LD (left) and zinc diffused LD (right). The

enlarged images at the upper left corner and lower right corner of the same figure shows the core section with 5 quantum wells sandwiched by upper and lower SCH. It should be noted that in the left figure, the ridge waveguide is sandwiched between the etched SAG regions. And the remains from the SAG patterns which were etched away after the growing of the core look visible in the same figure.
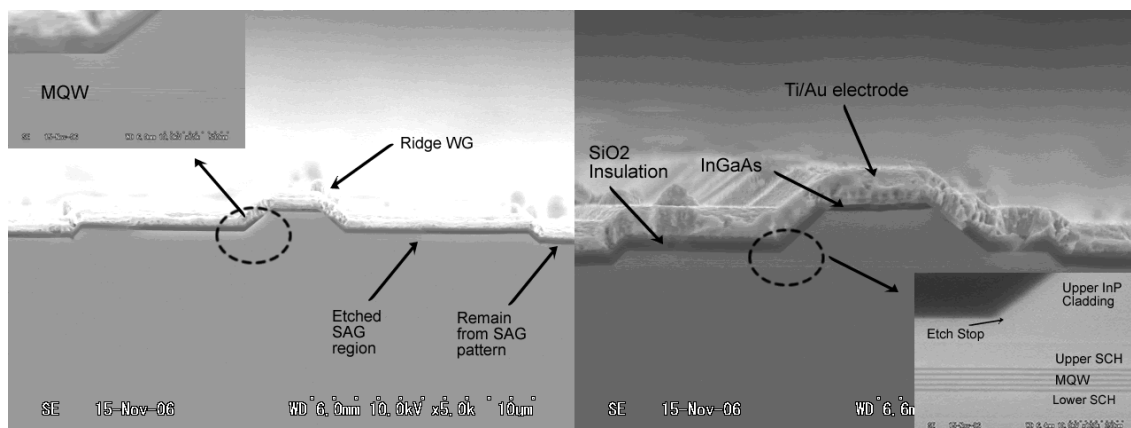

Fig. 5.5 SEM images of the cross section view of two laser diode. (left) zinc doped sample, (right) zinc diffused sample. The upper left and lower right smaller images are the enlarged section showing the core portion. 5 wells are clearly shown in the both images.

5.4 Conclusion

In this chapter the general fabrication procedures have been described. It can be mainly separated into the two parts: the passive parts and the active parts. For the passive parts, mainly the doped and undoped passive waveguides were made for optical loss measurement. On the other hand, in the active parts, zinc doped and zinc diffused Fabry-Perot Laser Diode arrays were fabricated for performance comparison.

First, since the epitaxy structure for both passive and active are quite similar, the procedure was stated in the first part of this chapter. One thing worth mentioning is that differ from the conventional single-step-epitaxy growth which is commonly used in Selective Area Growth (SAG), in this study a two-step-epitaxy growth was used: core is grown first, followed by etching of SiO$_2$ mask, and then the growth of upper cladding and InGaAs contact layer. The main reason of doing this is to apply the zinc diffusion among all the 4 channels of the active device. The structure of both core part and upper

cladding/InGaAs part is illustrated in table forms.

The fabrication procedures were then detailed in the succeeding section, first the passive fabrication procedure then the active fabrication procedure. In the passive fabrication procedure part, in addition to the wet-etching of doped and undoped passive waveguides, dry-etching was also used for reference purpose. SEMS images of etched multimode interference (MMI) couplers were also used to illustrate the difference between wet and dry etching.

6. Characterization of Passive and Active components

As mentioned in last section of chapters, the design consideration of the Monolithically Integrated 4-Channel DFB Laser Array with Optical Combiner for 1.55µm CWDM Systems by Selective Area MOVPE and the fabrication of separated passive and active components have been detailed. In this chapter, the characterization of both components will be detailed in the succeeding sections.

6.1 Passive Components

Passive components employed in the designed integrated device include straight passive waveguides, S-bend passive waveguides and 4X1 multimode interference (MMI) coupler. A passive component such as a MMI coupler is considered to be ideal if it could act transparently to the incoming light and thus play an important role of combining the incoming light. However the reality is far from transparent. This might due to some different reasons: such as, total insertion loss due to coupling loss between the optical fibers and the facets of the cleaved device, unwanted impurities and defects contaminated the surface of device during processing and thus contribute to the propagation loss, the sidewall roughness of the waveguides contribute to scattering, and lastly which the we would like to focus on in this thesis, to diminish the loss due to p-doped InP cladding in the passive part which unavoidably form during selective area growth.

Although the propagation loss in silica optical fiber has been ideally optimized to as small as 0.2db/km, however waveguides based on semiconductor materials is far from getting near such result. Thus, we believe it is very important to confirm the propagation loss of light in the passive waveguides which is used through out the study. In the succeeding section, loss measurement of straight waveguides, and some qualitative output we observed from the fabricated S-bend passive waveguide and 4X1 MMI coupler will be detailed.

6.1.1 Propagation Loss Measurement by Fabry-Perot Method

Fabry-Perot Etalon Method is one of the most reliable ways to estimate the loss of a waveguide whose reflection ratio on both facets is known. [50-51] As shown in Fig 6.1. with reflector ratio r_1 and r_2 at its two facets, the waveguides forms a Fabry-Perot etalon. When the light E_{in} couples into the waveguide, the power of the output light varies with the wavelength according to loop phase matching condition as shown in equation 6.1.
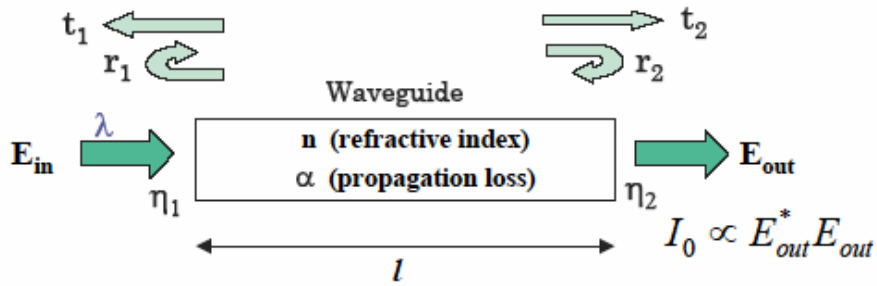

Fig.6.1 Schematic experimental setup for measuring waveguide propagation loss with Fabry-Perot method..

Optical loss in passive waveguides can be derived to equation 6.3 from 6.1 with contrast H which is defined in equation 6.2. In the three equations t_1, t_2 represents the transmission ratio, r_1, r_2 are the reflection ratio, η_1 η_2 are the coupling efficnecy, E_{in} and E_{out} denote the input and output of electromagnetic field of the lightwave, λ is the wavelength I is the length of the waveguide and finally I_0 is the output intensity.

$$I_0 \propto E_{out}^* E_{out} = \frac{\eta_1 \eta_2 t_1^2 t_2^2 e^{-\alpha} |E_{in}|^2}{1 + r_1^2 r_2^2 e^{-2\alpha l} - 2 r_1 r_2 e^{-\alpha l} \cos(4\pi n l / \lambda)} \qquad (6.1)$$

$$H = \frac{I_{0max}}{I_{0min}} = \left(\frac{1 + r_1 r_2 e^{-\alpha l}}{1 - r_1 r_2 e^{-\alpha l}} \right)^2 \qquad (6.2)$$

$$\alpha = -\frac{1}{l} \ln \left(\frac{1}{r_1 r_2} \frac{\sqrt{H} - 1}{\sqrt{H} + 1} \right) \qquad (6.3)$$

As described in the previous chapter, we have mainly fabricated two sets of passive waveguides, mainly the chemically wet-etched undoped passive

waveguides and wet-etched doped passive waveguides. As it has been mentioned in chapter two, the main issue with the SAG technique has been detailed, which is that the upper cladding of the passive region is unavoidably p-doped during the single step epitaxy growth, thus in such case, Selective Zinc diffusion is proposed to solve such particular issue. And if it worked out the way we think, the passive components of the selective zinc diffused integrated device is expected to be undoped.

6.1.2 Loss Measurement Setup for Passive Waveguides

The measurement setup of the passive waveguides using Fabry-Perot method is illustrated in Fig. 6.2. The input laser is first carefully coupled to the facet of the tested sample (both doped and undoped passive waveguides) via a single mode optical fiber (SMF), and powered powered by a tunable laser diode (TLD). Three wavelengths were tested, 1530nm, 1550nm and 1570nm. The polarizer controller (PC) which connected between the TLD and the SMF of the input laser is used to switch from TE mode to TM mode and vise versa. The optical output from the facet of the passive waveguide was then refocused thru a lens, and projected on a CCD camera. The pin hole is used to screen out unnecessary light entering either CCD camera or photodiode. After the output light spot was refocused properly, the camera was replaced by a photo-detector connected to a power meter, and then data was gathered thru the power meter that was connected to a pc. The data gathered is detailed in the next subsection.
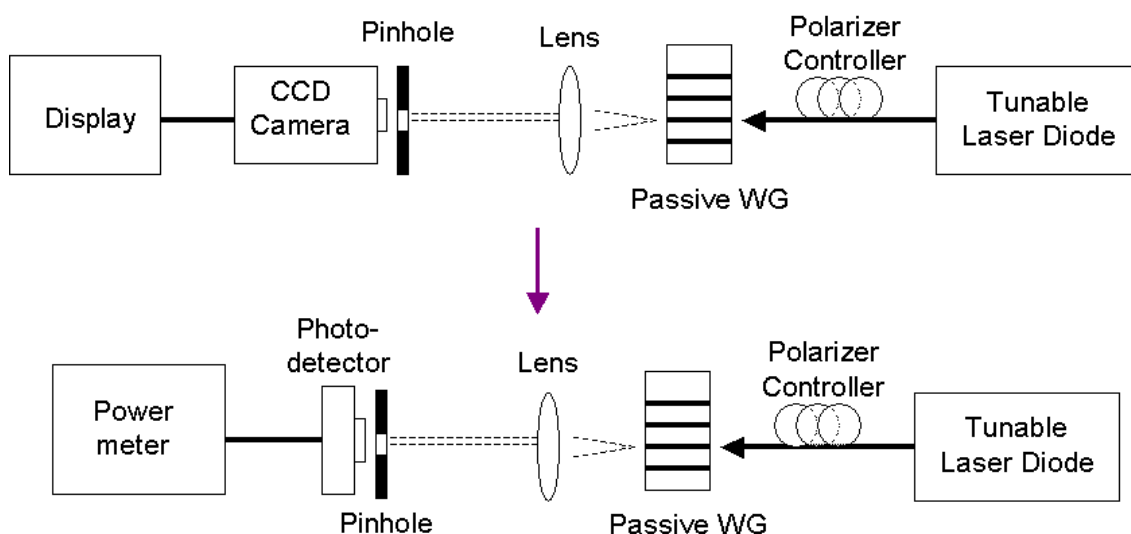

Fig.6.2 Experimental set-up of measurement for the passive waveguide.

6.1.3 Fabry-Perot Method Loss Measurement Result

Examples of measured data for both wet-etched doped and undoped waveguieds at TE mode is illustrated in Fig. 6.3. (Left is the undoped sample while Right is the doped one). The illustrated undoped waveguide is 1550µm long while doped wavelguide is 1480µm long. 1530nm, 1550nm and 1570nm were chosen as the three wavelengths to be measured for the loss using Fabry-Perot method. 1590nm is also a expected to test as well, however due to the limitation of our equipment, only the mentioned three wavelengths were used, These wavelengths were chosen, because it's in agreement with the four channels we designed for 1.55µm CWDM system. While assuming r_1 r_2= 0.3 and the peak-to-valley ratio H, which obtained in Fig.6.2, the loss is calculated with equation 4.3 and the calculated graph is presented in Fig. 6.3. Take Note that the results have been converted from cm^{-1} to dB/cm. 9 to 15db/cm loss (and 13 to 15dB/cm loss) is observed in the fabricated undoped passive waveguide at TE mode (TM mode), while 22 to 28dB/cm loss (and 23 to 31db/cm loss)is observed in the doped one at TE mode (TM mode). TE mode result is slightly better than TM mode result which is expected. It is observed that the loss in the doped waveguide is not as severed as it was observed in the previous study. This might due to the passive waveguide fabricated before is a deeply etched waveguide, not like the ridge waveguide being studied here.
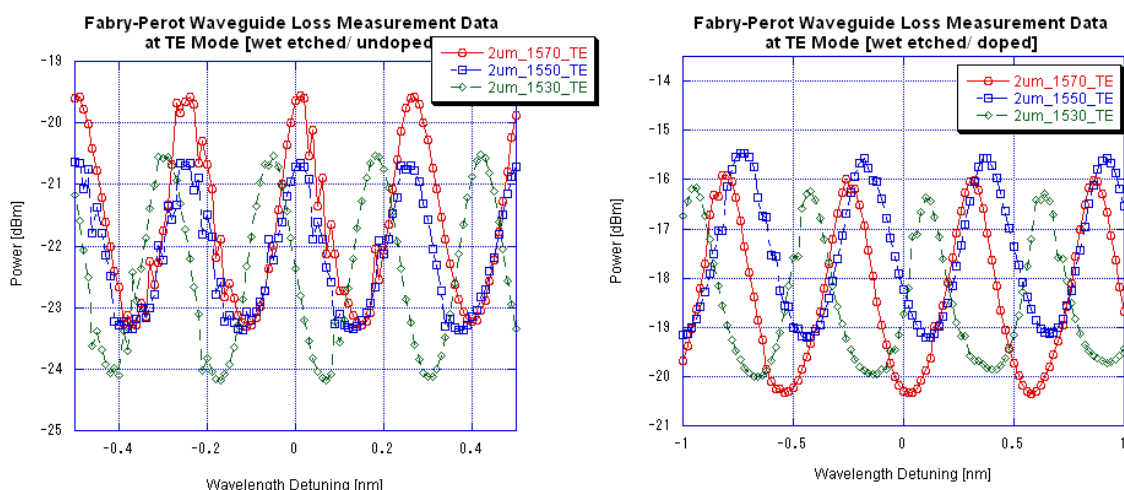

Fig.6.3 Sample of the propagation loss measurement data from Fabry-Perot Method. (Left) figure was measured from the wet-etched undoped waveguide in TE mode, while (Right) was measured from wet-etched doped waveguide in TE mode.
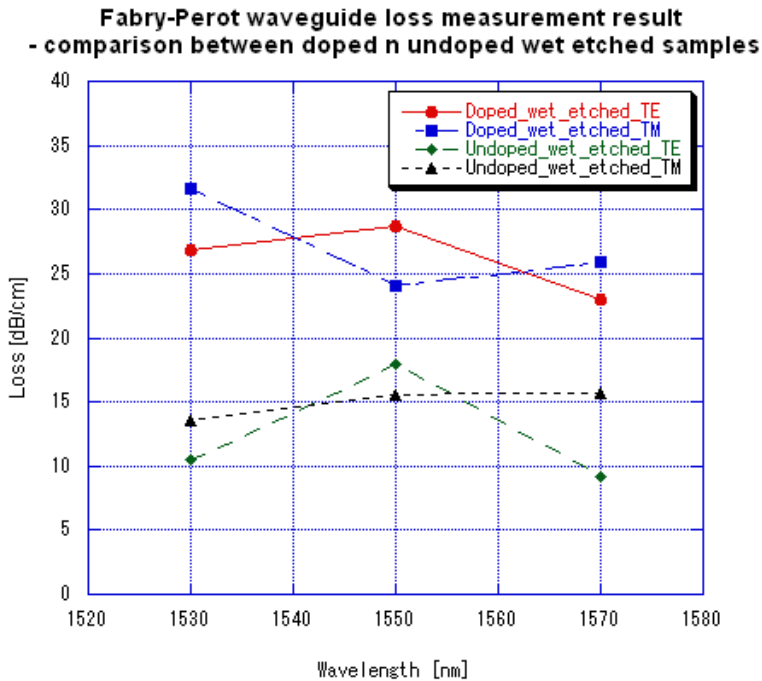
Fig.6.4 Fabry-Perot waveguide loss measurement result for both wet etched doped wavguide and wet edched undoped waveguide.

As mentioned in the previous section, another set of undoped waveguides has fabricated using dry-etching. Since the sample used here for dry-etching is belong to the same batch of the undoped sample used in wet etching, crystal quality and structure is assumed exactly the same. The waveguide is cleaved to 1500µm. The results showed 9 to 15dB/com loss in TE Mode and 9 to 17dB/cm in TM mode. The result was not very far from the result obtained thru wet etching. The reasons behind might due to first, both waveguides are shallowly edged waveguides, therefore both optical fields are confined under similar ridge profiles, and thus the results didn't differ too much. Secondly, since the dry-etched waveguide is a shallowly etched, the contamination by ion is only limited to the upper InP cladding, thus, core layer is still well protected, and loss due to contamination is lessen. And thirdly, the additional chemical wet etching using diluted SH soon after dry etching, helped etched the surface which might contaminate by the plasma from the dry-etching.
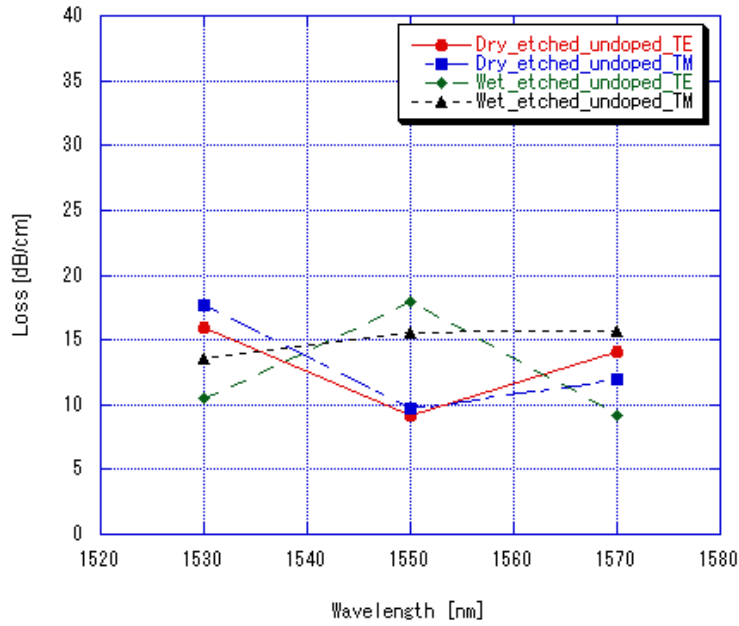
Fig.6.5 Fabry-Perot waveguide loss measurement result for both wet etched doped wavguide and wet edched undoped waveguide.

6.1.4 Multimode Interference (MMI) Coupler

Depicted in Fig. 6.6 is the microscopic image of fabricated MMI couplers. Five different length of MMI combiners were fabricated with straight waveguides sandwiched at middle of each set of MMI couplers. Though they are made into combiner, but we used the straight output waveguide as input instead, and 4 inputs as outputs. Images of each output were captured using CCD camera and some of them are illustrated in Fig. 6.7. The qualitative data was captured with the aid of a Hamamatsu DV3000 digital image processor. The input light's intensity was set to 0dB. Based on the images, we can see the 560μm MMI coupler performed best, which the four spots optical output seem to be equally split similar to a 6dB coupler. Based on our BPM simulation result, the tolerance of the designed MMI combiner is 530 ± 29μm, in this case, b) and c) fall within the tolerance and perform not too badly. In Fig. 6.8, the L560 MMI coupler is the same one in Fig. 6.7, except that the input light's intensity was set to -15dB, and the left image is the output images taken from the output facet of the straight waveguide adjacent to the 560MMI coupler. Based on the image, the outputs of the MMI coupler are not exactly 1/4 of the output of the adjacent straight waveguide. Estimation was conducted by comparing the optical power

transmission with the straight waveguide. The optical output of the straight waveguide was measured with 25.35dB, while the adjacent MMI coupler's output were measured with 33.34dB, 32.75dB, 31.96dB and 33.2dB (average of 32.81dB). Considering the 6dB theoretical loss in each port, the average excess loss of the 6dB MMI coupler was calculated as about 1.46dB.
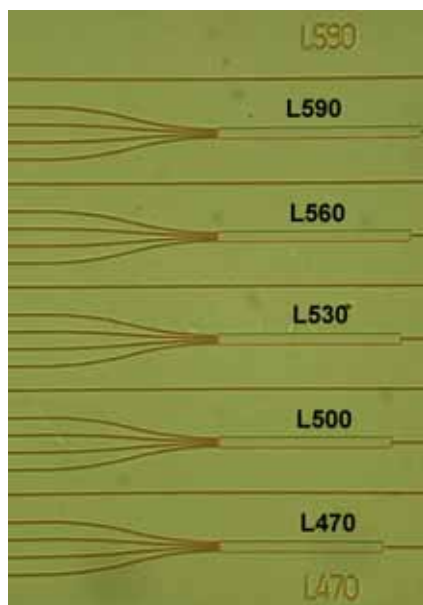

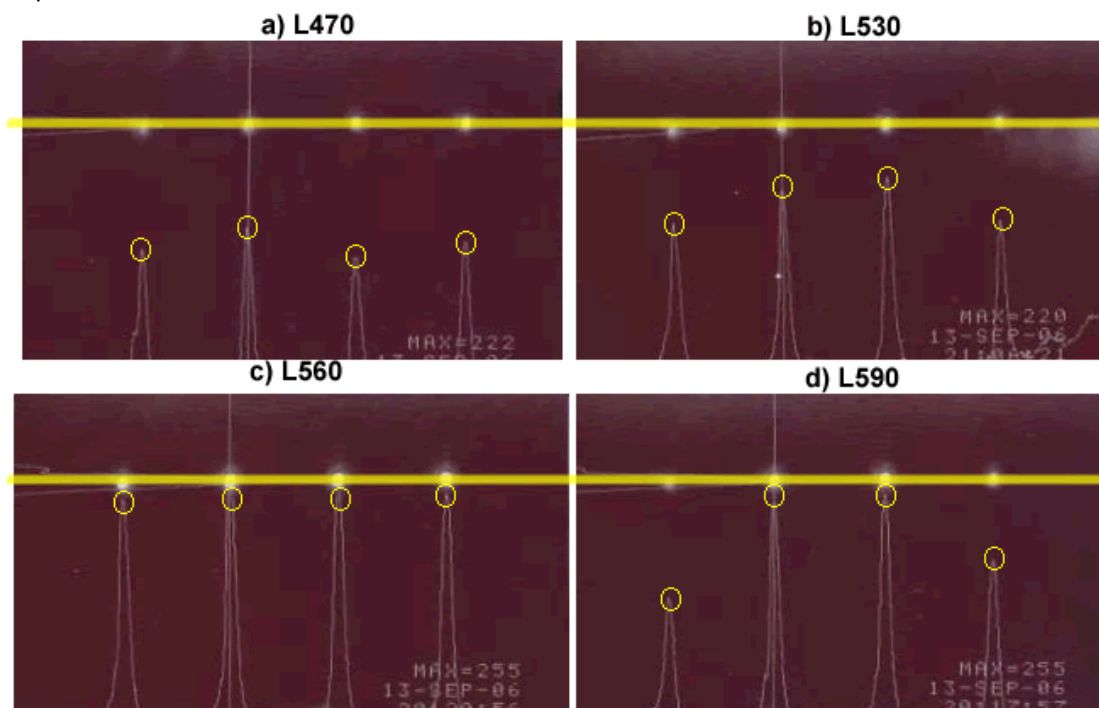*Fig.6.6 Microscopic image of the fabricated MMI couplers with different length: from 590µm to 470µm.*

Fig.6.7 Images captures from the output faucet of the passive waveguides thru a MMI coupler. a)

470µm MMI coupler, b) 530µm MMI coupler and c) 560µm MMI coupler, and d) 590µm MMI coupler. The input light's intensity is set to 0dB.
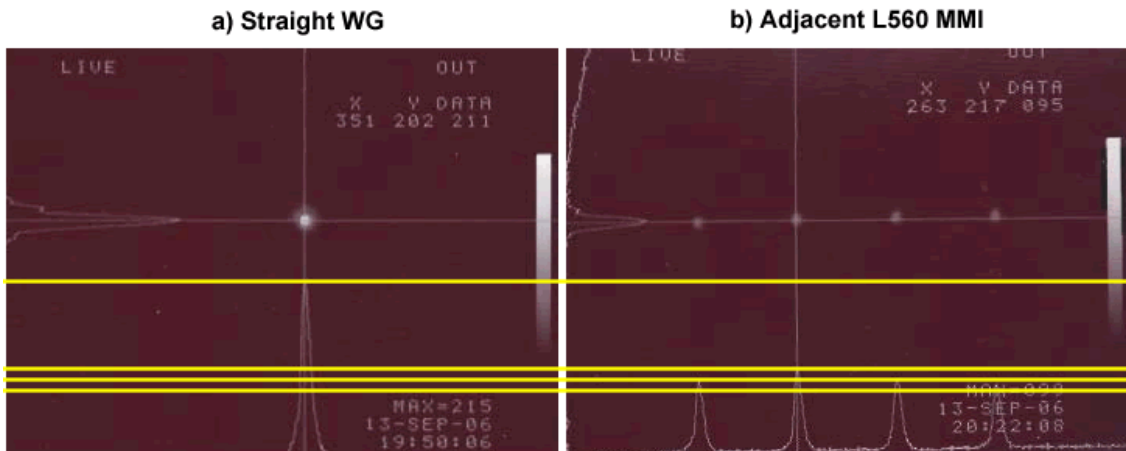

Fig.6.8 Comparison of a) straight waveguide and b) adjacent 560µm MMI coupler.The input light's intensity is set to -15dB.

6.1.5 S-bend Passive Waveguides

Fig. 6.9 illustrated the microscopic image of our undoped S-bend passive waveguides As it can be noted that the two S-bend waveguides at the upper portion of the same figure denoted R2757, those are the S-bend passive waveguides with radius of curvature of 2757µm; as same case, the lower one denoted R1000 are S-bend waveguides with radius of curvature of 1000µm radius. The straight waveguides of 2.5µm width, which sandwiched between the two sets of s-bend waveguides, are straight waveguide used to compare with the optical output of the s-bend passive waveguides. These outputs are illustrated in Fig. 6.10. These pictures were captured from the output facet of the passive waveguides thru an CCD camera, and the input light's intensity was set to be -15dB. The three images illustrated the output of three different waveguides of Fig 6.10: a) the output of the straight waveguide at the center, b) R2757, the S-bend waveguide with radius of curvature of 2757µm, and c) R1000, the S-bend waveguide of radius of curvature of 1000µm. As it is mentioned in chapter 4, section 4.4, that due to the limitation of BPM simulation tool, the precise optical loss occurred in a S-bend waveguide is undeterminable. However, the nature of the passive waveguides can be confirmed, the smaller the radius of curvature of a passive waveguide, the larger loss. Based on the images in Fig. 6.10, the output image shows that the optical power of a straight waveguide and the R2757 waveguide don't differ much, however, the R1000

waveguide's optical power is lowered than the other two. Similar to the MMI coupler characterization mentioned above, estimation of the two types of S-bend waveguides was conducted by comparing the optical output with the straight waveguide which illustrated in Fig.6.9. The optical output of the straight waveguide was measured of 20.5dB, while 21.16dB optical power was measured in R2757 S-bend waveguide and 22.36dB in R1000 S-bend waveguide. The excess loss was estimated to be 0.66dB in R2727 S-bend waveguide and 1.86dB in R1000 S-bend waveguide.
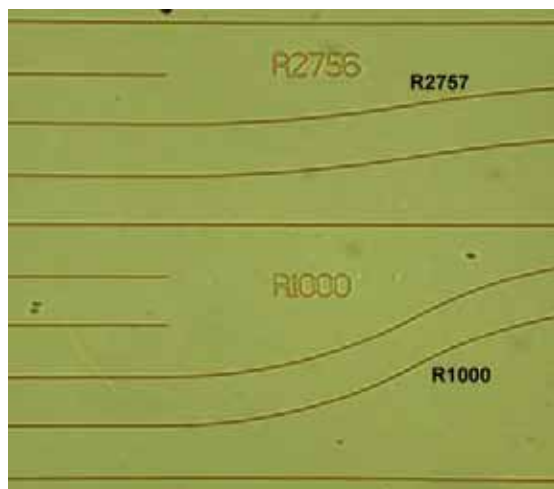
Fig.6.9 Microscopic image of the S-bend passive waveguide: (upper portion) S-bend passive waveguides with radius of 2757µm, (lower portion) S-bend passive waveguides with radius of 1000µm. The straight waveguide in the centre is used to compare the output from the S-bend waveguides.
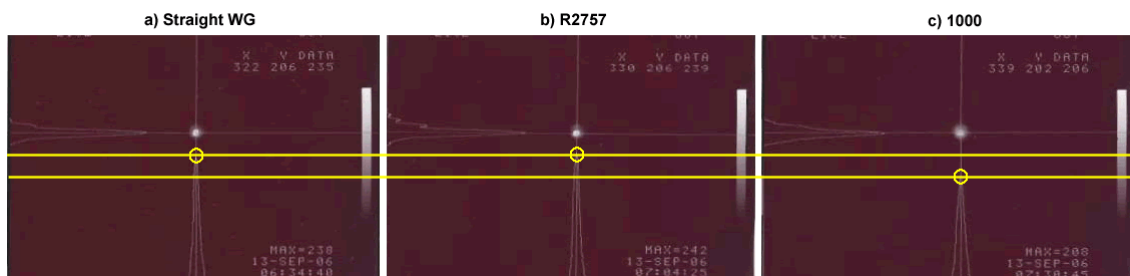
Fig.6.10 images captures from the output faucet of the passive waveguides illustrated in Fig. 6.9. a) output of the straight waveguide at the centre, b) R2757, the S-bend waveguide with radius of 2757µm, and c) R1000, the S-bend waveguide of radius of 1000µm.

6.2 Active Components

Active components that has been fabricated and tested for characterization are discussed in this section. There are mainly the two sets of Selective Area Grown Fabry-Perot Laser diode (SAG FP LD) arrays that were fabricated: the FP LD array which is grown conventionally, or *zinc doped* FP LD array, and the selective zinc diffused one, or in short the *zinc diffused* LD arrays. The measurement setup is described in section 6.2.1. And the characteristics of both LD arrays are illustrated and compared in section 6.2.2. The other parameters such as material gain, the refractive-index change, the alpha-factor of the mentioned devices are also illustrated in the later part of this section.

6.2.1 Measurement Setup for the Laser Diode Arrays

Among all characterization of laser diode, the current-voltage (I-V) curves, current-power (I-L) curves, and spectra measurements are the most fundamental one. Depicted in Fig 6.11 is the experimental setup for measuring the I-L curves and spectra measurement. The laser diode arrays (both Zinc doped and Zinc diffused ones) were first cleaved into designated length, then mounted on a well-polished bronze plate as heatsink using conductive paste, following by heating on hotplate at 150 degree Celsius for 10 minutes to dry up the conductive paste. The heatsink serves as a simple chip carrier and its high heat conductivity allows a stable control of chip temperature. The optical fiber which is alight to the facet of the LD one channel at a time is mounted on a fiber holder. And this fiber hold is fixed on a separate 3 dimensional (x-y-z) micro-positioner. This help in optimizing the alignment between optical fiber and the LD array, thus giving the maximum output which can be detected by the power meter and the spectrum analyzer. The device under test was placed on sample holder and carefully temperature controller. This setup can maintain at stable chip temperatures in the range of 10°C to 30°C depending on the ambient temperature and humidity. The LD arrays are biased through gold plated needles positioned on the p-contact electrode. The n-contact is grounded via the bronze plate chip carrier. The mechanical setup has the flexibility to be used for altering new device structure with any sample width. The tip of the single mode tapered fibers (SMF) has a radius of approximately 10µm and a taper angle of nearly 90 degrees. The taper fiber holder arms have vacuum chucks to fix the

position of the fiber so that a reliable coupling can be maintained over a period long enough throughout the measurement, though this is not absolute due to different external reasons. The optical power and spectrum which generated by the LD array is then measured with an optical power meter and spectrum analyzer. This measurement setup has been used for analyzing the most of the basic characterization of both LD arrays.
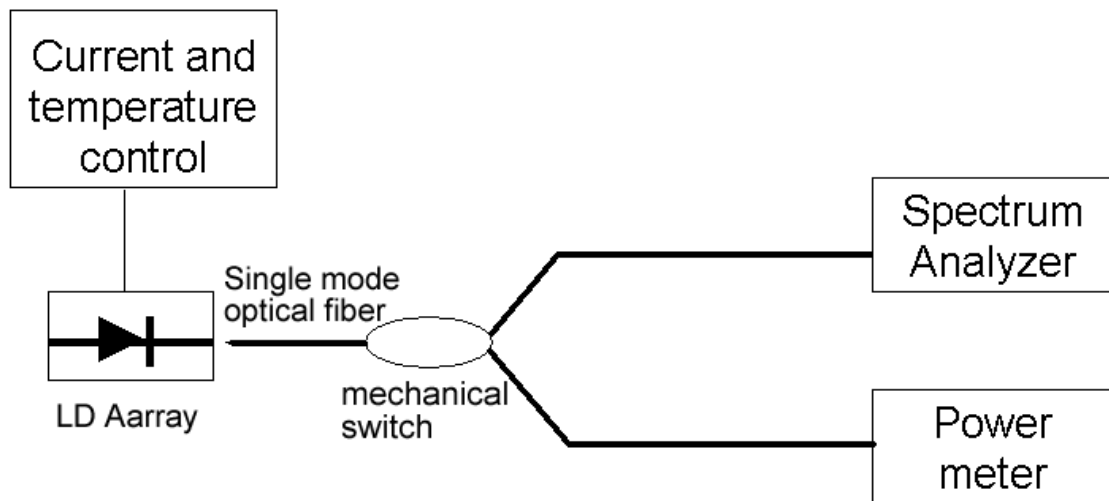
Fig.6.11 Experimental set-up of measurement for the laser diode arrays.

6.2.2 Current-Voltage and Current-Power Characteristic of Laser Diode Arrays

Fig 6.12 illustrates the current-voltage (I-V9 characteristics of 2 laser diodes: one from each of the zinc doped and zinc diffused LD arrays respectively, and stabilized at 15°C using temperature controller. This is usually one of our first step of determine whether the device can perform accordingly. The current flowing through a LD can be modeled thru:

$$I = I_S \left[e^{\beta(V - IR_s)} - 1 \right] \qquad (6.4)$$

$$\beta = \frac{e}{\alpha k_B T} \qquad (6.5)$$

where V, I, RS, I_S, and α represent the voltage, current, series resistance, diffusion current and junction constant. As the forward bias is applied on a LD, it operates in LED-mode before lasing. And as current gradually increases up till threshold current, the differential resistance becomes constant due to the pinning of the quasi-Fermi level since the carrier distribution in the conduction

and valence bands are fixed after lasing. The quasi-Fermi level pinning results in the saturation of junction voltage even under further increase in the forward current, consequently the differential voltage becomes equal to differential resistance. [52-54] A turn on voltage of 0.7V usually represent a good ohmic contact in a LD. However in the mentioned figure, apparently both LDs turn on slightly more than 0.7V.
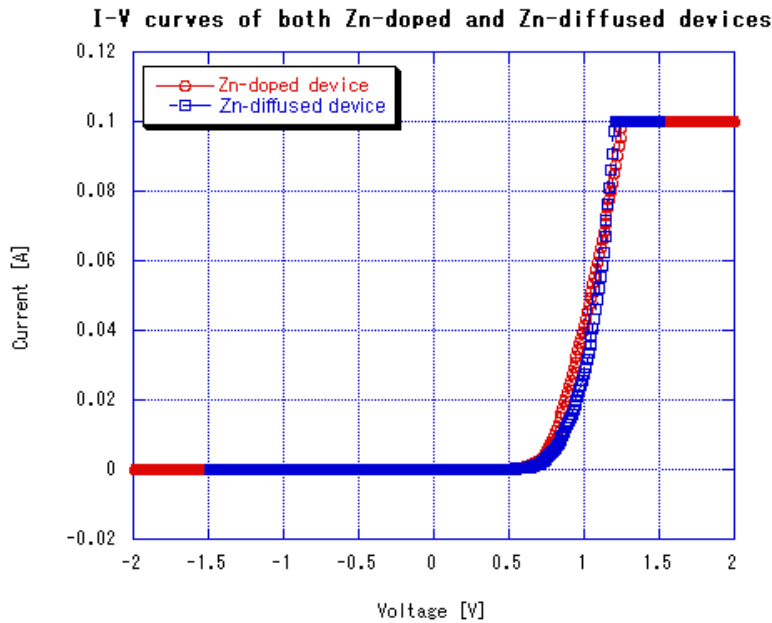
Fig.6.12 The I-V Characteristics of a zinc doped sample (red) and zinc diffused sample (blue)

Depicted in Fig 6.13 is the current-power (I-L) characteristics measured from samples of   a zinc doped LD array (sample#4800-1002) (left) and a zinc diffused LD array (sample#4890-1213) (right) at 15 degree Celsius. Sample#4800-1002 is 288µm long while, sample#4890-1213 is 450µm long. The left image of the mentioned figure illustrates the threshold current (I_{th}) measured from channel 1 to 4 of sample#4800-1002 with 31.18mA, 26.04mA, 24.03mA and 29.02mA respectively. On the other hand, the right figure shows the result of 27.92mA, 36.84mA, 33.33mA and 54.5mA I_{th} from channel 1 to 4 of the Zn diffused sample (#4890-1213). As the data showed that, the Zinc diffused samples has larger threshold current compare to the Zinc doped sample. This maybe due to a few different reasons such as one) the device length is longer than the Zinc doped sample, thus required higher threshold current to get lased. Another reason behind might due to zinc diffusion profile might need to further optimize in order to get the best results. Lastly, the results might vary due to

imperfect processing, due as epitaxy growth or processing itself.

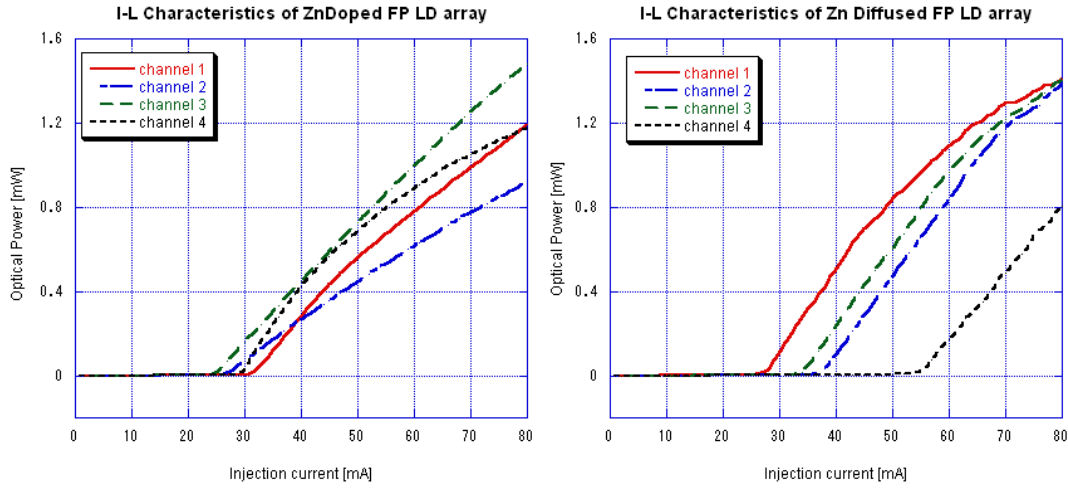Fig.6.13 I-L characteristics of wet chemically etched samples of Zinc doped (left) and Zinc diffused (Right) laser diode samples.
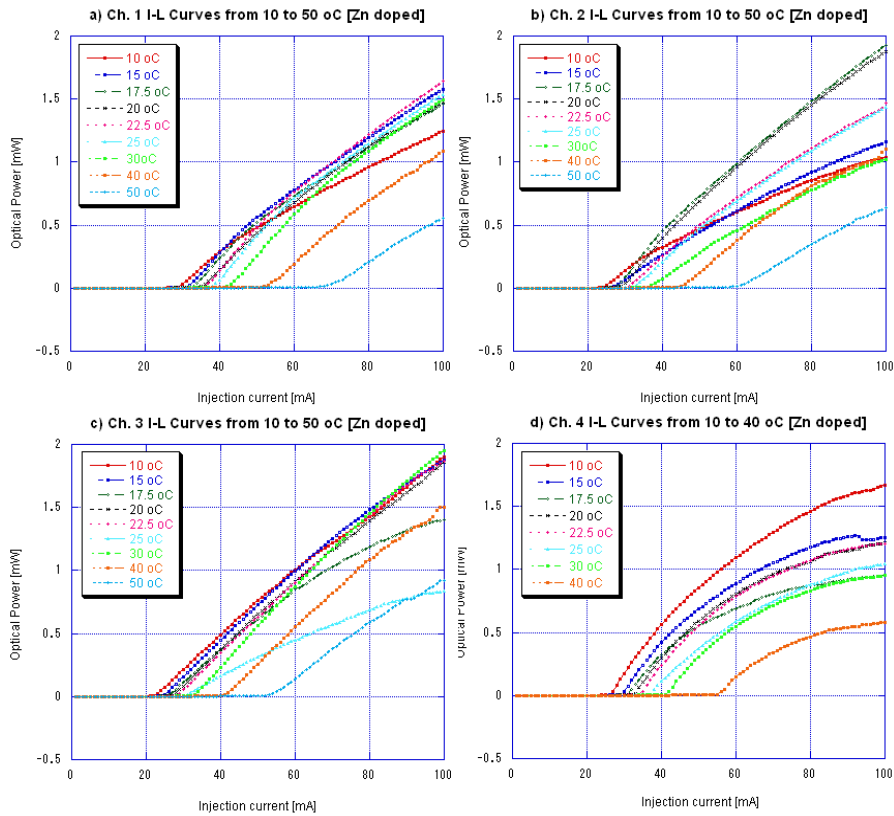
Fig.6.14 I-L Temperature Characteristics of the Zn doped LD array measured from $10^{o}C$ to $50^{o}C$
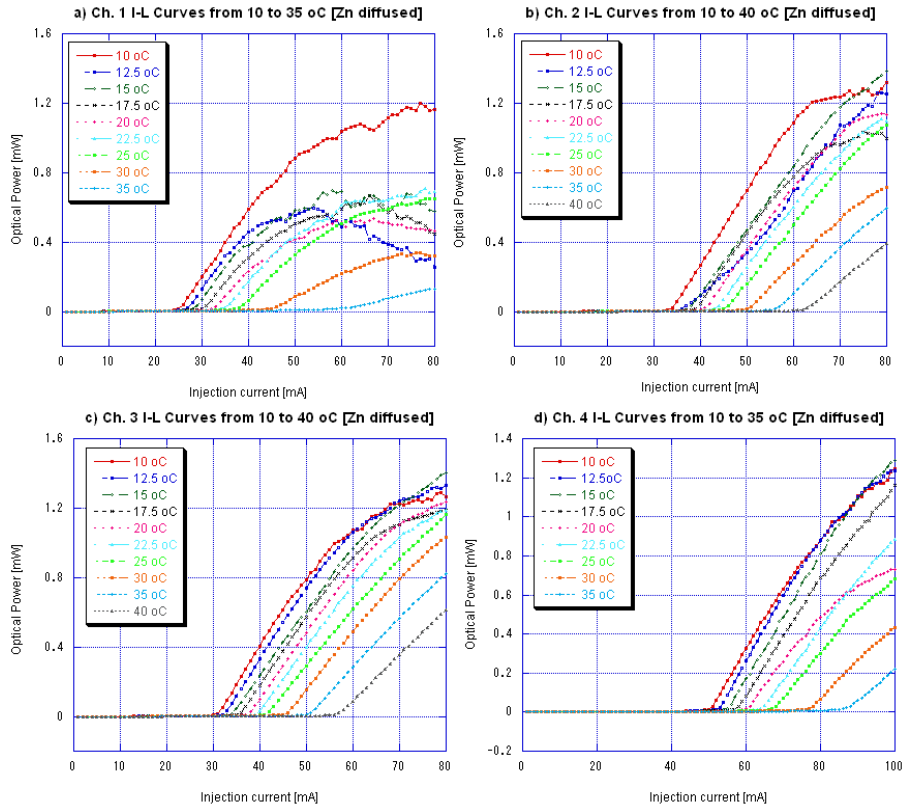
Fig.6.15 I-L Temperature Characteristics of the Zn diffused LD array measured from 10°C to 40°C

The I-L curves in Fig 6.14 and Fig 6.15 were taken from sample#4800-1002 (zinc doped LD array) and sample #4890-1213 (zinc diffused LD array) respectively. In both figures, graphs locate from upper-left corner (a) to lower-right corner (d) is the order of channel 1 to 4. These I-L curves were measured starting from 10°C and gradually increased the temperature up till 50°C for the former one and until 40°C for the latter one. While at each increment of temperature, temperature stabilization has been carried out first prior to the testing. As the data shows in mentioned figures, the threshold current (I_{th}) is increasing as the temperature increase. This tendency can be expressed with follow equation:

$$I_{th}(T) = I_0 \exp\left(\frac{T}{T_0}\right) \qquad (6.6)$$

T_0, of equation 6.6, is commonly used as an indicator for evaluating quality of good laser diode based on temperature dependency. As good laser diodes should lase accordingly even at high temperature. Typical values for 1.55µm InGaAsP lasers are found to be somewhere between 45K and 65K at

20°C to 80°C. And the result of such is illustrated in Fig. 6.16. The figure shows the T_0 of sample#4800-1002 are found to be 45.81K, 41.75K, 45.55K and 40.05K from channel 1 to 4 respectively, while the T_0 of sample#4890-1213 are 32.28K, 46.21K, 45.58K and 45.22K from channel 1 to 4 respectively. Optimization of the InGaAsP/InP structure layer might help improve the temperature dependency performance.
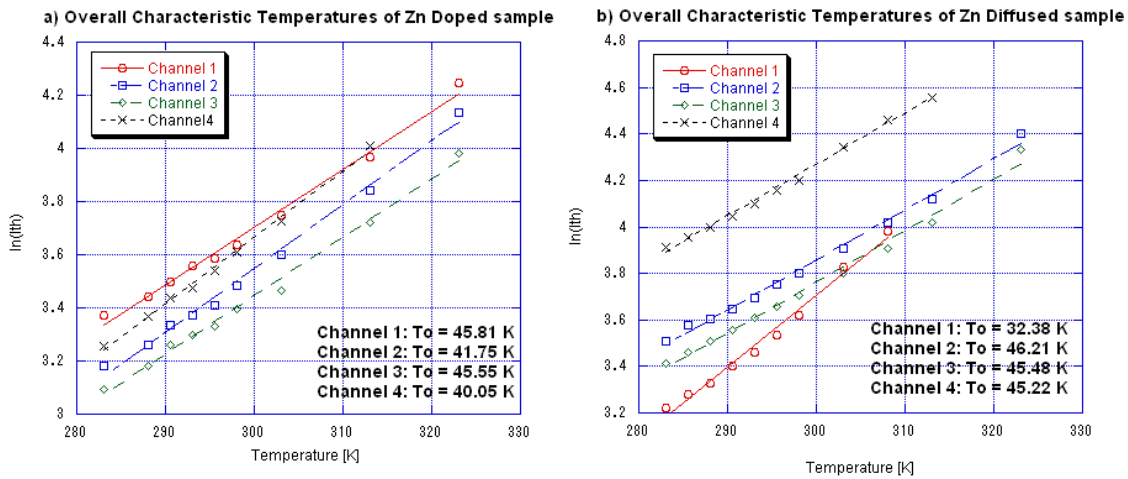
Fig.6.16 Characteristic Temperature Plots of a) Zinc doped sample and b) Zinc diffused sample.

6.2.3 Lasing Spectra of Fabry-Perot (FP) Laser Diode Arrays

The lasing spectra of sample#4800-1002 (zinc doped) and sample#4890-1213 (zinc diffused) are illustrated in Fig 6.17 and Fig 6.18. Graphs a) to d) represents from channel 1 to 4 respectively. The peak wavelength is measured 10mA above threshold and the result is listed as follow. The four channels of sample#4800-1002 are lasing at 1532nm, 1552nm, 1573nm and 1595nm for channel 1 to 4 respectively, meanwhile. The four channels of lasing are 1531nm, 1546nm, 1570nm and 1593nm for channel 1 to 4 respectively. It should be noted that as soon as forward bias is applied to the LD, as inject-current increase, the optical gain will also increase until around threshold current, then the optical gain will be clamped staidly. Meanwhile, the phase shift will first tend to blue shift along the increasing of inject current and optical gain until threshold current then start to red shift due to purely thermal effect. From the lasing spectra obtained in this subsection, parameters such as material gain, refractive index can be further extracted and analysed. And this data will be used in the succeeding subsections.
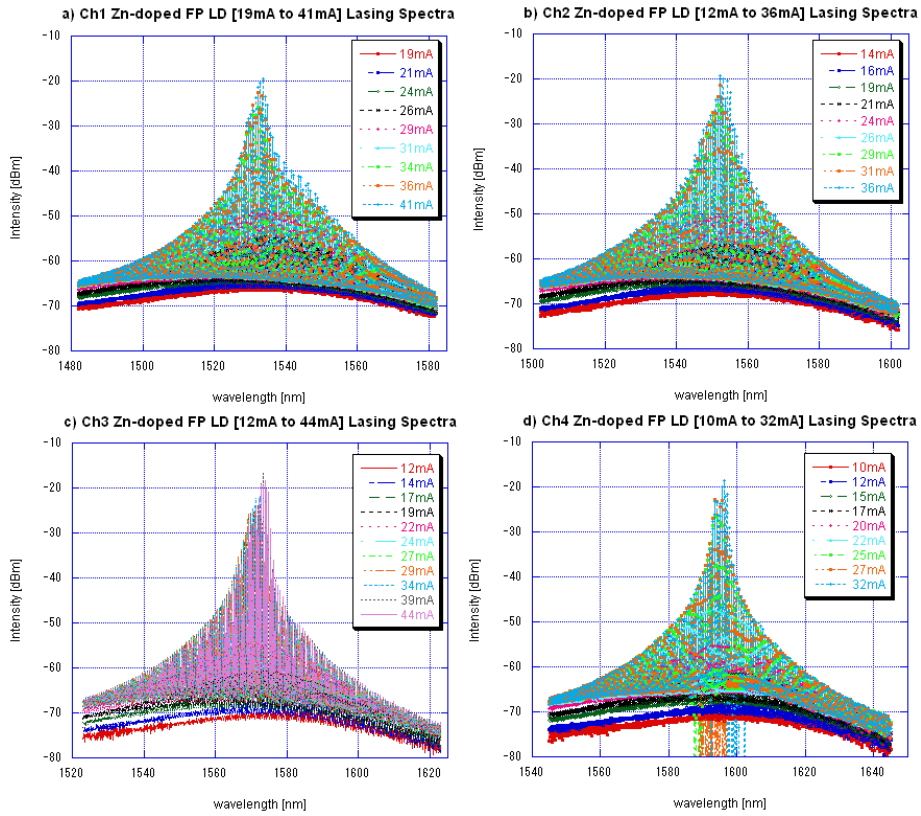
Fig.6.17 Lasing Spectra of sample#4800-1002 (zinc doped) from channel 1(a) to channel 4(d).
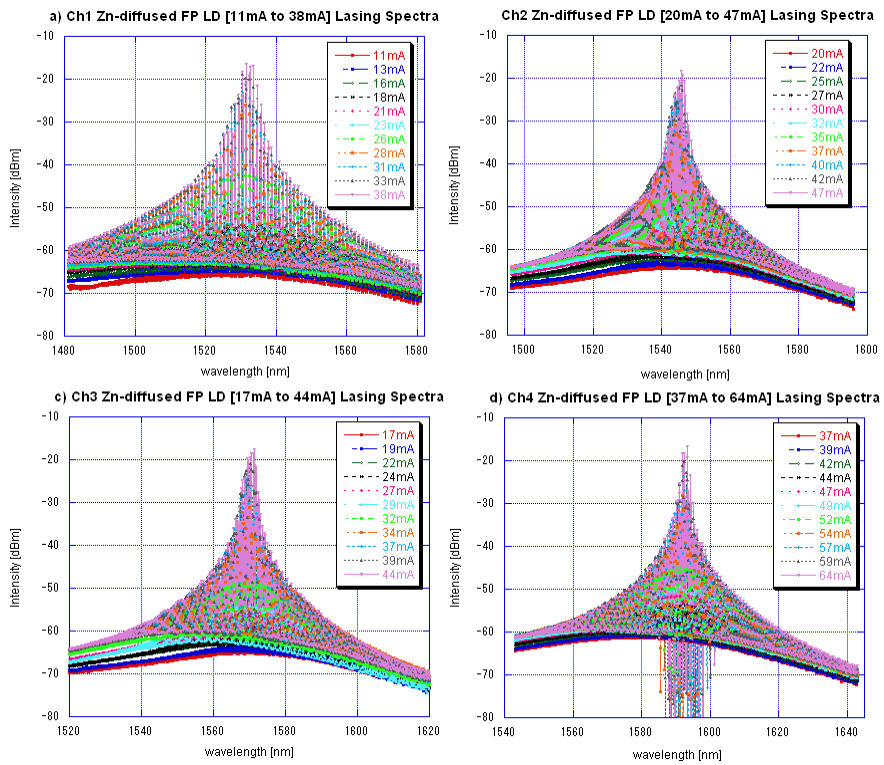
Fig.6.18 Lasing Spectra of sample#4890-1213 (zinc diffused) from channel 1(a) to channel 4(d).

6.2.4 Net Modal Gain, ĝ

In this study, the net modal, ĝ is one of the parameters which can be extracted from the spectra obtained in the last subsection thru the Hakki and Paoli method. [55]The expression is derived as follow:

$$\overline{g}_{hp}(\lambda_0) = \frac{1}{L} \ln \frac{\sqrt{\rho_{hp}(\lambda_0)} - 1}{\sqrt{\rho_{hp}(\lambda_0)} + 1} \qquad (6.7)$$

in which

$$\rho_{hp}(\lambda_0) = \frac{P_{max}(\lambda_0 - \Delta\lambda) + P_{max}(\lambda_0 + \Delta\lambda)}{2P_{min}(\lambda_0)} \qquad (6.8)$$

Where the subscription "hp" stands for "Hakki-Paoli" and p_{hp} is the ratio of maximal P_{max} to adjacent minimal intensities P_{min} of the laser's Fabry-Perot modes.
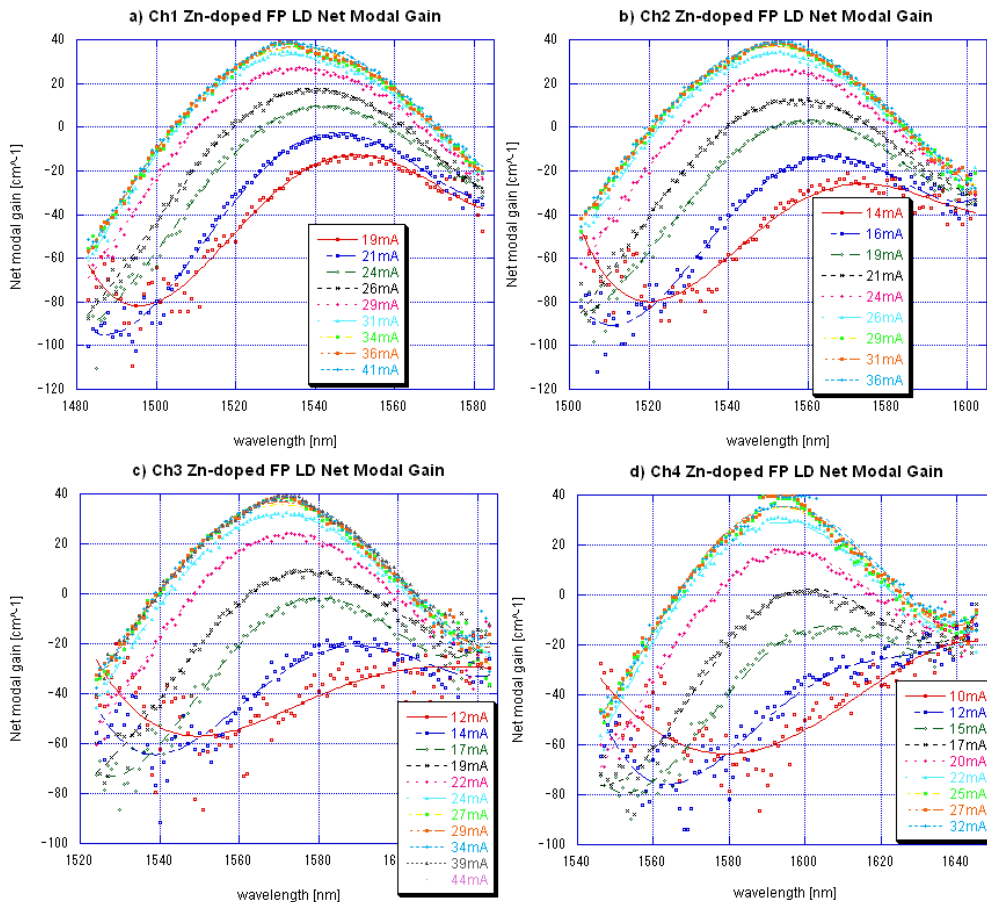
Fig.6.19 Net modal gain with respect to wavelength of channel 1(a) to 4 (d) of

sample#4800-1002 (zinc doped)
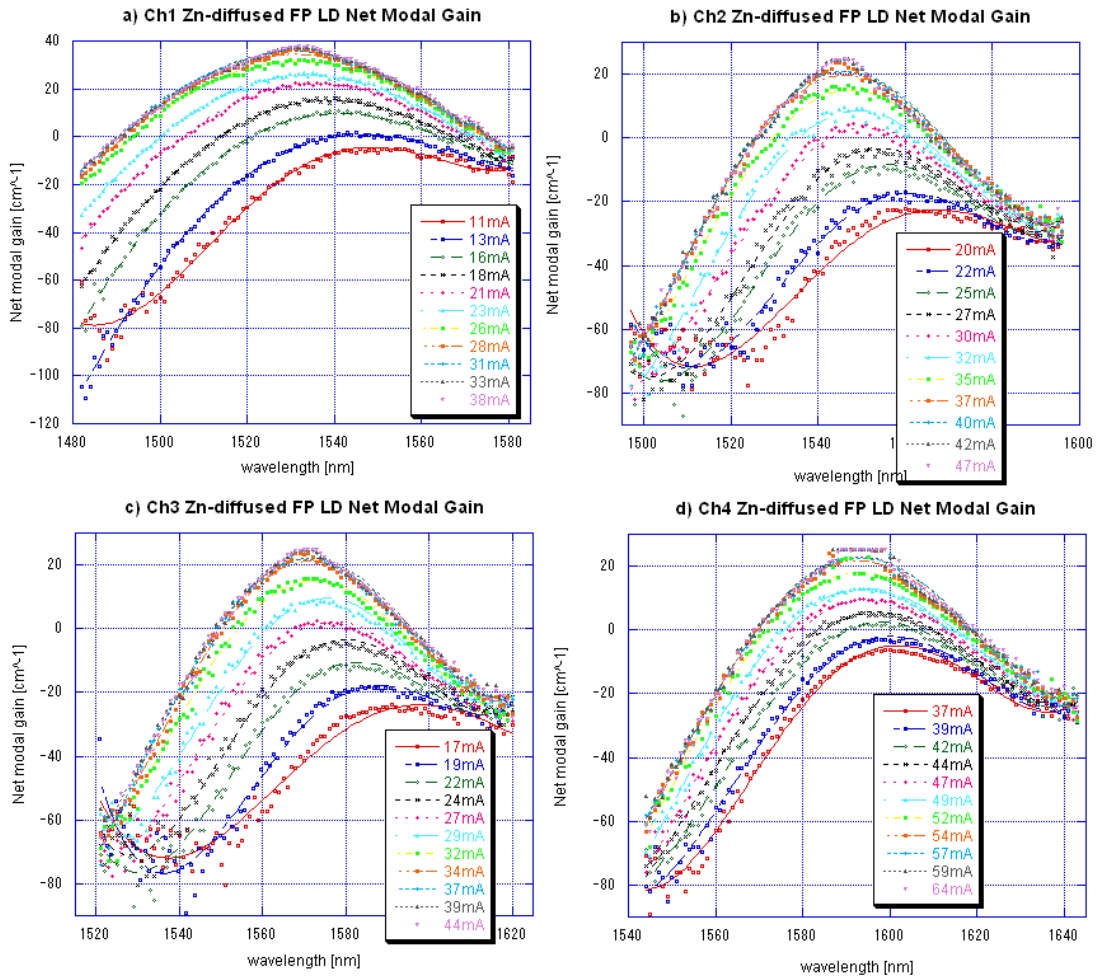
Fig.6.20 Net modal gain with respect to wavelength of channel 1(a) to 4 (d) of sample#4900-1213(zinc diffused)

In this study, spectra of lasing wavelength ± 50nm (or in short range of 100nm with lasing wavelength as median) were taken from each channel from both sample#4800-1002 (zinc doped) and sample#4890-1213 (zinc diffused). All spectra were measured at stabilized temperature of 15°C. Since the cavity temperature would increase with increasing currents, we made sure the temperature controller is maintained at 15°C all the time during measurement. The evaluation of the gain spectra at different currents provided the averaged modal gain of sample#4800-1002 and sample#4890-1213. We have depicted the net gain curves of sample#4800-1002 in Fig. 6.19 and sample#4890-1213's in Fig. 6.20. The solid curves are 9th order polynomial least-square fits. It is observed that the gain peak is occurred in the region near the lasing spectra,

and clamp at around 40cm^{-1} for sample#4800-1002 and around 20 cm^{-1} for most channels of sample#4890-1213. Although the net material gain, g_m, can be calculated thru the following expression:

$$\overline{g} = \Gamma g_m - \alpha_i - \alpha_{tot} \qquad (6.9)$$

However, the simulation of internal losses α_i and mirror losses α_m are not included in this study.

6.2.5 Alpha factor,

The alpha factor, α, also called linewidth enhancement factor or amplitude-phase coupling factor, is a key parameter for semiconductor lasers. It denotes the coupling between the induced phase changes and the amplitude changes of a signal in a device. [56] Usually, the alpha factor should be small in lasers in order to reduce chirp. Alpha-factor measurements such as 1) dependency on wavelength, 2) carrier density and 3) temperature are available, however, for simplicity; we only focused on dependency on wavelength.

In order to determine the alpha-factor of a laser, refractive index and gain shift from the spectra of the FP laser were first determine. We extracted these parameters thru the spectra we obtained in section 6.2.3. Depicted in Fig. 6.21 are some Spectra of channel 3 from sample#4800-1002, which taken from 17mA to 27mA. The gradual phase shift and amplitude gain can be observed. Refractive index and gain shift is obtained the following equations:

$$\Delta n = \frac{\lambda}{4\pi L}(\Delta\phi) \qquad (6.10)$$

$$g = \frac{1}{L}\log\left(\frac{1}{R}\frac{\sqrt{H}-1}{\sqrt{H}+1}\right) \qquad (6.11)$$

Where Δn is the refractive index shift, λ the wavelength, L the length of the laser cavity, and Δφ the phase shift of the lightwave. Here, Δφ can be calculated by the division of spectrum peak shift by the optical wavelength. The gain at each injected current was obtained from the amplitude of the Fabry-Perot oscillation of the spectrum; L stands for the length of the cavity of the LD, R the power reflectivity of both facets, and H for the ratio contrast between maximum and minimum of the Fabry-Perot ripples. The R is assumed to be 0.3 in this study.
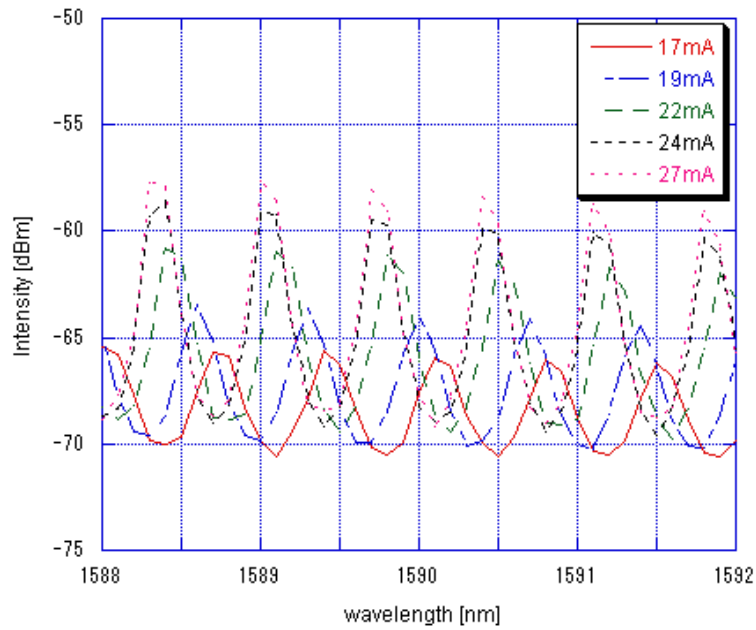
Fig.6.21 Example Spectra of channel 3 from sample#4800-1002, taken from 17mA to 27mA. Alpha factor can be determined by calculating the change in phase and gain with respect to the injected current.
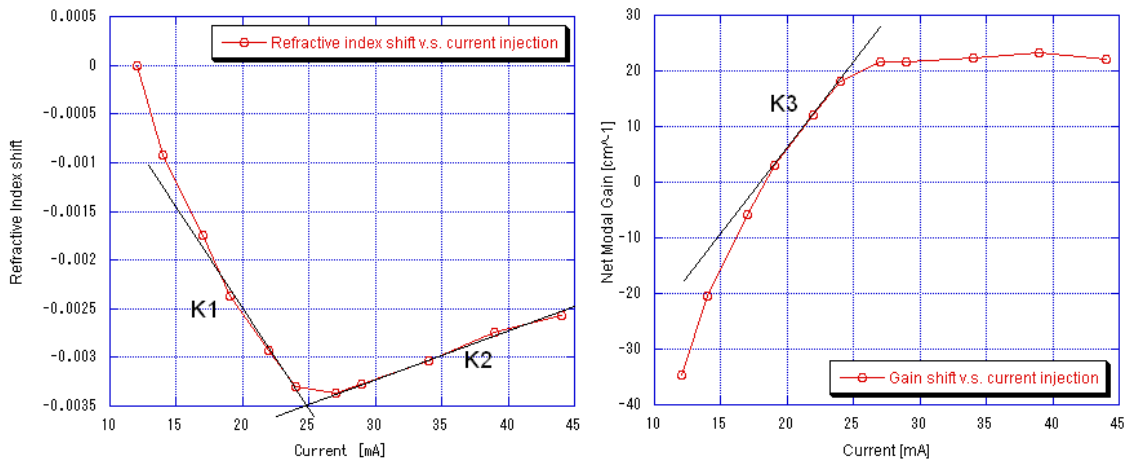
Fig.6.22 (Left) the relative refractive index change and (Right) the gain change obtained are extracted from the spectra illustrated in Fig. 6.21.

By applying equation 6.10 and 6.11, we obtained the refractive index and gain shift for each of the four channels in both sample#4800-1002 (zinc doped) and sample#4890-1213 (zinc diffused). Fig. 22 illustrates the relative index change (at the left) and the gain change (at the right) thru extracting

81

parameters from Fig. 6.21. K_1 and K_2 in the said figure are differential refractive index, dn/dI, before and after lasing. Since the carrier density become constant as illustrated in right graph of Fig. 6.22, K_2 indicates the carrier heating effect resulting from the current injection. Compensation for this temperature effect can be done by subtracting K_2 from K_1, and the alpha factor of these two LD arrays can be obtained thru the following expression:

$$\alpha = -\frac{4\pi}{\lambda} \cdot \frac{dn/dN}{dg/dN} = -\frac{4\pi}{\lambda} \cdot \frac{dn/dI}{dg/dI} \cong -\frac{4\pi}{\lambda} \cdot \frac{(K_1 - K_2)}{K_3} \qquad (6.12)$$
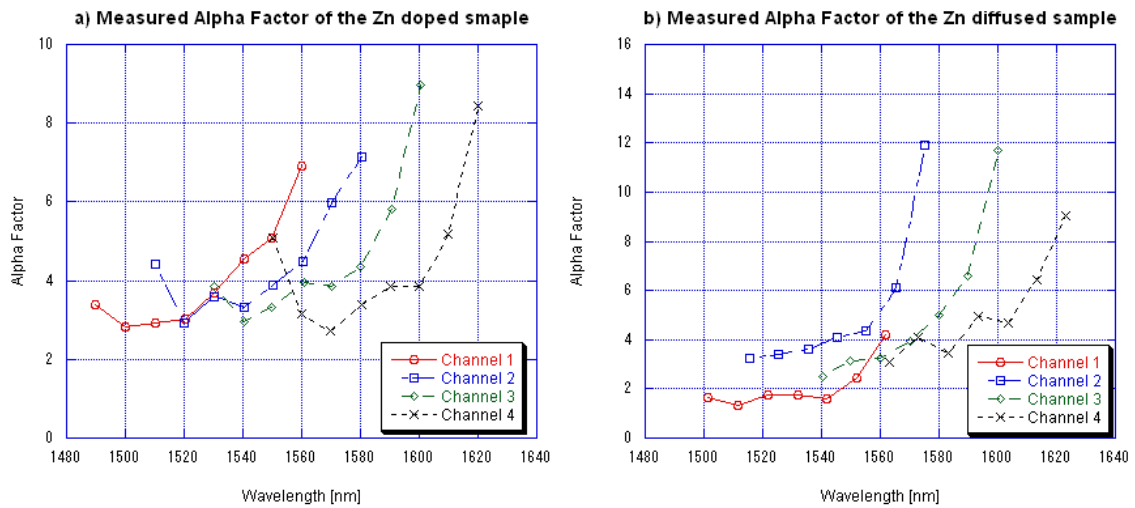
Fig.6.23 Calculated alpha factor of the zinc doped sample (a) and zinc diffused sample (b)
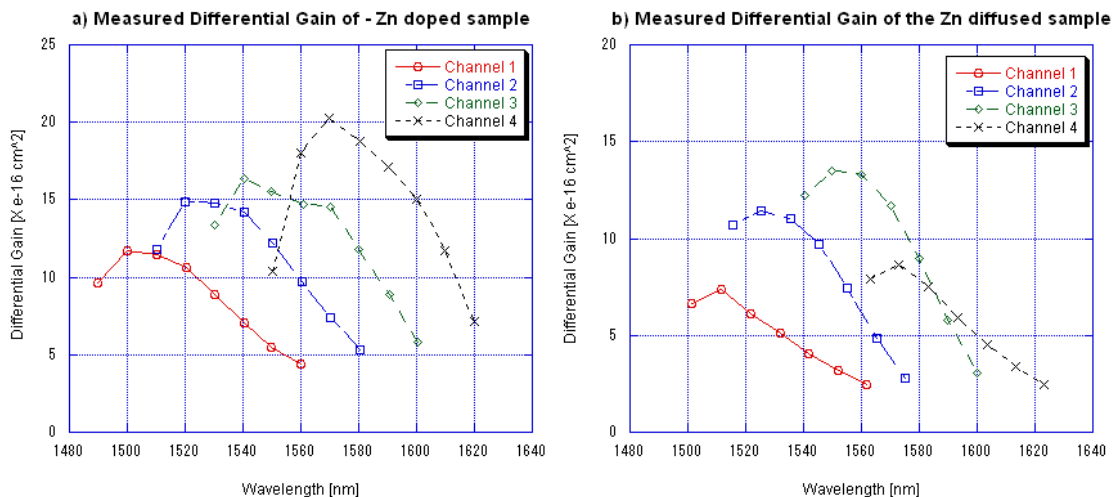
Fig.6.24 Calculated differential gain of the zinc doped sample (a) and zinc diffused sample (b)

The changes of alpha factor with wavelength are displayed in Fig. 6.23:

the sample#4800-1002's results at left and sample#4890-1213's at right. In typical case, the alpha factor increases with increasing wavelength. Results in Fig.6.23 agree with such tendency. This is due to at longer wavelengths the higher carrier injection density additionally increases the alpha factor. Finally, the differential gains of both samples are illustrated in Fig. 6.24. Differential gain is defined calculated thru the following equation:

$$g' = \frac{dg}{dN} = \frac{dg}{dI/(e \cdot V) \cdot \tau} \cong \frac{e \cdot V}{\tau} \cdot K_3 \qquad (6.13)$$

Where N is the carrier density, e the elementary electric charge, the carrier life time and V the volume of the active layer. The volume of the active layer is considered only the core layer of the cleaved laser which means from lower SCH, MQW, up till upper SCH. For details of structure, refer to table 4.1

6.3 Conclusion

In this chapter, passive components and active components were measured separately.

In passive components, propagation loss measurement of straight passive waveguides, multimode interference (MMI) couplers and S-bend passive waveguides were details in the first section of this chapter. Doped and undoped straight passive waveguides were first cleaved into different length, and propagation loss measurement by Fabry-Perot method was conducted. Approximately 10 to 15 dB/cm loss were observed in the undoped passive waveguides while 25 to 30dB/cm loss were observed in the doped one. The 15dB/cm difference between the doped and undoped passive waveguides is mainly due to carrier absorption.

MMI couplers and S-bend passive waeguides were measured both qualitatively and quantitatively. In qualitative measurement, the optical images were first captured from the output facets of the passive components via a CCD infrared camera, the results were then compared to the one captured thru a adjacent straight waveguide. In quantitative measurement, the output power were measured between a straight waveguide and a MMI coupler/S-bend

waveguide. It is observed that excess of 1.46dB loss from and a standard 6-dB MMI Coupler. Meanwhile, 0.66 dB loss (1.86 dB loss) where observed between a R2757 (R1000) S-bend waveguide and an adjacent straight waveguide.

In the active parts, zinc doped and zinc diffused Fabry-Perot laser diodes were separately cleaved and different characteristics were measured and analyzed. Basic laser characteristics such as I-V curves, I-L curves, spectrum analysis were measured. Other additional characteristics such as temperature dependency, materials gain, alpha factor measurements and etc. were extracted and analyzed based on the result from basic laser characteristics. In the end, both zinc doped and zinc diffused Fabry-Perot Laser diode arrays performed similarly and accordingly. Although it the latter one can be optimized further, it can be concluded that, zinc diffused sample can work as good as zinc diffused sample. Thus, it is feasible to apply such techniques to integrated device by selective area MOVPE.

7. Conclusion

Through out this thesis, we have demonstrated and established the selective area MOVPE technique as a promising technique in monolithic integration of photonic integrated circuits. However we also demonstrate the issues behind this technique and provided a proposed solution to solve this particular issue. This proposed solution is thru selective zinc diffusion.

In chapter 2, we have detailed the Metal Organic Vapor Phase Epitaxy (MOVPE) and Selective Area Growth (SAG) technique which is used throughout this thesis. The principle of the selective area Growth, especially the importance of the W_m/G_m ratio in bandgap engineering with SA-MOVPE has been discussed, and the design of W_m/G_m ratio for four channels using in 1.55μ m CWDM system has been realized. Ridge lasers will be fabricated within the mentioned SAG regions. In addition, the Micro-Photoluminescence Profiles of SAG such as transverse scan, center scan and active to passive transition scan has been investigated. And lastly, the issue of selective area MOVPE, particularly the p-doped InP materials in upper cladding of passive parts has been detailed, thus the main issue in this study would be focusing.

In chapter 3, we have studied the feasibility of the selective zinc diffusion, as a solution toward the specific issue in selective area MOVPE integrated Devices. Then ideal zinc diffusion profiles were obtained thru repeated tests and these data were analyzed thru Fick's second law of diffusion. Error-function solution was also used to fit the SIMS data obtained from the same diffusion profile. In the later part of this chapter, we have discussed the Implementation of zinc diffusion into a separately selective area grown laser diode array and the sample were tested thru Secondary Ion Mass Spectroscopy (SIMS) analysis, along with a zinc doped samples. The zinc diffusion profiles show doping density of $\sim 10^{19} cm^{-3}$ were observed in the InGaAs contact layer of both samples and $\sim 10^{17} cm^{-3}$ to $\sim 10^{18} cm^{-3}$ of in both of the upper InP cladding layer. These promising results for typical laser doping level support the feasibility of zinc diffused device, and further, the potential of selective zinc diffusion in selective

are MOVPE monolithically integrated devices.

In chapter 4, we have detailed the overall design consideration of the Monolithically Integrated 4-Channel DFB Laser Array with Optical Combiner for 1.55μm CWDM Systems by Selective Area MOVPE. Active and passive components have been separately studied thoroughly. Beam-Propagation Method (BPM) analysis was used to simulate the performance of the passive components such as MMI coupler and S-bend passive waveguides. The width tolerance and length tolerance of the MMI is calculated based on the data obtained from BPM analysis: 30 ± 0.85μm for width tolerance and 530 ± 29μm for length tolerance. Simultaneous lasing spectrum of the final device is also illustrated in this chapter. However due to thermal crosstalk, the current required is dramatically increased for the simultaneous lasing occurred. In the last part of the chapter, the low yield issue of DFB lasers is stated. For this reason, we decided to separately fabricate the active and passive components and test the feasibility of zinc diffusion for selective area grown device.

In chapter 5, we have described the general fabrication procedures of 2 parts: 1) passive components and 2) active components. In passive components, the doped and undoped passive waveguides were fabricated for loss measurement comparison, and in the active components, zinc doped and zinc diffused Fabry-Perot Laser Diode arrays were fabricated for result comparing. During the epitaxy growth of both components, instead of the conventional single-step-epitaxy growth which is featured in Selective Area Growth (SAG), we used a two-step-epitaxy growth. The core was grown first, followed by etching of SiO$_2$ mask, and then the growth of upper cladding and InGaAs contact layer. The reason behind this is for evenly zinc diffusion into the upper contact layer of all channels. In the passive components fabrication, wet etching was used on both doped and undoped passive waveguides. In addition, dry-etching was also used on the undoped components for reference purpose. SEMS images of etched MMI couplers were used to illustrate the difference between wet and dry etching.

In chapter 6, we have characterized the fabricated passive components and active components separately. In passive components, we have measured both undoped and doped sample using Fabry-Perot propagation loss

measurement. These passive components include straight passive waveguides, MMI couplers and S-bend passive waveguides. As a result, approximately 10 to 15 dB/cm loss were observed in the undoped passive waveguides while 25 to 30dB/cm loss were observed in the doped one. The 15dB/cm difference between the doped and undoped passive waveguides is mainly due to carrier absorption. MMI couplers and S-bend passive waveguides were measured both qualitatively and quantitatively with an adjacent straight waveguide. Based on the quantitative measurement result, we observed an excess of 1.46dB loss in our 4X1 MMI coupler compare to a standard 6-dB MMI Coupler, and 0.66 dB loss (1.86 dB loss) where observed between a R2757 (R1000) S-bend waveguide and an adjacent straight waveguide. In the active parts, zinc doped and zinc diffused Fabry-Perot laser diode arrays were separately cleaved and tested. Basic laser characteristics such as I-V, I-L curves, spectrum analysis were measured. Other additional characteristics such as temperature dependency, materials gain, alpha factor measurements were extracted and analyzed based on the result from basic laser characteristics. In the end, we can conclude that both zinc doped and zinc diffused Fabry-Perot Laser diode arrays performed similarly and accordingly. Although selective zinc diffusion can be further optimized, in the mean time, it can be concluded that, zinc diffusion is a feasible method in applying to integrated device by selective area MOVPE.

Although the final objective of implementing the selective zinc diffusion into the Monolithically Integrated 4-Channel DFB Laser Array with Optical Combiner for 1.55μm CWDM Systems by Selective Area MOVPE, has been attempted but not accomplished thru this thesis. But other two main objectives have been achieved. First, provided similar epitaxy structure, fabricated condition and testing setup, a passive waveguide with zinc doped InP materials (*the doped waveguide*) is in fact suffer more optical loss than one with undoped InP cladding (*the undoped waveguide*), which believed due to carrier absorption. This has been thoroughly studied and proved in the chapter 6. Secondly, zinc diffusion is a feasible method in fabricating laser diodes array by selective area MOVPE. Different characterization has been carried out with *the zinc diffused laser diode arrays,* and this data was compared to the conventionally selective area grown laser diode array (*the zinc doped laser diode arrays*). Data from different characterization show both laser diode arrays performed similarly and accordingly. We believed by providing further optimization of the zinc diffusion

profile, improvement of fabrication techniques such as dry etching condition, and the optimization of epitaxy crystalline condition, the present zinc diffused laser diode can performed even better.

With the two accomplished objectives mentioned above, we believed selective zinc diffusion should be able to reduce passive waveguide's loss in monolithically integrated device by selective area MOVPE.

Further improvement of this thesis might include growth/structure optimization. Improving the confinement factor or increase the number of wells might be one of the considerations. In addition, further zinc profile optimization, and selective area growth (SAG) design optimization may be included. A more compact design of SAG array has been designed and under investigation recently, if the outcome turns out to be ideal, it may include into the device of this thesis, thus, decreases the over all size which means increase the number of device across a single substrates. At the same time, by reducing the size, it might also contribute to reduction of loss especially in the passive components such as S-bend passive waveguides.

8. References

[1] Erik J. Skogen, James W. Raring, Jonathon S. Barton, ,Steven P. DenBaars, and Larry A. Coldren, "Postgrowth Control of the Quantum-Well Band Edge for the Monolithic Integration of Widely Tunable Lasers and Electroabsorption Modulators" *IEEE J. Sel. Topics Quantum Electron.*, vol. 9 no.5, pp.1183-1190, Sep./Oct., 2003

[2] Ronald Kaiser and Helmut Heidrich, "Optoelectronic/Photonic Integgrated Circuits on InP between Technological Feasibility and Commercial Success" *IEIC Tran. on Electron.*, vol. E850C no.4, April, 2002

[3] F. Xia, V. Menon, S. R. Forrest, "Photonic Integration Using Asymmetric Twin-Waveguide (ATG) Technology: Part I – Concept and Theory" *IEEE J. Sel. Topics Quantum Electron.*, vol. 11 no.1, pp.17-29, Jan./Feb., 2005.

[4] T. Kitatani, K. Shinoda, T. Tsuchiya, H. Sato, K. Ouchi, H. Uchiyama, S. Tsuji, and M. Aoki , "Evaluation of the Optical-Coupling Efficiency of InGaAlAs–InGaAsP Butt Joint Using a Novel Multiple Butt-Jointed Laser," *IEEE Photon. Technol. Lett.*, vol. 17 no.6, pp.1148-1150, June, 2005.

[5] H. Kunzel, S. Ebert, R. Gibis, P. Harde, R. Kaiser, H. Kizuki, and S. Malchow, "Laser/waveguide Intergration Utilizing Selective Area MOMBE Regrowth for Photonic IC Applications," *10th Intern. Conf. on Indium Phosphide and Related Materials*, 11-15 May 1998, Tsukuba, Tokyo.

[6] M. Raburn, M. Takenaka, J. S. Barton, X. L. Song, K. Takeda, and Y. Nakano, "Design and Preliminary Fabrication of Integrable All-Optical Flip-Flops Based on DBR Multimode Interference Bistable Laser Diode Structure", *Symposium,* Sep, 2005.

[7] M. Takenaka, M. Raburn, and Y. Nakano, "All-Optical Flip-Flop Multimode Interference Bistable Laser Diode," *IEEE Photon. Technol. Letter.*, vol. 17, No. 5   pp.968-970, May 2005

[8] Hery Susanto Djie, and Ting Mei, "Plasma-Induced Quantum Well Intermixing for Monolithic Photonic Integration" *IEEE J. Sel. Topics Quantum Electron.*, vol. 11 no.2, pp.373-382, March./April., 2005.

[9] Erik J. Skogen, et al., "Monolithically Integrated Active Components: A Quantum-Well Intermixing Approach" *IEEE J. Sel. Topics Quantum Electron.*, vol. 11 no.2, pp.343-355, March./April., 2005.

[10] Erik J. Skogen, et al., "A Quatum-Well-Intermixing Process for Wavelength-Agile Photonic Integrated Circuits" *IEEE J. Sel. Topics Quantum*

Electron., vol. 8 no.4, pp.863-869, Jul./Aug., 2002

[11] T. Sasaki, "Selective MOVPE technique and its application for photonics for photonic devices," *Technical Digest CLEO/Pacific Rim '99*, Seoul, Korea, pp.1068-1069, Aug, 1999.

[12] Foo Cheong, Yit*,* "Fabrication of Monolithically Integrated Interferometer Switches by Selective Area MOVPE and their All-optical Signal Processing Application" *Ph.D. Thesis, The University of Tokyo.*,Japan, 2006.

[13] Xueliang, Song*,* "Study on Monolithically Integrated Mach-Zehnnder Interferometer All-Optical Swichted by Selective Area MOVPE" *Ph.D. Thesis, The University of Tokyo.*,Japan, 2003.

[14] M. Gibbon, J. P. Stagg, C. G. Cureton, E. J. Thrush, C. J. Jones, R. E. Mallard, R. E. Pritchard, N. Collis, and A. Chew, "Selective-area low-pressure MOCVD of GaIn- AsP and related materials on planar InP substrates", *Semicond. Sci. Technol.*, vol. 8, pp. 998-1010, 1993.

[15] M. Aoki et al., "Detuning adjustable multiwavelength MQW-DFB laser array grown by effective index/quantum energy control selective area MOVPE", *IEEE Photon. Technol. Lett.,* vol. 6, no. 7, pp. 789-791, July 1994.

[16] Kudo K, Yamazaki H, Sasaki T, Yamaguchi M, "Wide-wavelength range detuningadjusted DFB-LD's of different wavelengths fabricated on a wafer," *IEEE Photon. Technol. Lett.*, vol. 9, no. 10, pp. 1313-1315, 1997.

[17] Kudo K, Ishizaka M, Sasaki T, et al. "1.52-1.59-mu m range different-wavelength modulator-integrated DFB-LD's fabricated on a single wafer," *IEEE Photon. Technol. Lett.*, vol. 10, no. 7, pp.929-931, 1998.

[18] Mori K, Hatakeyama H, Hamamoto K, et al., "Narrow-stripe selective growth of high-quality MQWs by atmospheric-pressure MOVPE," *J Cryst. Growth*, 195: (1-4), pp.466-473, DEC 1998.

[19] Y.Muroya, et al., "100 , 10-Gb/s Direct Modulation with a Low Operation Current of 1.3-μm AlGaInAs Buried Heterostructure DFB Laser Diodes," *Optical Fiber Communication Conference* (OFC 2003), *Tech. Dig.* Series, FG6, pp.683-684, Atlanta, 2003.

[20] D.J. Lawrence et al, "Zinc diffusion process for GaAsP red light emitting diode fabrication in an undergraduate laboratory," *Proceedings of the 12th Biennial University /Government /Industry Microelectronics Symposium*, July 20-23, 1997.

[21] Wei Yang et al. "Planar GaAs-AlGaAs MQW Transverse Junction Ridge Waveguide Lasers Using Shallow Zinc Diffusion," *IEEE Photon. Technol.*

Lett., vol. 7, no. 8, pp.948-850, Aug., 1995.

[22] Y. Nagai et al., "Fabrication of Broad-Area Laser Diodes on a Three-Inch Wafer by a Solid-Phase Diffusion Method," *IEEE Photon. Technol. Lett.*, vol. 7 no.5, pp.464-466, may, 1995.

[23] J. R. Lowney and R.D. Larrabee. "The Use of Fick's Law in Modeling Diffusion Processes," *IEEE Transaction of Electron Devices,* vol. ED-27, no. 9, pp.1795-1798, 1980.

[24] P.F. Lesse et al, "Generalizations of the Diffusion Equation," *Journal of Polymer Science,* Part A-2, Vol. 9, pp.755-758, 1971.

[25] G.Y Tai et al. "Modeling of Zn Diffusion in InP/InGaAs Materials During MOVPE Growth," *11th International Conference on Indium Phosphide and Related Materials,* pp.245-247, 16-20 May 1999, Davos, Switzerland.

[26] G. J. van Gurp, et al. "Zinc Diffusion in InGaAsP," *Appl. Phys.. Lett.64*, vol. 7, pp.3468-3471, Oct.,1988.

[27] M. Wada et al. "Zn Diffusion into InP using Dimethylzinc ad Zn Source" *Japanese Journal of Applied Physcis,* vol. 28, no. 10, pp.L1700-1703, Oct, 1989.

[28] M. Wada et al. "Investigation of Zn Diffusion in InP using Dimethylzinc ad Zn Source" *Journal of Crystal Growth,* vol. 114, pp.321-326, 1991

[29] D. Franke et al. "Post-growth Zn Diffusion into InGaAs/InP In a LP-MOVPE reactor" *Journal of Crystal Growth,* vol. 195, pp.112-116, 1998

[30] M. Yamada, P.K. Tien et al. "Double Zinc Diffusion fronts in InP – Theory and experiment," *Appl. Phys.. Lett.43*, vol. 6, pp.594-596, Sept.,1983.

[31] Jesse Darja*,* "Integrated 1.55µm Distributed Feedback laser Array by Selective Area Growth for Coarse Wavelength Division Multiplexing" *Ph.D. Thesis, The University of Tokyo.*,Japan, 2007.

[32] K. Tsuruoka et al, "Four-channel 10-Gb/s operation of AlGaInAs-MQW-BH-DFB-LD array for 1.3-µm CWDM systems" *J. Sel. Topics Quantum Electron.*, vol. 11 no.5, pp.1169-1173, Sept/Oct., 2005

[33] Chuang-en Zah, et al.*,* "Multiwavelength DFB Laser Arrays with Integrated Combiner and Optical Amplifier for WDM Optical Networks" *IEEE J. Sel. Topics Quantum Electron.*, vol. 3 no.2, pp.584-596, April., 1997

[34] Y. Suzaki, et al*,* "Monolithically Integrated Eight-Channel WDM Modulator With Narrow Channel Spacing and High Throughput" *IEEE J. Sel. Topics*

Quantum Electron., vol. 11 no.1, pp.43 - 49, Jan../Feb.., 2005.

[35] P.P. Iannone et al, "Amplified CWDM Systems," *1 Lasers and Electro-Optics Society, 2003. LEOS 2003. The 16th Annual Meeting of the IEEE*, vol. 2, pp:678 – 679, 2003

[36] L. A. Buckman et al, "Demonstration of a small-form-factor WWDM transceiver moduler for 10Gb/s local area networks" *IEEE Photon. Technol. Lett..*, vol. 14 no.5, pp.702-704, May., 2005.

[37] Torsten Mitze et al., "CWDM Transmitter Module Based on Hybrid Integration" *IEEE J. Sel. Topics Quantum Electron.*, vol. 12 no.5, pp.983-987, Sept/Oct., 2006

[38] G. P. Agrawal and N. K. Dutta, "Semiconductor Lasers", Van Nostrand Reinhold, NY.. (1993)

[39] G. Morthier and P. Vankwikelberge, "Handbook of Distributed Feedback Laser Diodes" Artech House, Inc, Norwood MA. (1997)

[40] M. Amann and J. Buus, "Tunable Laser Diodes", Artech House, Inc., Norwood MA. (1998)

[41] H. Ghagouri-Shiraz, "Distributed Feebback Laser Diodes and Optical Tunable Filters", John Wiley & Sons, Ltd.,, UK. (2003)

[42] H. Zappe, "Laser Diode Microsystems", Springer, Germany. (2004)

[43] L.B. Soldano et al, "Optical multi-mode interference devices based on self-imagine: principles and applications," *IEEE J. Lightwave Technol.*, vol. 13, No. 4, pp.615-627, April, 1995.

[44] E.C.M. Pennings et al., "Reflection Properties of Multimode Interference Devices," *IEEE Photon. Technol. Lett.*, vol. 6 no.6, pp.715-718, June, 1994.

[45] A. Ferreras et al., "Useful Formulas for Multimode Interference Power Splitter/Combiner Design," *IEEE Photon. Technol. Lett.*, vol. 5 no.10, pp.1224-1227, Oct, 1993.

[46] Y. Gottesman et al., "A Novel Design Proposal to Minimize Reflections in Deep-Ridge Multimode Interference Couplers," *IEEE Photon. Technol. Lett.*, vol. 12 no.12, pp.1662-1664, Dec, 2004.

[47] M. Zirngibl et al., "Efficient 1 x 16 Optical Power Splitter Based on InP," *IEEE Electron. Lett.*, vol. 28 no.13, pp.1212-1213, June, 1992.

[48] M. Bachmann et al, "General self-imaging properties in N x N multimode

interference couplers including phase relationships," *Appl. Optics,* vol. 33, No. 18 pp.3905-3911, june, 1994.

[49] P. A. Besse et al., "Optical Bandwidth and Fabrication Tolerances of Multimode Interference Couplers," *IEEE J. Lightwave Tech..*, vol. 12 no.6, pp.1004-1009, June, 1994.

[50] M. J. Adams*,* "An Introduction to Optical Waveguides", John Wiley & Sons, Ltd., USA. (1981)

[51] C. Dragoc*,* "Optimum Planar Bends" *IEEE Elec.. Lett.*, vol. 29 no.12, pp.1121-1122, June., 1993.

[52] Eli Kapon*,* "Semiconductor Laser I Fundametals", Academic Press, USA. (1999)

[53] Eli Kapon*,* "Semiconductor Laser II Materials and Structures", Academic Press, USA. (1999)

[54] M. Fukuda*,* "Optical Semiconductor Devices", John Wiley & Sons, Ltd.,, USA. (1999)

[55] J. Leuthold*,* "Advanced Indium-Phosphide Waveguides Mach-Zehnder Interferometer All-Optical Switches and Wavelength Converters" ,Hartung-Gorre, Germany. (1999)

[56] B. Zhap et al. "Direct measurement of linewidth enchancement factors in quantum well lasers of different quatum well barrier heights," *Appl. Phys.. Lett.42*, vol. 14, pp.1591-1593, April,1993.

[57] P. V. Studenkov, et al., "Monolithic integration of a quantum-well laser and an optical amplifier using an asymmetric twin-waveguide structure," *IEEE Photon. Technol. Lett.*, vol. 10, pp.1088-1090, Aug, 1998.

[58] F. Xia, V. Menon, S. R. Forrest*,* "Photonic Integration Using Asymmetric Twin-Waveguide (ATG) Technology: Part II – Devices" *IEEE J. Sel. Topics Quantum Electron.*, vol. 11 no.1, pp.30-42, Jan./Feb., 2005.

[59] C. Schbert, et al., "160-Gbit/s all-optical demultiplexing using a gain-transparent ultrafast-nonlinear interferometer (GT-Uni)," *IEEE Photon. Technol. Lett.*, vol. 13, pp.475-477, May, 2001.

[60] M. Heid, et al., "160-Gbit/s demultiplexing based on a monolithically integrated Mach-Zehnder interferometer," *Proc. Eur. Conf. Optical Comm. (ECOC 2001)*, Amsterdam, The Netherlands, Sept 30- Oct 4, 2001.

[61] P. V. Studenkov, M. R. Gokhale, and S.R. Forrest, "Efficient Coupling in

Integrated Twin-Waveguide Lasers Using Waveguide Tapers," *IEEE Photon. Technol. Lett.*, vol. 11, No. 9, pp.1096-1098, Sept, 1999.

[62] M. Takenaka and Y. Nakano, "Multimode Interference Bistable Laser Diode," *IEEE Photon. Technol. Letter.*, vol. 15, No. 8 pp.1035-1037, Aug. 2003.

[63] Jung-Ho Song, Jung-Woo Park, Eun-Deok Sim, and Yongsoon Baek, "Measurements of Coupling and Reflection Characteristics of Butt-Joints in Passive Waveguide Integrated Laser Diodes," *IEEE Photon. Technol. Lett.*, vol. 17 no.9, pp.1791-1793, September, 2005.

[64] Y. Kawakita, et al., "Wavelength Demultiplexer Using GaInAs-InP MQW-Based Variable Refractive-Index Arrayed Waveguides Fabricated by Selective MOVPE" *IEEE J. Sel. Topics Quantum Electron.*, vol. 11 no.1, pp.211- 223, Jan../Feb.., 2005.

[65] Tien Pei Lee et al, "Multiwavelength DFB Laser Array Transmitters for ONTC Reconfigurable Optical Network Testbed" *J. Lightwave Tech.*, vol. 14 no.6, pp.967-975, June., 1996

[66] Marko Galarza, et al., "Mode-Expanded 1.55-μm InP-InGaAsP Fabry-Perot Lasers Using ARROW Waveguies for Efficient Fiber Coupling" *IEEE J. Sel. Topics Quantum Electron.*, vol. 8 no.6, pp.1389-1398, Nov./Dec., 2002

[67] K. Kudo et al, "1.55-μm wavelength-selectable microarray DFB-LD's with monolithically integrated MMI combiner, SOA, and EA-modulator" *IEEE Photon. Technol. Lett.*, vol. 12 no.3, pp.242-244, March., 2000.

[68] A.A. Ballman et al. "Double Doped Low Etch Pit Density InP with Reduced Optical Absorption" *Journal of Crystal Growth,* vol. 62, pp.198-202, June, 1983

[69] S. Ibrahim et al., "Source power effect on inductive coupled plasma (ICP) etching of InP near an optimized etching point",   54
2007   3

[70] R. Ramaswami, K. N. Sivarajan, "Optical Networks, A Practical Perspective", Morgan Kaufmann Publishers, USA. (2002)

[71] P. Bhattacharya, "Semiconductor Optoelectronic Devices", Prentice-Hall, Inc., New Jersey. (1997)

[72] Peter Harmsma, "Integration of Semiconductor Optical Amplifiers in Wavelength Division Multiplexing Photonic Integrated Circuits", the Netherlands. (2000)

9. Acknowledgement

This thesis could never have been accomplished without the tremendous amount of helps and supports from many people.

First and foremost, I am deeply grateful to my thesis supervisor, Professor Yoshiaki Nakano, for his guidance and professional knowledge throughout my whole research life in his laboratory. Under his supervision, I was able to spend a very beneficial and rewarding research life under his guidance. I would like to express my gratitude to Associate Professor Masakazu Sugiyama as well, for his invaluable knowledge and expertise in Selective Area MOVPE.

My study in Japan (one year as a research student and the succeeding two years as a Master degree student), would not have been possible without financial support from Panasonic Scholarship.

I'm indebted most to my colleagues: Mr. Jesse Darja, Dr. Foo-Cheong Yit, Dr. Shu-ROng Wang, Mr. Salah Ibrahim and Dr. Xue-Liang Song, for their technical collaboration and knowledge on the fundamental theory and prccessing techniques of Selective Area MOVPE. Without their pioneership and prominent results, this work could not have been completed. I also like to thank, Dr. Adbullah Al Amin, Dr. Mitsuru Takenaka, Mr. Xiao-Ping Zhao, Mr. Koji Takeda and Mr. Tomonari Shioda and many others in Nakano-Sugiyama laboratory, for all their technical expertise and support. I'm very grateful to Ms. Sueko Ui and Ms. Hiroe Miyagawa, for their dedicative daily administrative support, and Dr. Takuo Tanemura, for his daily arrangement of the laboratory and clean room maintenances.

Last but not least, I wish to express my deepest gratitude to my family: my brother, Mark; my sister, Stephanie; my father, Steven; my mother, Teresita, and my sister-in-law, Tess, for their support and encouragement during my whole stay here in Japan. I also thank all my friends from near and far, for all their support and friendship over all these years, and I especially thank Ms. Maureen Jane Tan, who has supported, encouraged and taken care of me over the past year.

10. List of Publications

Domestic Conferences Related to this Work

1. _____

   , " 　Zn　　　　　　　 MOVPE
   　　　 ", 　54
   2007 　3 　　　　.

2. _____

   , " 　 MOVPE 　　　　　　　　 CWDM 　 DFB
   ", 　　　　　　　　　　　　　 (LQE)
   　　, 2006 　12 　8 .

International Conferences Related to this Work

1. Jesse Darja, **Melvin Jeffrey C. Chan**, Masakazu Sugiyama, and Yoshiaki Nakano, "Monolithically Integrated Four-Channel DFB Laser Array by MOVPE Selective Area Growth for 1.55µm CWDM Systems," presented at IEEE Laser and Electro-Optics Society (LEOS) Annual Meeting, Montreal, Quebec, Canada, Nov 1, 2006.

Publications Related to this Work

1. Jesse Darja, **Melvin Jeffrey C. Chan**, Masakazu Sugiyama, and Yoshiaki Nakano, "Four-Channel DFB Laser Array with Integrated Optical Combiner 1.55µm CWDM Systems by MOVPE Selective Area Growth," online publication in in IEICE Electronics Express (ELEX) Vol. 3 No. 24, pp. 522-528, December 25, 2006.

2. Jesse Darja, **Melvin Jeffrey C. Chan**, Shu-Rong Wang, Masakazu Sugiyama, and Yoshiaki Nakano, "Four Channel Ridge DFB Laser Array for 1.55µm CWDM Systems by MOVPE Wide-Stripe Selective Area Growth," full paper accepted for publication in IEICE Transactions: Special Issue on Recent Advances in Integrated Photonic Devices, May 2007.

3. Jesse Darja, **Melvin Jeffrey C. Chan**, Masakazu Sugiyama, and Yoshiaki Nakano, "Four Channel Ridge DFB Laser Array for 1.55µm CWDM Systems by MOVPE Wide-Stripe Selective Area Growth," letter in preparation for submission to IEEE Photonics Technology Letters.